INVESTIGATION ON THE MATERIAL COMPOSITIONS ON AIR CATHODE IN AN ALUMINIUM-AIR BATTERY

KOH ZU HENG

UNIVERSITI TUNKU ABDUL RAHMAN

INVESTIGATION ON THE MATERIAL COMPOSITIONS ON AIR CATHODE IN AN ALUMINIUM-AIR BATTERY

KOH ZU HENG

A project report submitted in partial fulfilment of the requirements for the award of Bachelor of Mechanical Engineering with Honours

Lee Kong Chian Faculty of Engineering and Science
Universiti Tunku Abdul Rahman

May 2024

DECLARATION

I hereby declare that this project report is based on my original work except for citations and quotations which have been duly acknowledged. I also declare that it has not been previously and concurrently submitted for any other degree or award at UTAR or other institutions.

Signature : 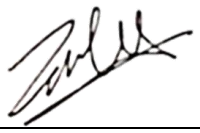

Name : KOH ZU HENG

ID No. : 20 UEB 01360

Date : 18 May 2024

APPROVAL FOR SUBMISSION

I certify that this project report entitled **"INVESTIGATION ON THE MATERIAL COMPOSITIONS ON AIR CATHODE IN AN ALUMINIUM-AIR BATTERY"** was prepared by **KOH ZU HENG** has met the required standard for submission in partial fulfilment of the requirements for the award of Bachelor of Mechanical Engineering with Honours at Universiti Tunku Abdul Rahman.

Approved by,

Signature : *WengCheong*

Supervisor : Dr. Tan Weng Cheong

Date : 18 May 2024

Signature :

Co-Supervisor :

Date :

ACKNOWLEDGEMENTS

I would like to express my sincere gratitude to my research supervisor, Dr. Tan Weng Cheong for his precious advice and guidance throughout the research. His passion towards research is always my role model to work hard on my learning journey.

In addition, I would like to thank my loving parents, sister and friends who always help and give me encouragement.

ABSTRACT

The development of metal-air batteries has gained intensive focus in recent years. Among the metal-air batteries, the aluminium-air battery is treated as one of the most favoured topics for researchers due to its low cost, high specific capacity and high theoretical energy. To improve the aluminium-air battery performance, there is a lack of information for optimizing the material composition of the air cathode. Thus, this project focuses on the optimization of the material composition of the air cathode by determining the mass ratio of each material. Taguchi Method is utilized to propose the mass ratio of each material for each sample. 5000 series aluminium alloy was selected as the material of metal anode due to its higher corrosion resistance. For the electrolyte, the aqueous KOH electrolyte was chosen as it is capable of providing higher achievable power and larger open circuit potential. The materials used to fabricate the air cathode are carbon black, activated carbon, manganese (IV) oxide, propanol and PTFE. The size of the fabricated prototype was around 3 cm*1.8 cm*4.5 cm. The fabricated samples were tested via discharge test and linear sweep voltammetry test. The results obtained were then analyzed and ranked using Grey Relational Analysis. Several relationships were extracted from the projects to obtain better performance, which is the mass ratio of Carbon Black and Propanol shall be higher and the mass ratio of Activated Carbon and PTFE shall be lower. As a result, the optimized material composition of the powder mixture (Carbon Black, Activated Carbon and Manganese (IV) Oxide), in terms of mass ratio is 9: 1: 2. While the mass ratio of the powder mixture, propanol and PTFE is 1: 3: 1. The optimized aluminium-air battery is capable of providing 1.5 V of plateau voltage, 2.046 Ah/g of specific capacity, 0.137 W of peak power and 0.3247 A of shutdown current which mainly contributed by the effect of optimized air cathode. The high plateau voltage and peak power obtained in the project further indicate the possibility of the subsequent development of air cathode optimization. In addition, the implementation of large-scale prototype will further enlarge the application of the fabricated aluminium-air batteries.

TABLE OF CONTENTS

DECLARATION **i**
APPROVAL FOR SUBMISSION **ii**
ACKNOWLEDGEMENTS **iv**
ABSTRACT **v**
TABLE OF CONTENTS **vi**
LIST OF TABLES **ix**
LIST OF FIGURES **xi**
LIST OF SYMBOLS / ABBREVIATIONS **xiii**
LIST OF APPENDICES **xiv**

CHAPTER

1 INTRODUCTION **1**
1.1 General Introduction 1
1.2 Energy Storage System 1
1.2.1 Classification of Energy Storage System 2
1.3 Battery Technology 5
1.3.1 Lithium-Ion Battery 5
1.3.2 Metal-Air Battery 7
1.4 Importance of the Study 9
1.5 Problem Statement 10
1.6 Aim and Objectives 10
1.7 Scope and Limitation of the Study 10
1.8 Contribution of Study 12
1.9 Outline of Report 12
2 LITERATURE REVIEW **13**
2.1 Introduction 13
2.2 Aluminium Anode 13
2.3 Electrolyte 17

	2.4	Cathode	20
		2.4.1 Introduction	20
		2.4.2 Gas Diffusion Layer	20
		2.4.3 Current Collector	21
		2.4.4 Catalyst Layer	21
		2.4.5 Fabrication Method	22
	2.5	Summary	23
3	**METHODOLOGY AND WORK PLAN**		**25**
	3.1	Introduction	25
	3.2	Overall Process Flow Chart	25
	3.3	Fabrication Process	27
		3.3.1 Casing Fabrication	27
		3.3.2 Air Cathode Fabrication	27
		3.3.3 Electrolyte Preparation	28
		3.3.4 Assemble Process	28
	3.4	Taguchi Method	29
		3.4.1 Mass Ratio Composition of Batch 1 Samples	29
		3.4.2 Mass Ratio Composition of Batch 2 Samples	32
	3.5	Prototype Design	33
	3.6	Purchase List	38
	3.7	Experiment Study	39
	3.8	Grey Relational Analysis	40
	3.9	Summary	42
4	**RESULTS AND DISCUSSION**		**43**
	4.1	Introduction	43
	4.2	Batch 1 Samples	43
	4.3	Batch 2 Sample	54
	4.4	Summary	65
5	**CONCLUSIONS AND RECOMMENDATIONS**		**66**
	5.1	Conclusions	66
	5.2	Recommendations for future work	66
REFERENCES			**69**

APPENDICES **74**

LIST OF TABLES

Table 3.1:	Optimization Parameters of Taguchi Method.	30
Table 3.2:	L9 Orthogonal Array.	30
Table 3.3:	Respective Materials Composition according to the L9 Array.	31
Table 3.4:	Mass Needed for Each Material for Each Trial of Batch 1 Samples	31
Table 3.5:	Mass Ratio of Propanol and PTFE in Different Levels	32
Table 3.6:	Mass Needed for Each Material for Each Trial of Batch 2 Samples	33
Table 3.7:	Purchase List of Prototypes.	38
Table 4.1:	Histogram for Sample 4 Plateau Voltage Determination	44
Table 4.2:	Parameters Obtained from Batch 1 Samples	46
Table 4.3:	Specific Capacity of Batch 1 Samples	47
Table 4.4:	GRC for Plateau Voltage of Batch 1 Samples	48
Table 4.5:	GRC for Specific Capacity of Batch 1 Samples	48
Table 4.6:	GRC for Peak Power of Batch 1 Samples	49
Table 4.7:	GRC for Shutdown Current of Batch 1 Samples	49
Table 4.8:	Performance Ranking of Batch 1 Samples	50
Table 4.9:	SNR for Plateau Voltage	51
Table 4.10:	SNR for Specific Capacity	51
Table 4.11:	SNR for Peak Power	51
Table 4.12:	SNR for Shutdown Current	52
Table 4.13:	Mass Ratio of Sample 1, CS 1, Sample 4 and CS 2	53
Table 4.14:	Comparison Table of Sample 1, Sample 4, CS 1 and CS 2 Outputs	53

Table 4.15:	Parameters Obtained from Batch 2 Samples	54
Table 4.16:	Specific Capacity of Batch 2 Samples	55
Table 4.17:	GRC for Plateau Voltage of Batch 2 Samples	56
Table 4.18:	GRC for Specific Capacity of Batch 2 Samples	56
Table 4.19:	GRC for Peak Power of Batch 2 Samples	57
Table 4.20:	GRC for Shutdown Current of Batch 2 Samples	57
Table 4.21:	Performance Ranking of Batch 2 Samples	58
Table 4.22:	SNR for Plateau Voltage	58
Table 4.23:	SNR for Specific Capacity	59
Table 4.24:	SNR for Peak Power	59
Table 4.25:	SNR for Shutdown Current	59
Table 4.26:	Mass Ratio of Sample 16 and MS 1	61
Table 4.27:	Comparison Table of Sample 16 and MS 1 Outputs	63
Table 4.28:	Comparison Table of Sample 15 and MS 1 Outputs	64

LIST OF FIGURES

Figure 1.1:	Theoretical Energy Densities of Metal-Air Batteries.	11
Figure 2.1:	Collected Hydrogen Gas of Various Al Anodes	14
Figure 2.2:	Hydrogen Evolution Rate Comparison for Aluminium Anodes	15
Figure 2.3:	Corrosion Behaviours of Al-Ga, Al-In and Al-Sn Alloys	16
Figure 2.4:	Comparison of Various Types of Electrolytes' Performance	18
Figure 2.5:	Typical Fabrication Method of Air Cathode	23
Figure 3.1:	Overall Process Flow Chart	26
Figure 3.2:	Casing of AAB	27
Figure 3.3:	Fabricated Air Cathode	28
Figure 3.4:	Aluminium-air Battery	29
Figure 3.5:	Exploded View of AAB	34
Figure 3.6:	Overview of AAB in mm	34
Figure 3.7:	Dimension of Aluminium Anode in mm	35
Figure 3.8:	Dimension of Air Cathode in mm	36
Figure 3.9:	Dimension of AAB Casing (Bottom) in mm	37
Figure 3.10:	Dimension of AAB Casing (Front & Back) in mm	37
Figure 3.11:	Dimension of AAB Casing (Side) in mm	38
Figure 4.1:	Discharge Graph of Sample 4	44
Figure 4.2:	LSV Graph of Sample 4	45
Figure 4.3:	Plateau Voltage Value for Various Mass of PTFE and Propanol	60
Figure 4.4:	Peak Power Value for Various Mass of PTFE and Propanol	60

Figure 4.5: Discharge Graph of MS 1 62

Figure 4.6: LSV Graph of MS 1 62

Figure 4.7: Excess Propanol Could Not Absorbed by the Mixture 64

Figure 5.1: Water Leakage Found after Long Period of Operation 67

LIST OF SYMBOLS / ABBREVIATIONS

EVs	electrical vehicles
PHS	pumped hydroelectric storage
SMES	superconducting magnetic energy storage
CAES	compressed air energy storage
SEI	solid electrolyte interface
CMC	carboxymethyl cellulose
PEG	polyethylene glycol
L-Glu	L-glutamic acid
N9	nonoxynol-9
ORR	oxygen reduction reaction
OER	oxygen evolution reaction
GDL	gas diffusion layer
AAB	aluminium air battery
PTFE	polytetrafluoroethylene
SNR	signal-to-noise ratio

LIST OF APPENDICES

Appendix A: Graphs Obtained For Batch 1 Samples 74

Appendix B: Graphs Obtained For Batch 2 Samples 84

CHAPTER 1

INTRODUCTION

1.1 General Introduction

The rapid evolution of electrical vehicles (EVs) and portable electronic devices has led to a huge increment in the high energy density and stability of power source demands. In addition, under the urge of Industry Revolution 4.0, high energy storage systems development is crucial to ensure that the high demands and needs of power usage can be fulfilled when needed while avoiding power waste.

Back in the early 20th century, the era when power stations usually shut down overnight, the importance of the flexible usage of energy storage urged the development of stationary electrical energy storage. After the first energy storage central station of Pumped Hydroelectric Storage (PHS) was initially launched in 1929 and prospered for several decades, it started to slowly run into its waning due to the increment of environmental concern awareness (Chen et al., 2009).

Following that, several factors like the exponential growth of renewable energy and technologies, power quality issues and more severe environmental regulations have led to the rapid growth and development of many electrical energy storage systems. Among the electrical energy storage systems, battery technologies grabbed considerable focus due to their fast response, reliable and stable power supply characteristics. In particular, the metal-air batteries are treated as a future generation due to their low production cost, high power density and lightweight (Wang et al., 2019).

1.2 Energy Storage System

Electrical energy storage stores energy in any form depending on its nature. Then, the stored energy will convert to electrical energy when in use. This enables the generation of electricity to occur during low demand and low production cost, and stored energy can be utilized when high demand, high generation cost or other generation means are not available (Chen et al., 2009).

1.2.1 Classification of Energy Storage System

Electricity can be stored in different forms and converted back to electricity when in use. Due to this characteristic, energy storage systems can be classified into four big categories based on their storage energy form, which are Electrical Energy Storage, Mechanical Energy Storage, Chemical Energy Storage and Thermal Energy Storage (Chen et al., 2009).

1.2.1.1 Electrical Energy Storage

Electrical energy storage can be further classified into Electrostatic Energy Storage and Magnetic/Current Energy Storage.

One of the examples of electrostatic energy storage is the capacitor which stores the electrical energy into the electrical charge on the metal plates. When a capacitor is connected to a DC power source, the capacitor will accumulate energy and create a potential difference by inducing an opposite sign among two metal plates (Chen et al., 2009). Once the potential difference between the metal plates of the capacitor is equal to the voltage output of the power source, the capacitor is fully charged and ready to discharge the electrical energy when connected to the load. The capacitor has an expeditious charge and discharge rate than the batteries with high efficiency as the capacitor just stores the charge while the battery stores the electrical energy via the electrochemical process which consumes more process time. However, capacitors have a lower energy density than other technologies.

Superconducting magnetic energy storage (SMES) can be classified as current energy storage as it is the only known energy storage which stores electrical energy into electric current. SMES stores the energy by inducing the DC to pass through the inductor (coil) which is made from superconducting material like niobiumtitane (NbTi) filaments (Ibrahim, Ilinca and Perron, 2008). Since the flow of electric current in a conducting wire will generate a magnetic field, the SMES is capable of storing the energy as the magnetic field also. SMES system is suitable for constant, full cycling and continuous operation mode applications due to its high energy storage efficiency and rapid response time. However, the application of the SMES system will raise environmental issues due to the strong generated magnetic field. In addition,

the SMES units can be treated as a burden for small industries due to their high cost (Chen et al., 2009).

1.2.1.2 Mechanical Energy Storage

Mechanical Energy Storage stores electrical energy in the form of kinetic energy or potential energy.

Pumped hydroelectric storage (PHS) stores the electrical energy into hydraulic potential energy. A PHS system consists of two reservoirs at different elevations. During the off-peak hours, PHS utilizes electricity to pump the water from the lower reservoir to the higher reservoir. By this, electricity can be stored into potential energy as this amount of water will then return to the lower reservoir and activate the turbine to generate electricity during high demand. Thus, the stored energy amount relies on the height difference between the two reservoirs as well. PHS is the current most used high-power application (above 100 MW) technology with relatively low capital cost compared to the energy output (Ibrahim, Ilinca and Perron, 2008). To build a PHS, several constraints need to be fulfilled and overcome, which are a large available site for 2 reservoirs and dams, and an available budget for high construction cost. Not only that, the rise in awareness of environmental concerns also limits the development of the PHS system (Chen et al., 2009).

Compressed air energy storage (CAES) is another energy storage to provide very large energy besides PHS. During off-peak hours, electrical power is utilized to compress and store the air in a container or cavity. At that period, the electricity is stored in the elastic potential energy of compressed air. Then, during peak hours, the compressed air will be heated and expanded through a high-pressure turbine before the air is further mixed with fuel to feed into the low-pressure turbine. Both turbines are capable of producing electricity as they are all connected to a generator. The construction of the CAES system also relied on the geography constraint. In addition, the CAES system only operates with the connection of a gas turbine plant, other power plants are not capable (Chen et al., 2009).

The spinning momentum of the flywheels can be utilized to store electricity. A motor is needed to spin the flywheel for both the charging and discharging stages. During the charging stage, by supplying electrical power,

the motor will activate and spin the flywheel, and the energy is stored as momentum. During the discharging stage, when the electrical power supply is removed, the momentum of the flywheel will drive the motor as a generator to reproduce electricity (Chen et al., 2009).

1.2.1.3 Chemical Energy Storage

The chemical energy storage generates the electrical energy by transforming the chemical energy obtained via electrochemical reactions. There is a wide range of applications for chemical energy storage technologies, including conventional batteries (lead-acid batteries and lithium-ion batteries), flow-cell batteries, fuel cells, metal-air batteries and even thermochemical energy storage like solar hydrogen and solar metal (Chen et al., 2009).

A battery stores electricity into chemical energy. It consists of anode, cathode and electrolyte which may be in the liquid, paste or solid form. For example, a lead acid battery consists of a lead dioxide cathode, pure lead anode and liquid sulfuric acid electrolyte. During discharging, the lead atom at the anode reacts with sulfate from the electrolyte to produce lead sulfate and free electrons. The electrons will then flow through the wire to the load, and finally flow to the cathode and react with lead dioxide, hydrogen ions and sulfate to form lead sulfate and water. A complete cell reaction is listed as Eqs. 1.1, 1.2, 1.3 and 1.4 below.

At Electrolyte: $$2H_2SO_4 \rightarrow 4H^+ + 2{SO_4}^{2-} \quad (1.1)$$

At Anode: $$Pb + {SO_4}^{2-} \rightarrow PbSO_4 + 2e^- \quad (1.2)$$

At Cathode: $$PbO_2 + 4H^+ + {SO_4}^{2-} + 2e^- \rightarrow PbSO_4 + 2H_2O \quad (1.3)$$

Cell Reaction: $$PbO_2 + Pb + 2H_2SO_4 \rightleftarrows 2PbSO_4 + 2H_2O \quad (1.4)$$

This reaction is reversible for charging. The cost of lead acid is low at the same time provides high efficiency and reliability. However, its drawbacks are a short life cycle, low energy density and poor low-temperature performance (Chen et al., 2009).

Differ from batteries which store energy in a closed system, a fuel cell utilizes the external supplies of fuel and oxidant to produce electricity.

The fuel anode can be hydrogen, hydrocarbons, alcohol or metal. While the oxidant cathode materials can be oxygen, air, chlorine and chlorine dioxide.

For example, a hydrogen fuel cell utilizes hydrogen as fuel and oxygen as an oxidant. With the help of a catalyst, the hydrogen will break into hydrogen ions and free electrons at the anode. The free electrons will flow through the load to produce electricity while the hydrogen ions will react with the oxygen at the cathode to produce water as a sub-product (Chen et al., 2009).

1.2.1.4 Thermal Energy Storage

The thermal energy storage system uses a storage material which has a high energy density and good insulation to keep the high/low temperature. The stored heat energy can be further utilized for heating or cooling and generate electricity with the use of a heat engine cycle.

1.3 Battery Technology

Following the trend of EVs development, lithium-ion batteries and metal-air batteries grab most of the attention of researchers. Till now, lithium-ion batteries have been widely used in the market but at the same time have some space for further improvement. Metal-air batteries are treated as a future trend for research due to their abundant cathode source. Some of the inexpensive anode materials like aluminium, magnesium and iron are also an attractive edge for researchers (Rahman, Wang and Wen, 2013).

1.3.1 Lithium-Ion Battery

Lithium-ion batteries, one of the most popular types of batteries in the small portable device market which were first commercialised by Sony in 1990, have an excellent energy density, life cycle and high efficiency. These characteristics enable lithium-ion battery widen the gap with other batteries and control over 50 % of the small portable devices market. However, the special packaging and internal protection circuits also impede the production process and lead to high costs (Manthiram, 2017).

1.3.1.1 Working Principle

A lithium-ion battery consists of a lithiated metal oxide cathode which can be made from $LiCoO_2$, $LiMnO_2$ and $LiNiO_2$, a cathode which can be graphite or other carbons and a lithium salt electrolyte (Manthiram, 2017).

When the lithium-ion battery is first charged, the power source will lead the lithiated metal oxide in the cathode to break into lithium-ion, free electrons and metal oxide. The electrons will then flow through the charging power source and the lithium ion will flow through the electrolyte to the anode to form the lithiated carbons. The process will then be reversed during the discharging process when the power source is replaced by a load. The complete cell reaction is stated as Eqs 1.5, 1.6 and 1.7 as below by considering a $LiMnO_2$ cathode and graphite anode (Chawla, Bharti and Singh, 2019).

At Cathode: $$LiMnO_2 \rightleftarrows Li^+ + MnO_2 + e^- \quad (1.5)$$

At Anode: $$C_6 + Li^+ + e^- \rightleftarrows LiC_6 \quad (1.6)$$

Cell Reaction: $$LiMnO_2 + C_6 \rightleftarrows MnO_2 + LiC_6 \quad (1.7)$$

1.3.1.2 Performance

In the past 25 years, graphite has become a favourable material as an anode of commercial lithium-ion batteries. When the cell is first charged, lithium-ion which passes through the electrolyte and brings along the solvent molecules will lead to the formation of a solid electrolyte interface (SEI) layer by reacting with the graphite at the anode. The SEI layer can prevent direct contact between the electrons and electrolyte, and therefore avoid electrolyte degradation and provide a long life with high stability.

The cathode of a lithium-ion battery may be made from layered structure $LiMO_2$ where M can be Mn, Co and Ni, spinel $LiMn_2O_4$, and olivine $LiFePo_4$. Among the three types of materials, the layered lithiated metal oxide provides the highest energy density as the layered structure can provide the highest practical capacity up to 180 Ah/kg (Manthiram, 2017).

Till now, commercial lithium-ion battery technologies are limited to a maximum of 250 Wh/kg of cell gravimetric energy densities and maximum volumetric energy densities of 650 Wh/L (Manthiram, 2017). To make improvements, the materials used for cell components and cell fabrication

engineering are the two important sectors to focus on. This is because all performance parameters such as energy density, safety, cost, cycle life and charge-discharge rate all depend on the component materials.

1.3.1.3 Advantages and Limitations

In short conclusion, lithium-ion batteries are capable of providing large energy density, long cycle life, high efficiency in a compact and portable design. This led to its dominant position in the small portable device industries. However, due to its irreversible and unpredictable nature, the usage of lithium-ion batteries may raise several safety concerns under abuse conditions such as thermal runaway, overheating, overcharge or over-discharge, deformation, collision and shock. Furthermore, the flammable electrolyte can lead to explosion as well. In the electric vehicles sector, recent studies show that around 0.5-1 kWh/kg of energy density is needed to drive 500 km (Felipe, Kumar and Gupta, 2023). As the theoretical energy density of lithium-ion batteries is 0.387 kWh/kg, which is not capable of fulfilling the demand, a new energy storage with high energy density is necessary to be implemented (Bruce et al., 2011).

1.3.2 Metal-Air Battery

A metal-air battery consists of a metal anode, air cathode and electrolyte. The characteristic of a metal-air battery that utilizes the oxygen from the surrounding air to undergo an electrochemical process leads to its advantages of lightweight and compact design (Li and Lu, 2017). Currently, the rechargeability of metal-air batteries is still under development due to the low practical energy density which is not comparable with lithium-ion batteries. Ideally, the development of secondary metal-air batteries may rely on the non-aqueous electrolyte.

Generally, an M anode metal which having the n oxidation number of a metal-air battery will be oxidized at the anode to generate metal ions and electrons. While at the cathode, the oxygen from the air will be reduced to generate hydroxide ions as shown in Eqs 1.8 and 1.9 below (Li and Lu, 2017).

At Anode: $$M \rightarrow M^{n+} + ne^{-} \quad (1.8)$$

At Cathode: $$O_2 + 2H_2O + ne^{-} \rightarrow 4OH^{-} \quad (1.9)$$

1.3.2.1 Li-Air Battery

Based on the electrolyte of the cell, lithium-air batteries can be classified into 4 categories, which are aqueous electrolytic type, aprotic/non-aqueous electrolytic type, mixed/hybrid electrolytic type and solid electrolytic type. Depending on the electrolyte used, the corresponding electrochemistry of the cell will differ (Rahman, Wang and Wen, 2013).

Lithium-air batteries have a larger energy density than conventional lithium-ion batteries. As lithium is very reactive, similar to lithium-ion batteries, lithium-air batteries also raise several safety concerns. The likelihood of the dendrite formation occurrence will also reduce the specific capacity, coulombic efficiency and cycling stability (Tomar, Sakshee Chandel and Alok Kumar Rai, 2023).

1.3.2.2 Zn-Air Battery

A zinc-air battery uses zinc metal to be the anode material. The hydrogen evolution reaction will occur when the zinc corrodes in the alkaline electrolyte, following the reaction listed as Eq 1.10 below:

$$Zn + 2H_2O \rightarrow Zn(0H)_2 + H_2 \quad (1.10)$$

In addition, the effect of activation, ohmic and concentration loss affect the practical working voltage of a zinc-air battery to be less than 1.65 V (Rahman, Wang and Wen, 2013). This leads to the usage of zinc-air batteries being mostly limited for low power usage. As a secondary battery, the poor performance (<60 % energy efficiency) also states that the rechargeability of the metal-air battery still needs to be further investigated (Li et al., 2023).

1.3.2.3 Al-Air Battery

Due to the low production cost, high theoretical energy and specific capacity, aluminium is one of the best materials for the fabrication of metal-air anode.

An aluminium-air battery consists of an aluminium anode, air cathode which is also called a gas diffusion electrode) with catalysts and electrolytes (Olabi et al., 2021).

During discharging, the aluminium will break into free electrons and aluminium ions which will later react with hydroxide ions to form aluminium hydroxide. When the free electrons pass through the load and finally reach the cathode, they will react with water molecules from the electrolyte and oxygen from the air to form hydroxide ions, which the hydroxide ions will flow to the anode to react with the aluminium ions as discussed previously. The complete cell reaction is stated in Eqs 1.11, 1.12, 1.13 and 1.14 below (Egan et al., 2013).

At Anode: $$Al \rightarrow Al^{3+} + 3e^{-} \quad (1.11)$$

$$Al^{3+} + 3OH^{-} \rightarrow Al(OH)_3 \quad (1.12)$$

At Cathode: $$O_2 + 2H_2O + 4e^{-} \rightarrow 4OH^{-} \quad (1.13)$$

Cell Reaction: $$4Al + 3O_2 + 6H_2O \rightarrow 4Al(OH)_3 \quad (1.14)$$

For a common primary aluminium-air battery, when all the aluminium atoms become aluminium hydroxide, a new anode needs to be replenished for further usage.

1.4 Importance of the Study

The aluminium-air battery is treated as one of the future trends for development due to its advantages towards sustainable development. This is stated as because the materials needed to fabricate the battery are either reusable or environmental friendly. For example, the casing and aluminium anode are reusable, while the cathode and electrolyte are made from carbon and alkaline, where the alkaline is the raw material for the fabrication of soap and carbon is the common material that can be simply obtained from daily life.

Thus, this project may deliver a positive impact towards the development of aluminium air batteries by first providing a basic understanding of the principles of aluminium air batteries. Then, this project is capable of providing guidelines and suggestions on the optimization of material composition for aluminium air cathode fabrication. Lastly, the

obtained results in this project can suggest the focus direction of future development of aluminium air batteries.

1.5 Problem Statement

The air cathode of the primary aluminium air batteries plays a crucial role in controlling the ORR and OER process for the discharge process. However, most of the researchers are mainly focusing on the development of additives of electrolyte and aluminium anode. To improve the performance of AAB, there is a lack of information on the air cathode optimization, especially for the material composition of the air cathode.

1.6 Aim and Objectives

The main aim of the research is to optimize the fabrication of air cathodes to improve the performance of aluminium air batteries. This can be achieved by several specific objectives of this research:

- To determine the optimal material composition of air cathode via Taguchi Method.
- To fabricate the aluminium air batteries.
- To evaluate the performance of aluminium air batteries.

1.7 Scope and Limitation of the Study

The scope of the project will focus on the optimization of the material composition of air cathode by determining the optimal mass ratio of each material for air cathode fabrication. Thus, several prototypes will be fabricated and subsequence experiments will be carried out to evaluate the performance. Due to the size nature of the prototype, the fabricated aluminium air battery will only be capable of miniature application.

As the Taguchi method is utilized in the optimization of the mass ratio of each material, the use of the L9 orthogonal array will lead to the restriction of the number of investigated factors of each material. For example, the mass ratio of carbon black only varies in the value of 8, 9 and 10 in the project, other mass ratio values of carbon black are not taken into consideration.

Similarly, the use of orthogonal array can save time and cost by reducing the number of trials or experiments, however, it also sacrifices a small amount of accuracy compared to the outcomes obtained via full factorial experiments (Cimbala, 2014).

Among all energy storage systems, lithium-ion batteries provide better performance and therefore dominate the market. Their remarkable advantages such as high efficiency, low self-discharge rate and long cycle life have led them to be widely used in various markets including the significant trend in future, electric vehicles (EVs). However, there are still several lingering concerns for the public regarding the safety of lithium-ion batteries. For example, thermal runaway is led by the uncontrollable and irreversible nature, overcharge or over-discharge and overheating (Tran et al., 2022). In addition, to achieve high capacity (minimum 200 $mAhg^{-1}$) and safety requirements for EVs, it is undeniable that lithium-ion batteries are still facing some challenges (Wang et al., 2019).

Metal-air batteries are treated as a trend to replace lithium-ion batteries and have more focus on their development due to their low production cost, lightweight, compact design and environmentally friendly. In addition, metal-air batteries have a larger theoretical energy density (1.2–11.4 kWh/kg) than lithium-ion (0.387 kWh/kg) (Bruce et al., 2011) as shown in Figure 1.1 (Li and Lu, 2017).

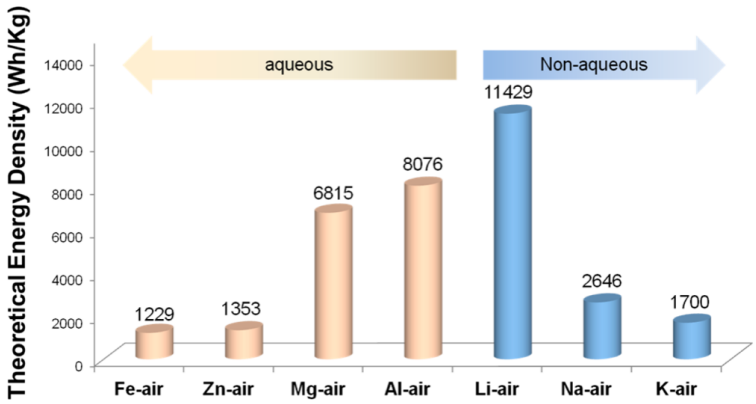

Figure 1.1: Theoretical Energy Densities of Metal-Air Batteries. Adapted with Permission (Li and Lu, 2017). Copyright 2017. American Chemical Society.

Since aluminium is abundant, a lower production cost aluminium-air battery which is capable of providing high energy density and capacity will be the main focus in this study. A detailed aluminium-air battery construction will be discussed and the optimum material compositions on the air cathode will be investigated.

1.8 Contribution of Study

This project proposed five materials to fabricate the air cathode of AAB, which are carbon black, activated carbon, manganese (IV) oxide, propanol and PTFE. In addition, to fulfil the demand of optimizing the material compositions of the air cathode, this project will determine the optimal mass ratio of each material. The outcomes of the study may deliver insight for future development by suggesting the focus direction based on the result obtained.

1.9 Outline of Report

This report consists of 5 main parts. First of all, Chapter 1 introduction stated the background of the research topic, identified the problem statement and thus set the aim and objectives of this project. Then, a detailed literature review is carried out to build the necessary knowledge regarding the project. In this case, since the project is optimizing the material compositions of the air cathode, the review of all components of AAB, including aluminium anode, electrolyte and air cathode is discussed in Chapter 2. The Chapter 3 methodology and work plan provides a complete guide to carry out the project. Then, the obtained results and subsequent analysis are stated in Chapter 4. Lastly, the Chapter 5 concludes the project and also provides some suggestions for future development.

CHAPTER 2

LITERATURE REVIEW

2.1 Introduction

Aluminium air batteries gained a lot of focus on development due to their high theoretical energy (8.1 kWh/kg), acceptable theoretical voltage (2.71 V) and practical voltage (1.2-1.6 V) (Li and Zhang, 2023).

As one of the metal-air batteries, the aluminium air battery also adopts the same characteristic which utilizes ambient air as the source for the cathode. By this, the weight of the product can be reduced and the production cost will be lowered. As shown in Figure 1.1, among other anode metals such as Li, Na, K, Ca, Mg and Zn, aluminium air batteries have a higher specific capacity except for Li. However, aluminium is very abundant compared to Li which is very hard to be obtained. In addition, aluminium is believed to be safer than Li as Li is very reactive. The abundance of aluminium is further reducing the cost and thus led it to be the most attractive candidate for researchers (Buckingham, Asset and Atanassov, 2021).

The aqueous alkaline electrolyte is the most widely used electrolyte for aluminium-air batteries, hence it will be the electrolyte used in this paper also which the respective reason will be discussed later. However, it also led to drawbacks which the self-discharge and corrosion since aluminium is reactive in alkaline and a large amount of hydrogen gas will be released at the anode (Cho et al., 2015).

2.2 Aluminium Anode

The anode material of the aluminium air battery can be pure aluminium or aluminium alloys. There are several grades to classify aluminium alloys based on their composition and different grades will lead to their characteristic.

Pure aluminium has high electrical conductivity but also suffers from self-discharge and corrosion issues when immersed in an alkaline solution. To resolve this problem, researchers recommend the usage of aluminium alloy, which several additives are recommended: Mn, Mg, Cr, Zn and Ti. 1000 series aluminium alloy requires at least 99 % of pure aluminium. It is capable of high

conductivity. 2000 series aluminium contains 2-10 % of copper. 3000 series aluminium alloys contain 1.5-4.5 % of manganese (metals4u, n.d.). Mn is treated as one of the elements of anti-rust, the performance can be further optimized by adding the Sn element which is proven by recent studies as shown in Figure 2.1, the Al-Mn-Sb collected hydrogen gas is the lowest value among the others when the aluminium anode is immersed in 4M KOH.

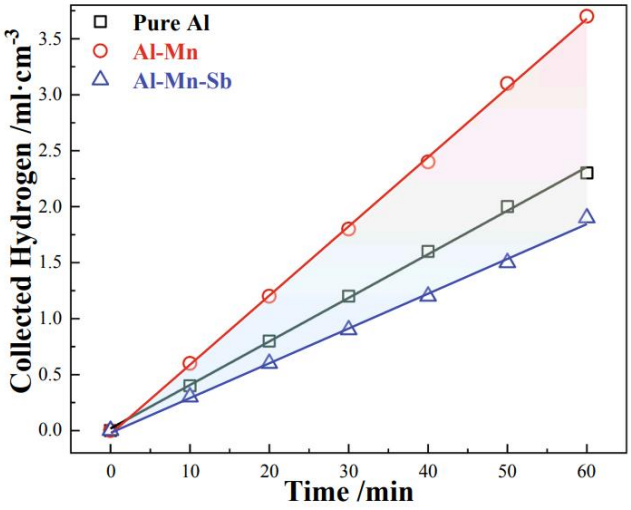

Figure 2.1: Collected Hydrogen Gas of Various Al Anodes
Adapted with Permission (Liu et al., 2021). Copyright 2021. Elsevier.

4000 series aluminium alloys also known as silicon alloys. Silicon is added to lower the melting point of the alloy at the same time maintain its ductility. 5000 series alloys contain magnesium, but are usually added on with additional elements, for example, chromium or manganese. It has a higher corrosion resistance. 6000 series alloys contain both silicon and magnesium. 7000 series aluminium alloys contain zinc as the primary agent with a few other metals like magnesium. A strong and hard alloy which is commonly used in the aerospace industry. 8000 series alloys refer to other alloy categories which may contain various elements like lithium and iron. 8000 series alloy has similar properties to 1000 series alloy, but in stronger condition.

Cho et al., 2015 compared the performance of two pure Al (grade 4N 99.99 % purity and grade 2N5 99.5% purity) in 4M NaOH solution. As a

result, 4N grade Al has higher corrosion resistance value than 2N5 grade Al. This can be shown by the corrosion rate obtained, in which the corrosion rate of 4N Al (465.59 mm/year) is lower than 2N5 Al (577.4 mm/year).

The aluminium alloy has having lower corrosion rate than pure aluminium and the corrosion rate can be further reduced and optimized using a suitable amount of additives. The findings of Gao et al., 2019 agreed with the statement. Gao et al. tested and compared the performance of pure Al (grade 4N6 Al) and 5000 series Al alloy (Al-2Mg alloy) in 6M NaOH. As a result, the 0.159 $mLcm^{-2}min^{-1}$ hydrogen evolution rate of Al-2Mg alloy is lower than that of 4N6 Al which is 0.278 $mLcm^{-2}min^{-1}$. In addition, the hydrogen evolution rate can be further reduced to 0.015 $mLcm^{-2}min^{-1}$ when added 0.05 M of Na_2SnO_3.

The effect of Mg towards the anode performance can be further supported by the findings of Zhou et al., 2020. The performance of the pure aluminium, Al-Sn-Ga and Al-Sn-Ga-Mg in 4M NaOH solution is tested. The weight percentage of Sn and Ga for aluminium alloys are maintained at 0.08 wt% while the Mg content for the respective alloys varies from 0.5, 1.0, 1.5 to 2.0 wt%. As a result, as shown in Figure 2.2, pure aluminium shows the highest hydrogen evolution rate and Al-Sn-Ga-1.0Mg has the lowest hydrogen evolution rate.

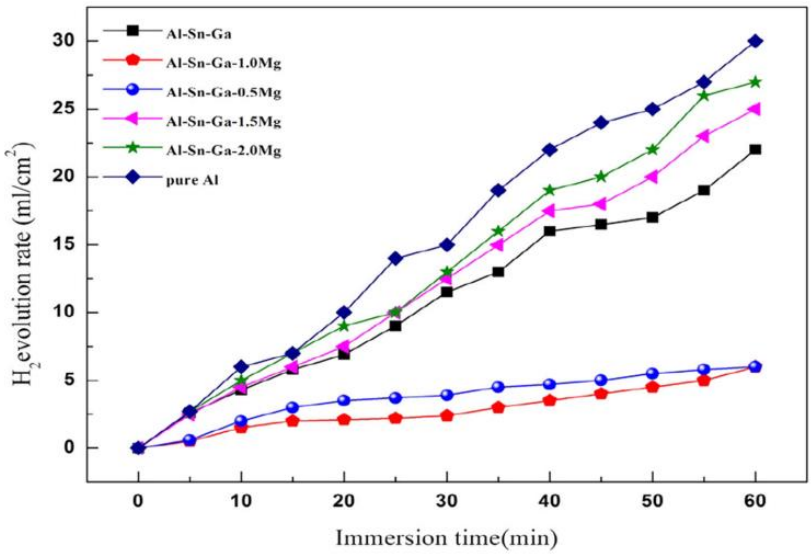

Figure 2.2: Hydrogen Evolution Rate Comparison for Aluminium Anodes Adapted with Permission (Zhou et al., 2020). Copyright 2020. Springer Nature.

Knowing that the higher purity of aluminium will result in a relatively higher corrosion rate when immersed in alkaline electrolyte, additives are definitely needed to improve the performance. However, the excess or inadequate addition of alloying elements will also lead to parasitic corrosion. For example, iron is believed to increase the corrosion rate.

The investigation of the aluminium alloy to obtain better performance has been carried out for a few decades. Ga, In and Sn were believed to be the alloying elements that lead the Al alloys more active than pure Al. Buckingham, Asset and Atanassov, 2021, combine several researchers' findings to investigate the effect of Ga, In and Sn in binary, ternary and quaternary alloys. To learn the behaviour of ternary and quaternary alloys, Hunter, 1989 as cited by Buckingham, Asset and Atanassov, 2021, proposed that the "dominance effect" of the alloys is controlled by a dominant element, which Sn is the most dominant element among the others following by In, and Ga is the least dominance. This statement is also supported by Scamans et al. In general, Al-In and Al-Sn alloys have lower corrosion rates than Al-Ga alloys. This can be supported by the experimental findings of Hunter, 1989 and Macdonald et al., 1988 as cited by Buckingham, Asset and Atanassov, 2021 as shown in Figure 2.3.

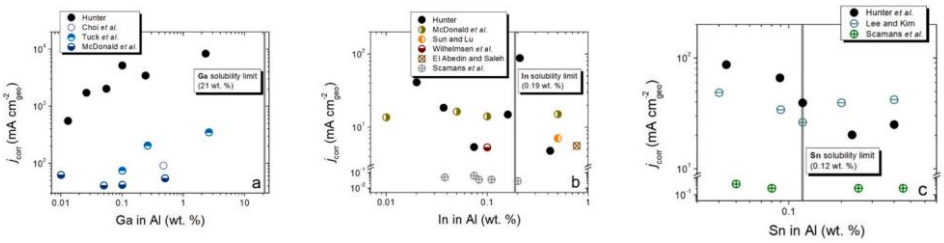

Figure 2.3: Corrosion Behaviours of Al-Ga, Al-In and Al-Sn Alloys Adapted with Permission (Buckingham, Asset and Atanassov, 2021). Copyright 2021. Elsevier.

According to Buckingham, Asset and Atanassov, 2021, the effect of Ga towards the anode performance is still unclear and the researchers still haven't reached to consensus. It is because several findings showed that Ga is not suitable to be the alloying metal for aluminium anode as the corrosion rate increases when the Ga content increases. In addition, the least impact of Ga for

ternary and quaternary alloys (i.e. Al-Ga-In ternary alloy has similar performance with Al-In binary alloy) also leads the researcher to conclude the statement. However, some findings conversely show the effect of Ga towards the aluminium anode behaviour. Scamans et al. as cited by Buckingham, Asset and Atanassov, 2021, stated that 0.012 % of Ga is a strong inhibitor of corrosion in Al-Ga-In alloy. Thus, the variation of results shows that more research is still needed for the development of Ga addition.

Not only that, Goel, Dobhal and Sharma, 2020 concluded that Zn has had a positive impact on increasing battery performance and the presence of Fe and Si shall be avoided for the same purpose after combining several researcher's works. This can be supported by the findings of Ma et al., 2014 which two aluminium alloys, alloy 1(Al−1Mg−0.1Ga−0.1Sn) and alloy 2 (Al−1Mg−1Zn−0.1Ga−0.1Sn) are tested in various electrolytes. As a result, the charge-transfer resistance values of the equivalent circuit for alloy 2 are higher than alloy 1 in 4M NaOH and 7M KOH solution. This indicates that the exchange current values which are directly associated with the corrosion electrochemical process of alloy 2 are lower in both solutions and thus have a lower corrosion rate. In addition, the obtained data also shows that the cell potential performance of alloy 2 is better than alloy 1 in NaCl and NaOH solutions.

2.3 Electrolyte

The electrolyte of metal-air batteries can be either aqueous, non-aqueous or hybrid. In this paper, only aqueous alkaline electrolytes will be discussed further.

Aqueous electrolytes can be further classified into acidic electrolytes, neutral electrolytes and alkaline electrolytes based on the pH value. The aqueous electrolyte, especially the alkaline electrolyte is widely used for the fabrication of aluminium air batteries. Generally, the attractive advantages of the aqueous electrolyte include inflammable characteristics due to the presence of water inside the electrolyte and relatively high power density (Buckingham, Asset and Atanassov, 2021).

According to Figure 2.4, the acidic electrolyte has the lowest aluminium corrosion rate among others. However, acidic electrolyte suffers

from poor battery efficiency as the large amount of H^+ ions will react directly with aluminium metals and thus reduce the source to generate electricity.

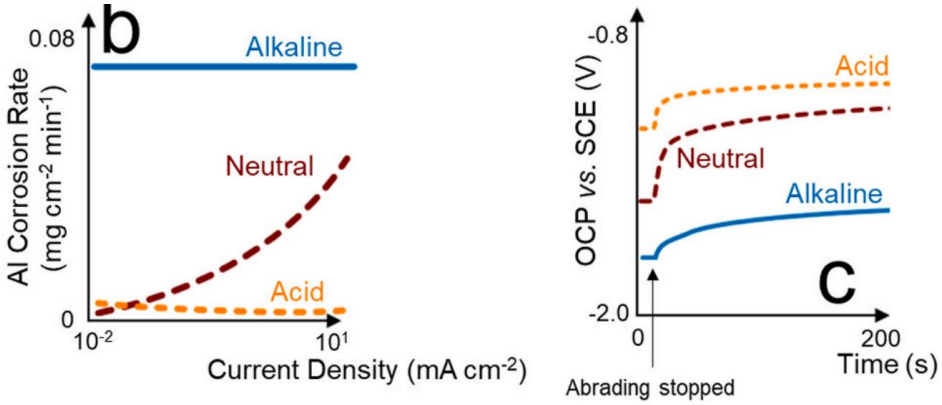

Figure 2.4: Comparison of Various Types of Electrolytes' Performance Adapted with Permission (Buckingham, Asset and Atanassov, 2021). Copyright 2021. Elsevier.

The neutral electrolyte has a lower corrosion rate than alkaline however the conductivity is also poorer. The alkaline electrolyte is commonly used for aluminium air battery production as it provides higher theoretical cell potential and achievable power. In addition, as shown in Figure 2.4, it provides the larger open circuit potential than acidic and neutral electrolytes. For the selection of an alkaline electrolyte, KOH and NaOH can be taken into consideration. However, KOH is more recommended as it is relatively better due to its lower viscosity and higher ionic conductivity (Wang et al., 2019; Olabi et al., 2021).

Although alkaline electrolytes have a lot of advantages which lead it to be the most common electrolyte, it also has some drawbacks. As aluminium is reactive in alkaline solution, the corrosion of the aluminium anode will lead to the formation of a hydroxide surface as following the parasitic reaction stated in Eq 2.1 below (Tan et al., 2023):

$$2Al + 6H_2O \rightarrow 2Al(OH)_3 + H_2 \qquad (2.1)$$

The corrosion of the aluminium is due to the reaction between aluminium and water presence in the aqueous electrolyte to release hydrogen

gas. Thus, when some of the pure aluminium is consumed for the parasitic reaction, the amount of aluminium reacts with hydroxide ions to release free electrons will be decreased and thus affect the cell performance.

In addition, an aluminium air battery consumes an aluminium anode to produce electricity. During the discharging process, the pure aluminium element from the anode will react with hydroxide ions to form aluminium hydroxide and release free electrons. However, the parasitic reaction also consumes aluminium anode to form aluminium hydroxide without producing free electrons. Thus, the parasitic reaction has fastened the aluminium anode consuming rate and reduced the aluminium air battery lifespan. Therefore, it is crucial to inhibit the evolution of hydrogen gas to improve its efficiency. This can be achieved in several ways, one of them may be adopting aluminium alloys as an anode which has been discussed earlier as the additives are capable for metal alloys to suppress the generation of hydrogen.

The functions of electrolytes are mainly suppressing corrosion, lowering the hydrogen evolution rate and thus increasing the anode utilization. For further improvement, Mori, 2020 proposed several additives that can be added, for example, Zn^{2+}, Sn^{3+}, and In^{3+} can be used for neutral electrolytes, ZnO and polyethylene glycol for the alkaline electrolyte. According to Mori, 2020, this statement can be further supported by the works of different researchers. For example, Liu et al. tested the effect of CMC (carboxymethyl cellulose) and ZnO additives in NaOH solution and Wang et al. tested the performance of polyethylene glycol and ZnO in KOH solution. Wang et al., 2010 tested the inhibition effect of zinc oxide (ZnO) and polyethylene glycol (PEG) on the corrosion of pure aluminium electrodes in 4 M KOH solution. As a result, 0.2 M ZnO and 2 mM PEG showed a strong inhibition effect on corrosion in the value of 98.8 % corrosion inhibition efficiency. In addition, Wang et al. also tested the performance of the prototype. The data showed that the relatively high current density of 40 mA/cm^2, 0.2 M ZnO and 2 mM PEG led to a longer discharge period of 7.5 hours at the same time in a relatively low electrode potential below 1 V. This showed a good discharge performance can be obtained by utilizing the ZnO and PEG additives. As a result, both cases showed that the respective additives are capable of reducing the corrosion rate of the aluminium anode.

Furthermore, the organic additives can also reduce the corrosion rate effectively (Goel, Dobhal and Sharma, 2020). For example, Zhang et al. tested three different dicarboxylic acids (succinic acid, adipic acid and sebacic acid) as additives for alkaline electrolytes. As a result, three of them suppress the evolution of hydrogen, especially adipic acid which has the most prominent performance. Nevertheless, Wang et al. tested the rare earth complex organic additives (L-cysteine and cerium nitrate) in an alkaline electrolyte by utilising a 5052-aluminium alloy as the anode. The result showed the ability of these organic additives to inhibit the anode self-corrosion at the same time maintain the anodic electrochemical performance.

The inhibition effect of cathodic-type inhibitors was also investigated. Kang et al., 2019 tested the performance of cerium acetate ($Ce(CH3COOH)_3$) and L-glutamic acid (L-Glu) on corrosion inhibition. The result shows that 10 mM of cerium acetate and 8 mM of L-Glu can strongly inhibit the corrosion of aluminium anode which is made by Al-0.5Mg-0.1Sn-0.1Ga alloy in 4M NaOH with 77.85 % inhibition efficiency. However, these cathodic inhibitors will slightly affect the anode activity also. Another cathodic inhibitor, nonionic surfactant (nonoxynol-9, N9), was tested by Deyab, 2019 for the performance of pure aluminium electrodes in 4 M NaOH. As a result, 2 mM of N9 gave the most optimum inhibition efficiency in the value of 85.6 %.

2.4 Cathode

2.4.1 Introduction

An air cathode of the aluminium air batteries comprises three components, which are the gas diffusion layer, current collector and catalyst layer. Air cathode is essential for oxygen gas transfer to carry on cathode reactions, oxygen reduction reaction (ORR) and oxygen evolution reaction (OER), in which ORR occurs for discharging while OER occurs for charging (applicable for secondary aluminium air battery) (Liu et al., 2020).

2.4.2 Gas Diffusion Layer

The gas diffusion layer (GDL) is crucial for oxygen diffusion; hence it shall be thin and porous to obtain good performance. In addition, since the aqueous electrolyte is used, the GDL shall be hydrophobic as well which can be

achieved by adopting hydrophobic binders such as PTFE, FEP or PVDF. However, keep in mind that excess hydrophobic agents will also lead to the reduction of porosity and oxygen diffusion, and thus affect the cell performance. Hence, the percentage of hydrophobic agents is recommended to be 30-70 wt% (Liu et al., 2020).

Aleksandrs Vališevskis et al., 2019 suggested and tested several materials for the GDL fabrication. The first sample is an embroidered cathode pack inserted with carbon granules while a 3 mm thick nonwoven fabric of carbon impregnated is utilized as the second sample. As a result, the first sample is more recommended as a higher open circuit voltage (680 mV > 500 mV) and a short circuit current (35 mA > 13 mA) is obtained compared with the second sample.

2.4.3 Current Collector

The current collector is used to collect electrons. Normally, the current collector can be either metal or non-metal. However, as a current collector is normally placed outside the catalyst layer, which oxygen is needed to flow through to the catalyst layer to carry out ORR or OER, the current collector shall be made from porous metal foam (nickel, copper or stainless steel) or carbon-based materials (carbon cloth, graphitic paper or conductive carbon paper).

Despite a typical Ni mesh, copper wire and stainless steel wire mesh, Aleksandrs Vališevskis et al. also proposed several materials which having similar performance that can be purchased from industry, for example, Shieldex Budapest conductive textile and Shieldex Nora PW conductive textile.

2.4.4 Catalyst Layer

The catalyst layer is an essential component for the air cathode to occur ORR and OER. To fasten the oxygen reactions, the bifunctional electrocatalyst is needed. The electrocatalyst may be noble metals and alloys, metal oxides, metal hydroxides or carbon materials.

A noble metal or alloy can be a good electrocatalyst for an aluminium air battery. Pt, Pd, Au and Ag are suitable candidates due to their likelihood to

absorb the reactant molecule to occupy the vacant d-orbitals (Mori, 2020). Among them, Pt is the most commonly studied noble metal catalyst due to its excellent catalytic performance. However, the limited natural resources of Pt elements are often a big challenge and lead to high production costs. Hence, the usage of Pt alloys which can slightly reduce the need for pure Pt can be considered. In fact, Wang et al. found that Pt alloys are actually having a higher catalytic activity than pure Pt, thus Pt alloys are a good alternative to pure Pt.

The alternative usage of pure Pt by Pt alloys still consumes the Pt resources, yet the scarcity of Pt still exists. The abundant transition metal oxides are one of the good choices as electrocatalysts. Manganese is one of the most popular selections for catalysts (Goel, Dobhal and Sharma, 2020). In addition, carbonaceous nanomaterials like graphene, graphite and carbon nanotubes are also a better choice to eliminate the huge usage of Pt (Mori, 2020; Goel, Dobhal and Sharma, 2020). Several researchers have also proven the ability of these low-cost carbon-based catalysts. For example, Ganesan et al., 2015 tested the electrochemical measurements of different composite samples of cobalt sulfide/graphene oxide hybrid material prepared at 400, 500 and 600 degrees Celsius. As a result, these 3 samples give a maximum of 1.63 V for OER at 10 $mAcm^{-2}$ and 0.79 V for ORR at -3 $mAcm^{-2}$. As a reference, Ganesan et al. reported the performance of MnO_2 for comparison, which showed a similar performance (1.77 V for OER, 0.73 V for ORR) with the composite samples.

2.4.5 Fabrication Method

According to Liu et al., 2020, there are two ways of fabrication methods to produce the GDL. The first method is blending PTFE with carbon black, acetylene black, activated carbon or carbon fiber in alcohol. Then, the pasty mixture will be rolled into film after it is dried and attached to the current collector. Another way to fabricate GDL is to directly use the porous PTFE film. Depending on the electrolyte used, the design of GDL may vary. For example, a hydrophobic catalyst layer can even directly be treated as GDL for neutral electrolytes.

For the catalyst layer, conventionally, the catalyst will be bonded with the substrate by binder PTFE via spraying method, inkjet printing or screen printing. A schematic diagram of a typical fabrication method of air cathode is shown in Figure 2.5.

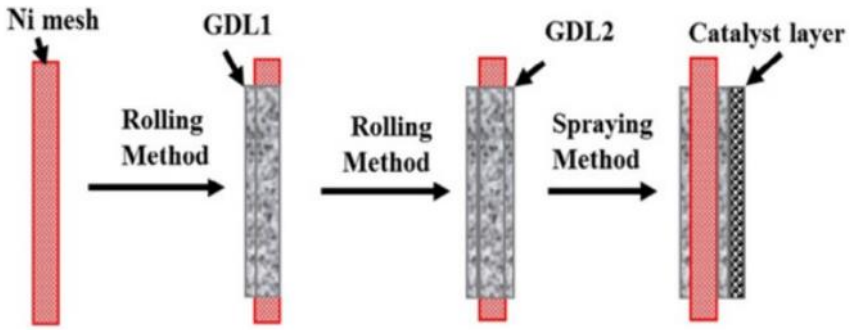

Figure 2.5: Typical Fabrication Method of Air Cathode
Adapted with Permission (Zhang et al., 2019). Copyright 2019. John Wiley and Sons.

The GDL and catalyst layer are often fabricated together and the selection and composition of the materials may be varied. For example, Zhang et al. fabricated the sample with 7 wt% of MnO_2 catalyst, 77 wt% of activated carbon powder and 16 wt% of PTFE binder. Nit Namwong and Chaiyaput Kruehong, 2022 remarked on the usage of chain-like carbon nano-onions (CNCLOs) as air cathodes due to the remarkable results obtained. The air cathode which is made up of the synthesized CNCLOs on nickel foam provides a higher cathode-to-anode ratio, 1108 $mAhg^{-1}$ of specific capacity and 584 $Whkg^{-1}$ of energy density.

2.5 Summary

From the literature review, to obtain high corrosion resistance, 5000 series aluminium alloy is selected as the material for aluminium anode. The aqueous KOH electrolyte is selected as well for better performance since the KOH electrolyte is capable of providing high achievable power and large open circuit potential. From the literature review, it can be seen that there is a

limited resources available regarding the fabrication materials of air cathode. In addition, the weight percent for each material determined from current published works are difficult to show the general trend or relationship to follow. Thus, by referencing from the journals discussed above, the carbon powder used to fabricate the air cathode in this project is set to be carbon black and activated carbon to increase other material combination probabilities for development. The other materials to fabricate the air cathode include manganese (iv) oxide acts as a catalyst, PTFE acts as a binder and Propanol acts as a solvent or processing agent to mix all the powder together.

CHAPTER 3

METHODOLOGY AND WORK PLAN

3.1 Introduction

This chapter will discuss the workflow of the project, the fabrication of prototypes and the experiment study.

This experiment aims to optimize the material compositions of the air cathode of an aluminium-air battery. 5 materials that were chosen to fabricate the air cathode are Carbon Black, Activated Carbon, Manganese (IV) Oxide, Propanol and PTFE. The mass composition of these five materials was proposed by using the Taguchi Method. To ease the investigation of the effect of these materials, the aluminium-air battery samples fabricated in this experiment are divided into two batches. The first batch sample aims to optimize the mass ratio of materials Carbon Black, Activated Carbon and Manganese (IV) Oxide at the same time maintaining the same value of the mass ratio of Propanol and PTFE. Then, from the result of batch 1 samples, the optimized mass ratio of Carbon Black, Activated Carbon and Manganese (IV) Oxide will be brought forward to batch 2 samples. For the batch 2 sample, the mass ratio of Carbon Black, Activated Carbon and Manganese (IV) Oxide will be set to be the same as the optimized result of batch 1 samples while varying the mass ratio of Propanol and PTFE for optimization.

Several experiments will be carried out to evaluate the cell performance, which is the discharge test and LSV test. Consequently, all batch 1 or batch 2 samples, all the tested samples will be ranked using Grey Relational Analysis to determine the optimized mass ratio of each material.

3.2 Overall Process Flow Chart

The overall process flow chart of this project is shown in Figure 3.1.

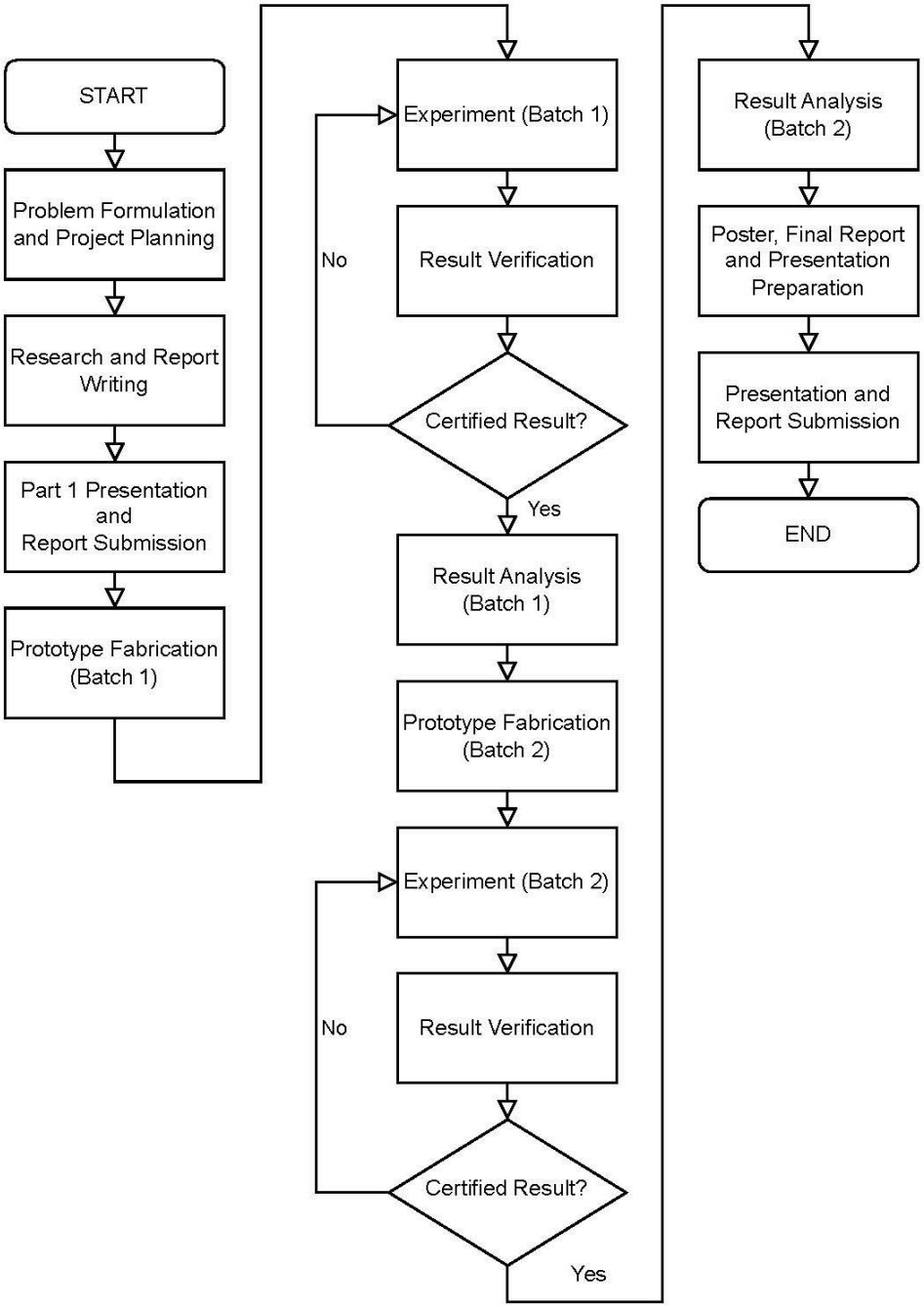

Figure 3.1: Overall Process Flow Chart

3.3 Fabrication Process

The fabrication process of the prototype may be divided into 4 categories, which include aluminium-air battery casing fabrication, air cathode fabrication, electrolyte preparation and assembly process.

3.3.1 Casing Fabrication

The prototype casing is made from the 6 mm thickness purchased acrylic board. First, the 2D drawing of each component of the casing is drawn and converted to a DXF file for laser cutting in the UTAR workshop. After all the acrylic board pieces were cut, all the components were stuck together to form the casing by using chloroform as shown in Figure 3.2.

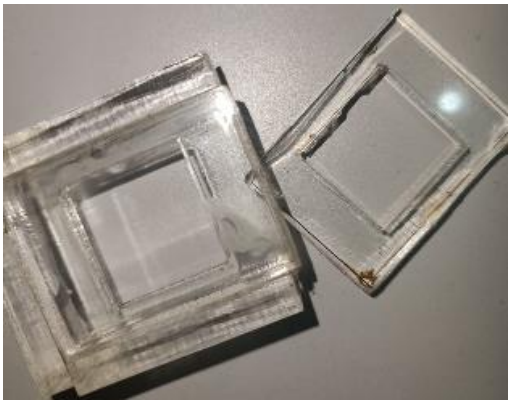

Figure 3.2: Casing of AAB

3.3.2 Air Cathode Fabrication

To optimize the material compositions for air cathode, 5 raw materials have been proposed, which are carbon black, activated carbon, manganese dioxide, propanol and Polytetrafluoroethylene (PTFE). The composition of each material will be determined by the use of the Taguchi method to propose several combinations of each material for the experiment. The design of the air cathode combined both the catalyst layer and gas diffusion layer to reduce the cost and ease the fabrication process.

The size of the air cathode is set as 3 cm*4.5 cm, among this, 2 cm*2 cm will be the coated surface that allows air to flow through. The detailed dimensions of the fabricated aluminium-air batteries will be discussed in

subchapter 3.5. Ni mesh is utilized to be the current collector and also the "skeleton" of the air cathode.

To fabricate the air cathode, the 5 materials were first mixed together in respective mass values. Then, the mixture was attached to the Ni mesh via the rolling process. Lastly, an air cathode was successfully fabricated after the drying process. Figure 3.3 below shows one of the fabricated air cathodes.

Figure 3.3: Fabricated Air Cathode

3.3.3 Electrolyte Preparation

The electrolyte used for the prototype will be the 1 M KOH. To prepare the 1 M KOH solution, the correct amount of KOH pallets was mixed into the corresponding amount of dilute water. For example, 56.11 g of KOH was mixed into 1 litre of distilled water.

3.3.4 Assemble Process

After all components were ready, the fabricated air cathodes were sealed into the casing using the liquid gasket. Lastly, the KOH solution was poured and the 5000 series purchased aluminium alloy anode was inserted into the casing together for operation. Figure 3.4 shows the look of the fabricated aluminium-air battery that is ready for testing.

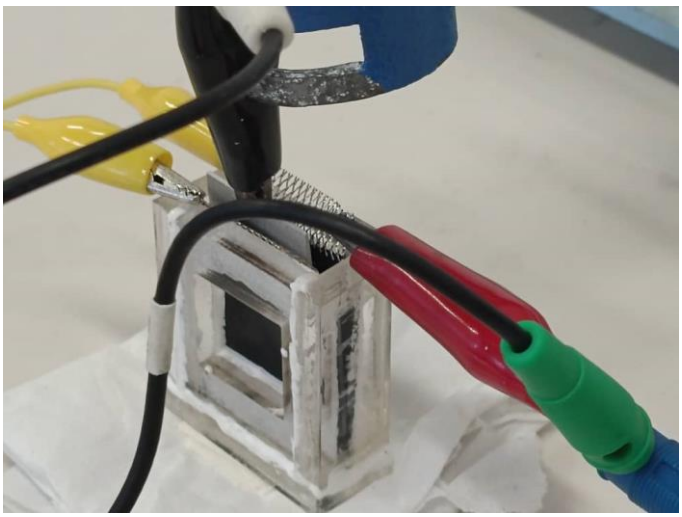

Figure 3.4: Aluminium-air Battery

3.4 Taguchi Method

Taguchi method, which was introduced by Genichi Taguchi is utilized to optimize the process or product (Naqiuddin et al., 2018). In the study, the Taguchi method is utilized to propose several trials of air cathode design in different material compositions for determining the best solution.

3.4.1 Mass Ratio Composition of Batch 1 Samples

The amount of propanol and PTFE are dependent on the total mass of carbon black, activated carbon and manganese dioxide, whereas for batch 1 samples if the total mass of carbon black, activated carbon and manganese dioxide is equal to x, the amount needed for propanol is set to 3x while the PTFE is 2x. Thus, the composition of carbon black, activated carbon and manganese dioxide will be first distributed according to the orthogonal array. After that, the respective amount for propanol and PTFE will be calculated for each trial.

The mass ratio of carbon black, activated carbon and manganese dioxide in different levels is listed in Table 3.1.

Table 3.1: Optimization Parameters of Taguchi Method.

Level	Material Compositions		
	Carbon Black	Activated Carbon	MnO_2
1	8	1	1
2	9	2	2
3	10	3	3

L9 orthogonal array is used to determine 9 trials of air cathode design in different material compositions as shown in Table 3.2.

Table 3.2: L9 Orthogonal Array.

Trials	Factor A	Factor B	Factor C
1	1	1	1
2	1	2	2
3	1	3	3
4	2	1	2
5	2	2	3
6	2	3	1
7	3	1	3
8	3	2	1
9	3	3	2

Then, the respective material compositions of carbon black, activated carbon and MnO_2 are determined following the L9 orthogonal array as listed in Table 3.3.

Table 3.3: Respective Materials Composition according to the L9 Array.

Trials	Carbon Black	Activated Carbon	MnO_2
1	8	1	1
2	8	2	2
3	8	3	3
4	9	1	2
5	9	2	3
6	9	3	1
7	10	1	3
8	10	2	1
9	10	3	2

As the total mass of 2.5 g of the mixture of carbon black, activated carbon and manganese dioxide is more than enough to fabricate one prototype, the total mass of the mixture is then set to be 2.5 g. So, the mass of the propanol and PTFE shall be 7.5 g and 5 g respectively. The respective amount of each material for each trial will then be listed in Table 3.4.

Table 3.4: Mass Needed for Each Material for Each Trial of Batch 1 Samples

Trials	Carbon Black (g)	Activated Carbon (g)	MnO_2 (g)	Propanol (g)	PTFE (g)
1	2.00	0.25	0.25	7.5	5
2	1.67	0.42	0.42		
3	1.43	0.54	0.54		
4	1.88	0.21	0.42		
5	1.61	0.36	0.54		
6	1.73	0.58	0.19		
7	1.79	0.18	0.54		
8	1.92	0.38	0.19		
9	1.67	0.50	0.33		
SUM	15.68	3.41	3.41	67.5	45

3.4.2 Mass Ratio Composition of Batch 2 Samples

For batch 2 samples, the mass ratio composition of Carbon Black, Activated Carbon and Manganese (IV) Oxide is set to be the same as the optimized result obtained from batch 1, whereas the detailed mass ratio of these three materials will be determined in the subsequent experiment session. For the current stage, the mass ratio of Propanol and PTFE is only depending on the total mass value of the mixture of Carbon Black, Activated Carbon and Manganese (IV) Oxide. Therefore, the total mass of these three material mixtures is simply set to x = 2.5 g once again. Then, the mass ratio of propanol and PTFE in different levels are shown in Table 3.5.

Table 3.5: Mass Ratio of Propanol and PTFE in Different Levels

Total mass of Carbon Black, Activated Carbon and MnO_2	Level	Mass ratio of Propanol	Mass ratio of PTFE
x = 2.5 g	1	1x = 2.5 g	2x = 5 g
	2	2x = 5 g	3x = 7.5 g
	3	3x = 7.5 g	4x = 10 g

Similar to the batch 1 samples, the use of the Taguchi Method proposed several trials with different combinations of levels from each factor to test the result. The mass needed for each material of batch 2 samples is shown in Table 3.6.

Table 3.6: Mass Needed for Each Material for Each Trial of Batch 2 Samples

Trials	Total mass of the mixture of Carbon Black, Activated Carbon and MnO_2 (g)	Propanol (g)	PTFE (g)
10	2.5	2.5	5.0
11		2.5	7.5
12		2.5	10.0
13		5.0	5.0
14		5.0	7.5
15		5.0	10.0
16		7.5	5.0
17		7.5	7.5
18		7.5	10.0
SUM	22.5	45	67.5

3.5 Prototype Design

The dimension for the aluminium air battery (AAB) casing, aluminium anode and air cathode is shown below. All dimensions are in mm units. In this design, there will be two air cathodes sealed in front and back of the AAB casing, the aluminium anode will insert inside the casing to immerse in the KOH solution.

Figures 3.5 and 3.6 below show the overall prototype design and its exploded view.

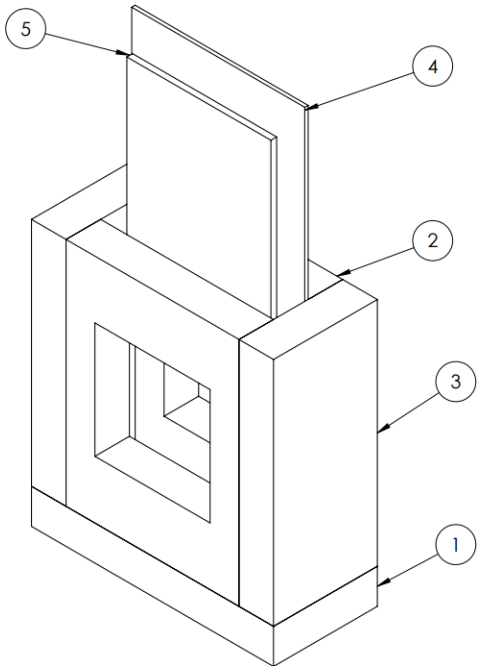

ITEM NO.	PART NUMBER	QTY.
1	AAB Casing BOTTOM	1
2	AAB Casing FRONT	2
3	AAB Casing SIDE	2
4	Air Cathode	2
5	Al Anode	1

Figure 3.5: Exploded View of AAB

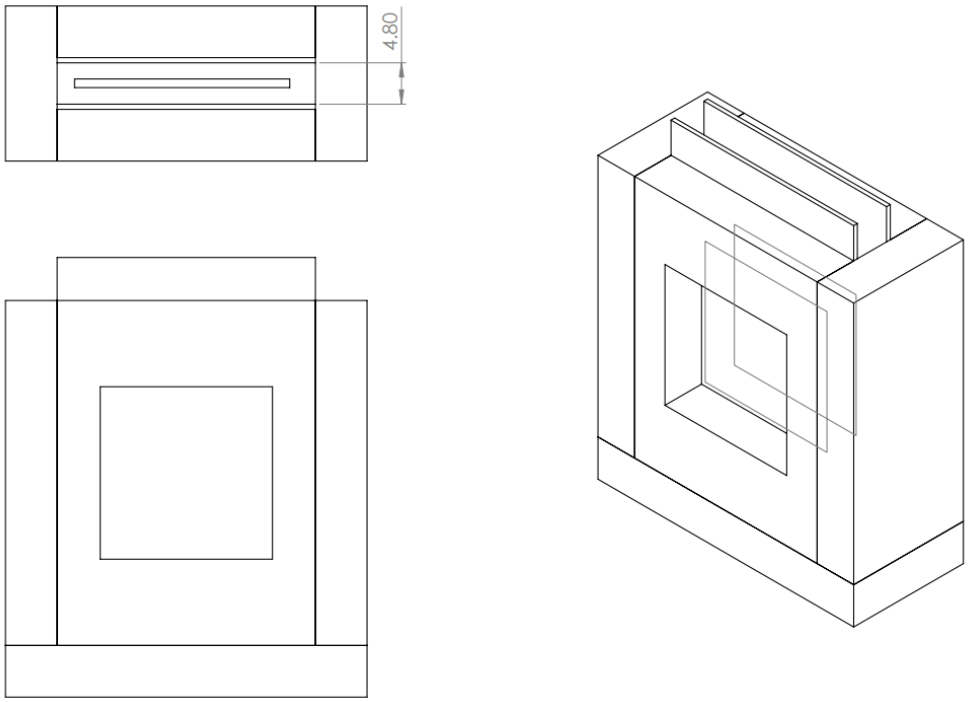

Figure 3.6: Overview of AAB in mm

Figure 3.7 shows the dimension of aluminium anode purchased which is made from 5000 series aluminium alloy. The thickness of the aluminium anode shall be 1 mm.

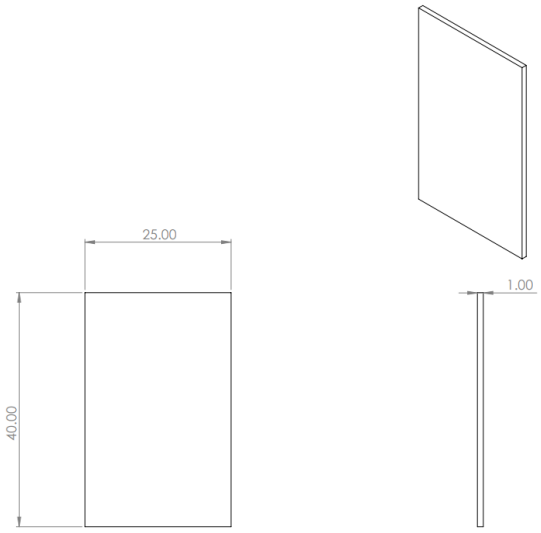

Figure 3.7: Dimension of Aluminium Anode in mm

Figure 3.8 shows the dimensions of the fabricated air cathode. The dimension of the coated surface shall be 20 mm x 20 mm.

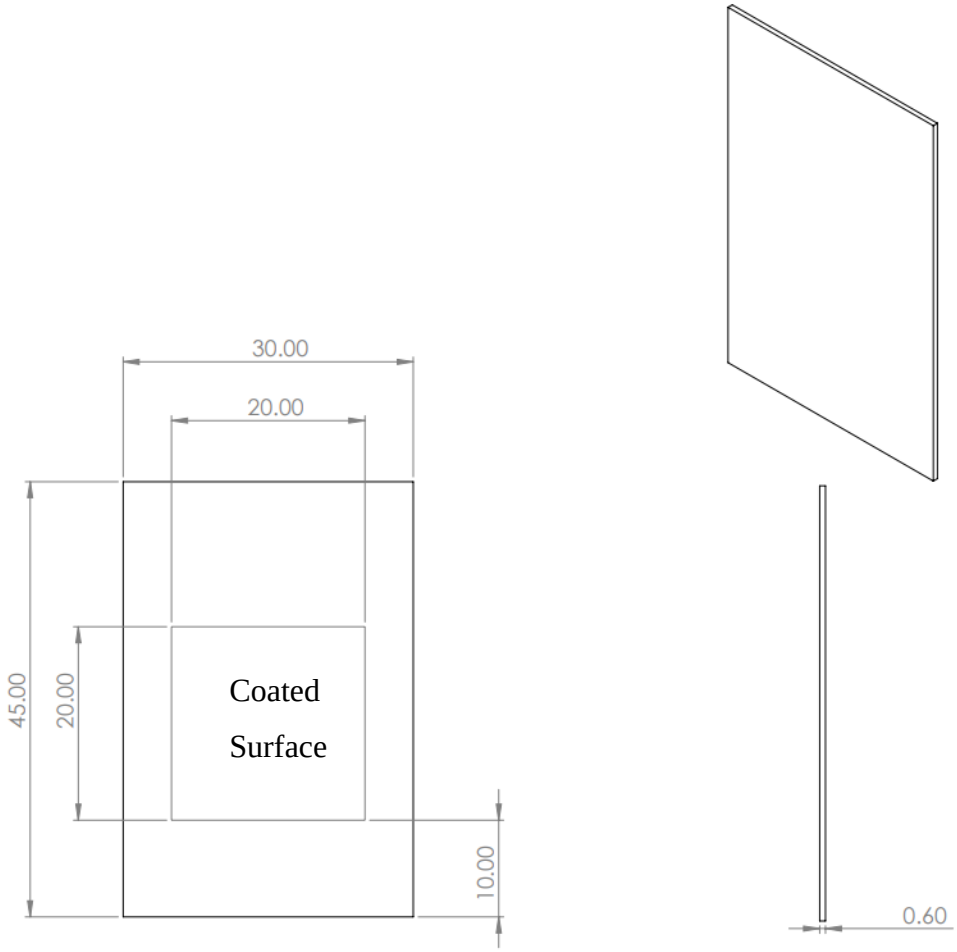

Figure 3.8: Dimension of Air Cathode in mm

Figures 3.9, 3.10 and 3.11 show the bottom view, front and back view, and side view of the fabricated AAB casing which is made from the acrylic board. These acrylic boards will then be stuck together using chloroform after laser cutting.

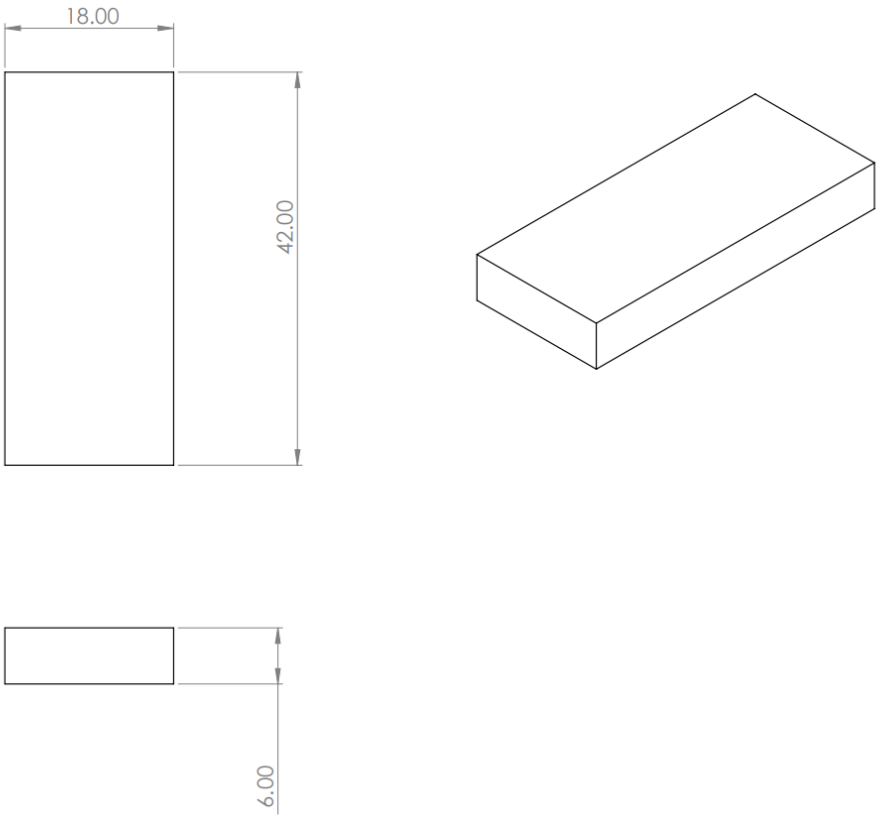

Figure 3.9: Dimension of AAB Casing (Bottom) in mm

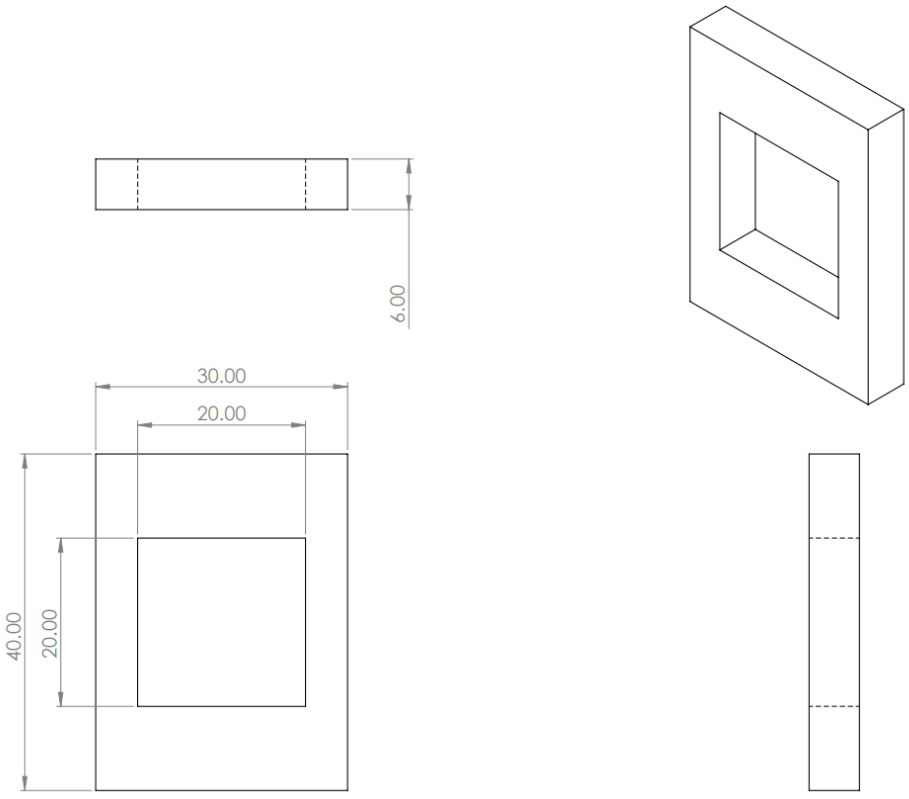

Figure 3.10: Dimension of AAB Casing (Front & Back) in mm

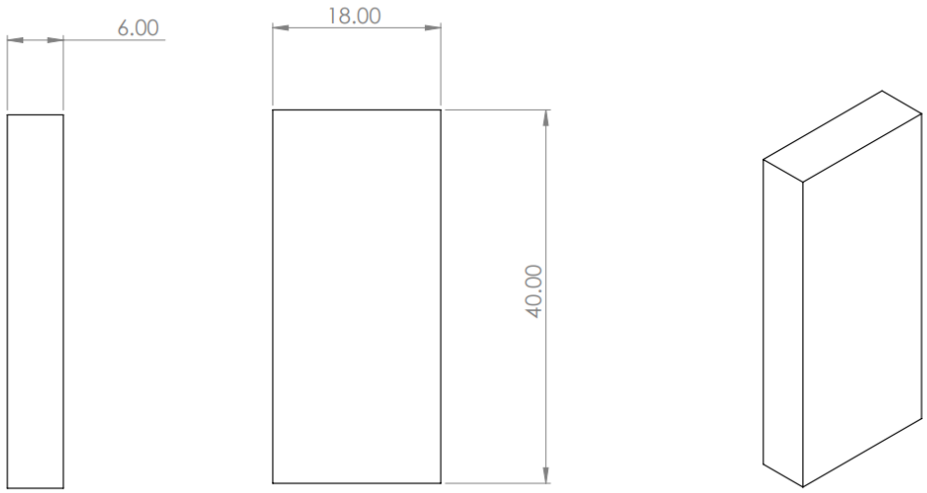

Figure 3.11: Dimension of AAB Casing (Side) in mm

3.6 Purchase List

The purchase list needed for the fabrication of 9 prototypes is listed in Table 3.7.

Table 3.7: Purchase List of Prototypes.

No	Components	Item	Quantity	Price (RM)
1.	Alkaline Electrolyte	1L KOH	2	64
2.	Air Cathode	500 g Carbon Black	1	26.05
3.		50 g Activated Carbon	1	12.90
4.		500 g MnO2	1	34.90
5.		500 ml Propanol	1	13.80
6.		100 g PTFE	1	78.43
7.		Ni Mesh	1	37.12
8.	Anode	5000 series Al	15	68.17
9.	Casing	A2 Acrylic board	1	28.90

10.		50 ml Chloroform	1	14.40
11.		100 Pcs Screw Needle Nozzle	1	23.90

3.7 Experiment Study

Once the prototypes are ready, experiments will be carried out to study the behaviour and evaluate the performance of the battery. A discharge test and linear sweep voltammetry (LSV) test will be carried out. A discharge test is utilized to test the battery capacity and discharge behaviour. By discharging a battery, the actual capacity of the battery can be determined to compare with its rated value. This can be done by applying a load in amperes or watts towards the system for discharging in a specified time range. In addition, if further discharging the battery, the end of discharge voltage of the cell can be obtained also (Tressler, 2022).

LSV measured the produced electric current of the cell by applying a controlled voltage to study its electrochemical behaviour. LSV is conducted by sweeping the applied voltage from the low limit to the high limit, when changing the sweeping time, the scan rate can be altered. The scan rate of the LSV can be simply obtained from the slope of the Voltage-Time Chart. From LSV, several electrochemical behaviours of the battery can be determined. First, depending on the shape of the obtained voltammogram, the electron transfer rate can be identified. Second, by relating the equilibrium electrochemistry to the Nernst equation as listed in Eq 3.1, the relationship between the applied voltage and concentration of reactants can be obtained (University of Cambridge, 2013).

$$E = E° + \frac{RT}{zF} \ln Q \quad (3.1)$$

Where

E = applied voltage

E° = standard potential

R = universal gas constant

z = ion charge

F = Faraday constant

Q = reaction quotient

When the applied voltage is sweeping from the lower limit to the upper limit, to satisfy the Nernst equation, the reaction quotient Q, or the concentration of the reactants needs to be altered. As the produced current is proportional to the flux of reactants when the flux of reactant is not sufficient to catch up with the value needed for the Nernst equation, the produced current will then begin to drop after the peak point.

3.8 Grey Relational Analysis

After the experiment, the obtained results will be analyzed through grey relational analysis to determine the optimum material compositions for air cathode among 18 prototypes for both batch 1 and batch 2 samples. The experiment results will then follow the steps and the formula below for calculation (Naqiuddin et al., 2018).

Step 1: Normalizing the data

Based on the normalization criteria of the data, the formula for the data which is larger the best or smaller the best will be used as listed in Eqs 3.2 and 3.3:

The larger the better: $$x_i^*(k) = \frac{x_i^0(k) - \min x_i^0(k)}{\max x_i^0(k) - \min x_i^0(k)} \quad (3.2)$$

The smaller the better: $$x_i^*(k) = \frac{\max x_i^0(k) - x_i^0(k)}{\max x_i^0(k) - \min x_i^0(k)} \quad (3.3)$$

Where

$x_i^0(k)$ = sequence before normalization processing

$x_i^*(k)$ = processed sequence after normalization

$\max x_i^0(k)$ = the largest value among the values of $x_i^0(k)$

$\min x_i^0(k)$ = smallest value among the values of $x_i^0(k)$

Step 2: Determination of deviation sequence

The deviation sequence can be obtained from Eq 3.4.

$$\Delta_{0i}(k) = \|x_0^*(k) - x_i^*(k)\| \tag{3.4}$$

Where

$x_0^*(k) = 1$

Step 3: Grey Relational Coefficient (GRC)

Then, the Grey Relational Coefficient can be obtained via Eq 3.5.

$$\xi_i(k) = \frac{\Delta_{min} + \xi\Delta_{max}}{\Delta_{0i}(k) + \xi\Delta_{max}} \tag{3.5}$$

Where

$\Delta_{min} = \min_{\forall j \epsilon i} \min_{\forall k} \|x_0(k) - x_j(k)\| =$ smallest value of $\Delta_{0i}, 0$

$\Delta_{max} = \max_{\forall j \epsilon i} \max_{\forall k} \|x_0(k) - x_j(k)\| =$ largest value of $\Delta_{0i}, 1$

ξ = distinguishing or identification coefficient$= [0,1]$, generally $\xi = 0.5$.

Step 4: Grey Relational Grade (GRG) and Ranking

Eq 3.6 is utilized to determine the Grey Relational Grade of each trial.

$$\gamma_i = \frac{1}{\sum_{k=1}^{n} w_k} \sum_{k=1}^{n} w_k \xi_i(k) \tag{3.6}$$

Where

γ_i = GRG of the i^{th} trial

w_k = normalized weight value of performance characteristic of k order

$\sum_{k=1}^{n} w_k$ = sum of the normalized weight value of performances = 1

Lastly, from the calculated GRG values, the ranking of each trial can be determined where the largest value of GRG will be placed in the highest rank.

3.9 Summary

This project will be across a three-trimester duration. For session 202305, it is estimated to take 14 weeks to formulate the problem, plan the project and conduct the necessary studies. For session 202310 and 202401, these two trimesters are allocated to conduct the AAB fabrication, experiment and result analysis. For the planning of the experiment, to optimize the material compositions of the air cathode, the experiment will be divided into 2 batches. The first batch of samples is aimed to optimize the mass ratio of the powder mixture, which is carbon black, activated carbon and manganese (iv) oxide. The second batch of samples is aimed to optimize the mass ratio of propanol and PTFE.

CHAPTER 4

RESULTS AND DISCUSSION

4.1 Introduction

The experiment is divided into two batches to obtain the best performance result. The batch 1 samples, consisting of 9 samples, which are sample 1 to sample 9, were fabricated and tested in order to optimize the mass ratio of Carbon Black, Activated Carbon and Manganese (IV) Oxide. Then, the optimized result of batch 1 samples will carry forward to batch 2 for the optimization of the mass ratio of PTFE and Propanol. Similarly, batch 2 will consist of 9 samples (sample 10 to sample 18) also since the L9 orthogonal array is selected once again.

4.2 Batch 1 Samples

From the discharge test and LSV test, the graphs of each sample obtained can extract several parameters for analysis. From the discharge test, the plateau voltage and discharge time parameters were captured. The plateau voltage indicates the longest voltage value of the sample to maintain throughout the experiment. From the discharge graph obtained, to determine the plateau voltage, histogram data analysis is utilized for higher accuracy. For example, from the discharge graph of sample 4 shown in Figure 4.1, to determine the plateau voltage, all the voltage values are processed via histogram analysis and the lower limit of the range that has the highest frequency shall be the plateau voltage of sample 4. As shown in Table 4.1, since the range of 1.2-1.29 V has the highest frequency, which indicates that 1.2-1.29 V is the longest voltage range that can be maintained by sample 4 through the discharge test, 1.2 V is determined as the plateau voltage value.

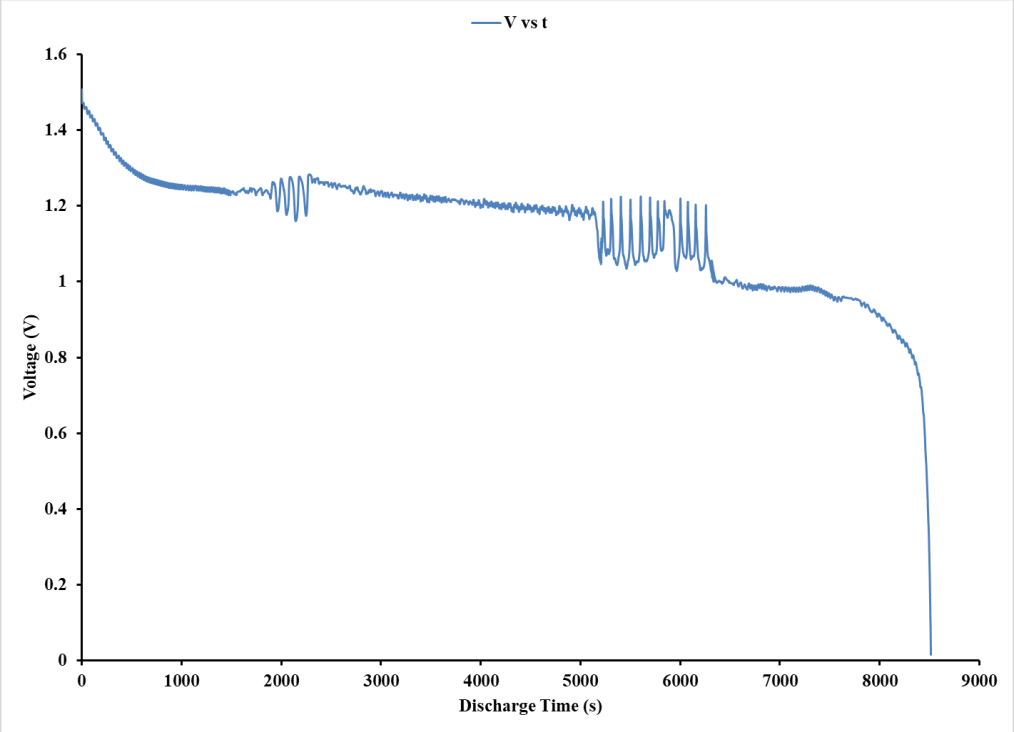

Figure 4.1: Discharge Graph of Sample 4

Table 4.1: Histogram for Sample 4 Plateau Voltage Determination

Range	Bin	Frequency
0-0.09	0.09	4
0.1-0.19	0.19	6
0.2-0.29	0.29	8
0.3-0.39	0.39	11
0.4-0.49	0.49	14
0.5-0.59	0.59	18
0.6-0.69	0.69	26
0.7-0.79	0.79	77
0.8-0.89	0.89	282
0.9-0.99	0.99	1393
1.0-1.09	1.09	1050
1.1-1.19	1.19	934
1.2-1.29	1.29	4160
1.3-1.39	1.39	320
1.4-1.49	1.49	212
<1.5	More	2

The discharge time value is a needed parameter to calculate the specific capacity of the sample for further analysis. It can be determined by just simply looking through the x-axis of the discharge graph.

For the LSV test, using the result of sample 4 also, the peak power can be determined from the maximum value of the P vs I curve as shown in Figure 4.2. While the I_{shoot} represents the shutdown current of the LSV test.

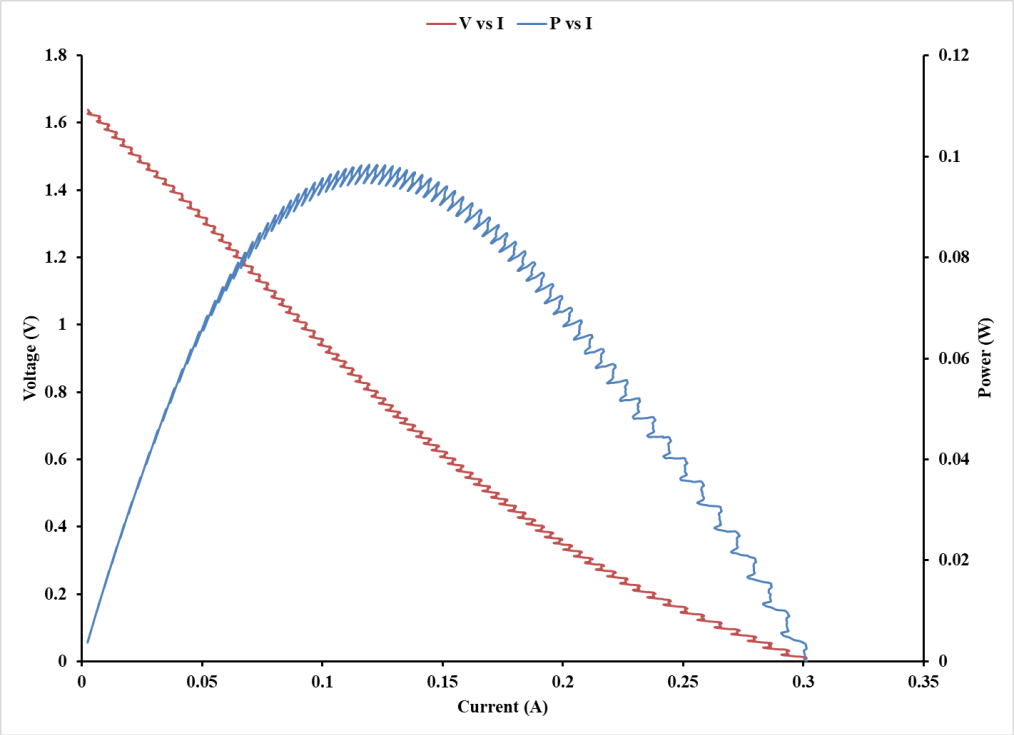

Figure 4.2: LSV Graph of Sample 4

Using these data extraction concepts, from the graphs obtained from all batch 1 sample testings, the results of the batch 1 samples from discharge and LSV tests are extracted and recorded as shown in Table 4.2. As a reference, the graphs obtained from all batch 1 samples are shown in appendix A (GraphA-1 to GraphA-16).

Table 4.2: Parameters Obtained from Batch 1 Samples

Sample	Discharge		LSV	
	Plateau Voltage (V)	Discharge Time (s)	Peak Power (W)	Shutdown Current (A)
1	0.7	8920	0.066	0.2184
2	0.4	9997	0.053	0.1826
3	0.8	6106	0.116	0.2817
4	1.2	8517	0.098	0.3013
5	0.5	7574	0.043	0.1333
6	0.7	8600	0.026	0.0683
7	0.9	8413	0.049	0.1660
8	1.1	7823	0.070	0.2613
9	0.6	8008	0.018	0.0896

The specific capacity of the sample can be calculated using the mass difference value of the aluminium anode before and after the experiment and formula 4.1 as shown below. The discharge current is set as 50 mA.

$$\text{Specific Capacity} = \frac{\text{Discharge Current} \times \text{Discharge Time}}{\text{Mass Difference of Aluminium Anode}} \qquad (4.1)$$

Table 4.3 below shows the mass difference of aluminium anode and specific capacity calculated for all batch 1 samples.

Table 4.3: Specific Capacity of Batch 1 Samples

Samples	Initial Mass (g)	Final Mass (g)	Mass Difference (g)	Specific Capacity (Ah/g)
1	2.8400	2.7981	0.0419	2.957
2	2.9000	2.8350	0.0650	2.136
3	2.9100	2.8800	0.0300	2.827
4	2.8477	2.8000	0.0477	2.48
5	2.8700	2.8400	0.0300	3.507
6	2.8200	2.7800	0.0400	2.986
7	2.9300	2.8800	0.0500	2.337
8	2.8220	2.7760	0.0460	2.362
9	2.8900	2.8500	0.0400	2.781

Since the mass ratio of each sample has too many variables and factors to the result, it is quite hard to simply conclude the outcomes. Thus, the obtained results are further analyzed and ranked by first introducing the use of Grey Relational Analysis. The use of Grey Relational Analysis can easily identify the best performance sample by ranking all the samples and considering all four testing parameters (Plateau Voltage, Specific Capacity, Peak Power and Shutdown Current) obtained at the same time. In the simplest words, the top-rank sample will be the final selection for the optimized result in batch 1. Using the formula stated in Chapter 3, the Grey Relational analysis is conducted step by step as shown below.

Table 4.4 shows the GRC for plateau voltage of batch 1 samples.

Table 4.4: GRC for Plateau Voltage of Batch 1 Samples

Trials, i	Plateau Voltage (V)	$x_i^*(1)$	Deviation Sequence, $\Delta_{0i}(1)$	GRC, $\xi_i(1)$
1	0.7	0.3750	0.6250	0.4444
2	0.4	0.0000	1.0000	0.3333
3	0.8	0.5000	0.5000	0.5000
4	1.2	1.0000	0.0000	1.0000
5	0.5	0.1250	0.8750	0.3636
6	0.7	0.3750	0.6250	0.4444
7	0.9	0.6250	0.3750	0.5714
8	1.1	0.8750	0.1250	0.8000
9	0.6	0.2500	0.7500	0.4000

Similarly, Table 4.5, Table 4.6 and Table 4.7 show the GRC values for specific capacity, peak power and shutdown current of batch 1 samples respectively.

Table 4.5: GRC for Specific Capacity of Batch 1 Samples

Trials, i	Specific Capacity (Ah/g)	$x_i^*(2)$	Deviation Sequence, $\Delta_{0i}(2)$	GRC, $\xi_i(2)$
1	2.9568	0.5989	0.4011	0.5549
2	2.1361	0.0000	1.0000	0.3333
3	2.8269	0.5041	0.4959	0.5020
4	2.4799	0.2509	0.7491	0.4003
5	3.5065	1.0000	0.0000	1.0000
6	2.9861	0.6203	0.3797	0.5684
7	2.3369	0.1466	0.8534	0.3694
8	2.3620	0.1649	0.8351	0.3745
9	2.7806	0.4703	0.5297	0.4856

Table 4.6: GRC for Peak Power of Batch 1 Samples

Trials, i	Peak Power (W)	$x_i^*(3)$	Deviation Sequence, $\Delta_{0i}(3)$	GRC, $\xi_i(3)$
1	0.0660	0.4898	0.5102	0.4949
2	0.0530	0.3571	0.6429	0.4375
3	0.1160	1.0000	0.0000	1.0000
4	0.0980	0.8163	0.1837	0.7313
5	0.0430	0.2551	0.7449	0.4016
6	0.0260	0.0816	0.9184	0.3525
7	0.0490	0.3163	0.6837	0.4224
8	0.0700	0.5306	0.4694	0.5158
9	0.0180	0.0000	1.0000	0.3333

Table 4.7: GRC for Shutdown Current of Batch 1 Samples

Trials, i	Shutdown Current (A)	$x_i^*(4)$	Deviation Sequence, $\Delta_{0i}(4)$	GRC, $\xi_i(4)$
1	0.2184	0.6442	0.3558	0.5843
2	0.1826	0.4906	0.5094	0.4953
3	0.2817	0.9159	0.0841	0.8560
4	0.3013	1.0000	0.0000	1.0000
5	0.1333	0.2790	0.7210	0.4095
6	0.0683	0.0000	1.0000	0.3333
7	0.1660	0.4193	0.5807	0.4627
8	0.2613	0.8283	0.1717	0.7444
9	0.0896	0.0914	0.9086	0.3550

Lastly, using the obtained GRC values and setting all performance parameters are equally important by having same value of normalized weight value, w = 0.25, The GRG and Ranking of batch 1 samples can be obtained as shown in Table 4.8.

Table 4.8: Performance Ranking of Batch 1 Samples

Trials, i	GRC, $\xi_i(1)$	GRC, $\xi_i(2)$	GRC, $\xi_i(3)$	GRC, $\xi_i(4)$	GRG, γ_i	Rank
1	0.4444	0.5549	0.4949	0.5843	0.5196	5
2	0.3333	0.3333	0.4375	0.4953	0.3999	8
3	0.5000	0.5020	1.0000	0.8560	0.7145	2
4	1.0000	0.4003	0.7313	1.0000	0.7829	1
5	0.3636	1.0000	0.4016	0.4095	0.5437	4
6	0.4444	0.5684	0.3525	0.3333	0.4247	7
7	0.5714	0.3694	0.4224	0.4627	0.4565	6
8	0.8000	0.3745	0.5158	0.7444	0.6087	3
9	0.4000	0.4856	0.3333	0.3550	0.3935	9

To further analyze the effect of each material towards the performance, the signal-to-noise ratio (SNR) can be calculated. Taguchi SNR is widely used to identify the optimal parameter settings of a single response (Qazi et al., 2021). In this experiment, since higher plateau voltage, specific capacity, peak power and shutdown current are aimed, thus the quality characteristic for the target design will be “larger the better”. Thus, according to this characteristic, the SNR can be calculated by the formula 4.2:

$$\text{SNR} = -10\log_{10}\left(\frac{1}{n}\sum_{i=1}^{n}\frac{1}{Y_i^2}\right) \qquad (4.2)$$

Then, by calculating the difference of SNR of each sample among all levels, the material or the factor that has the significant effect towards the results can be determined as stated in Table 4.9, Table 4.10, Table 4.11 and Table 4.12. From Table 4.9 and Table 4.12, the values of the SNR difference of activated carbon for plateau voltage and shutdown current are much larger than the other two factors. This indicates that the Activated Carbon is having the significant effect on the battery to obtain better performance for plateau voltage and shutdown current. This can be said because by just changing the mass ratio of Activated Carbon from one level to another level, the plateau voltage and shutdown current results obtained will have so much difference,

while by changing the levels of the other two factors, the results obtained will no having so much difference, which means the effect of Activated Carbon is much more significant compares to other two materials (Carbon Black and Manganese (IV) Oxide).

Similarly, as shown in Table 4.10 and Table 4.11, for specific capacity and peak power, the carbon black is more important or has a more significant effect. However, for peak power, the difference of SNR value of Activated Carbon (5.11) is actually very close to Carbon Black (5.45). Thus, in general, it can be said that the mass ratio of activated carbon is much more important.

Table 4.9: SNR for Plateau Voltage

Level	Carbon Black	Activated Carbon	MnO_2
1	-4.3317	-0.8099	-1.7894
2	-2.5117	-4.3838	-3.6041
3	-1.5081	-3.1577	-2.9580
Delta	2.8236	3.5740	1.8146
Rank	2	1	3

Table 4.10: SNR for Specific Capacity

Level	Carbon Black	Activated Carbon	MnO_2
1	8.345	8.226	8.795
2	9.429	8.319	7.788
3	7.907	9.137	9.099
Delta	1.522	0.911	1.311
Rank	1	3	2

Table 4.11: SNR for Peak Power

Level	Carbon Black	Activated Carbon	MnO_2
1	-22.61	-23.33	-26.14
2	-26.4	-25.31	-26.86
3	-28.06	-28.44	-24.08
Delta	5.45	5.11	2.78
Rank	1	2	3

Table 4.12: SNR for Shutdown Current

Level	Carbon Black	Activated Carbon	MnO_2
1	-13	-13.08	-16.06
2	-17.08	-14.64	-15.38
3	-16.07	-18.42	-14.7
Delta	4.08	5.35	1.36
Rank	2	1	3

The SNR value also indicates the quality of the performance, which is the level of a factor that has a higher SNR value can provide better performance than the other two levels (Kotcioglu, Cansiz and Nasiri Khalaji, 2013). For example, for the plateau voltage output and shutdown current, the level 1 Activated Carbon samples can provide better performance than the samples which had levels 2 and 3 of the mass ratio of activated carbon. Similarly, level 2 of carbon black can provide higher specific capacity while level 1 of carbon black can provide higher peak power.

Since activated carbon and carbon black are much more important by having larger SNR difference values to indicate the more significant effect towards the performance, the investigation of the activated carbon and carbon black is further carried out.

According to the SNR obtained above, the outcomes proposed that the optimized sample to have better performance shall consist of a higher mass ratio of Carbon Black (8 or 9 mass ratio) and a lower mass ratio of activated carbon, which is a mass ratio of 1. To further verify the finding, the samples that switched the mass ratio of activated carbon and carbon black of sample 1 and sample 4, which were labelled as CS 1 and CS 2 were fabricated and tested. The mass ratio of each material for CS 1 and CS 2 compared with sample 1 and sample 4 is shown in Table 4.13.

Table 4.13: Mass Ratio of Sample 1, CS 1, Sample 4 and CS 2

Sample	Carbon Black (g)	Activated Carbon (g)	MnO_2 (g)	Propanol (g)	PTFE (g)
1	2.00	0.25	0.25	7.5	5
CS 1	0.25	2.00	0.25		
4	1.88	0.21	0.42		
CS 2	0.21	1.88	0.42		

Then, from the graphs output of CS 1 and CS 2 shown in appendix A (GraphA-17 to GraphA-20), the parameters needed for analysis were extracted. The recorded data is then compared with sample 1 and sample 4 to verify the concept as stated in Table 4.14. The results show that sample CS 1 and sample CS 2 both have poor performance compared with sample 1 and sample 4 respectively. Thus, the assumption made based on the finding is further proven and verified. The mass ratio of activated carbon shall be lower and consequently the mass ratio of carbon black shall be higher.

Table 4.14: Comparison Table of Sample 1, Sample 4, CS 1 and CS 2 Outputs

Sample	Discharge		LSV	
	Plateau Voltage (V)	Specific Capacity (Ah/g)	Peak Power (W)	Shutdown Current (A)
1	0.7	2.957	0.066	0.2184
CS 1	0.3	2.340	0.041	0.2458
4	1.2	2.480	0.098	0.3013
CS 2	0.1	2.729	0.024	0.1338

Lastly, from the output of Grey Relational Analysis, sample 4 will be the best sample and optimized result of batch 1 sample. Thus, the mass ratio of Carbon Black, Activated Carbon and Manganese (IV) Oxide of sample 4 will be carried forward to batch 2 for further analysis of the mass ratio of Propanol and PTFE.

4.3 Batch 2 Sample

Similar to the procedures of batch 1 samples, from the graphs obtained from the testing of batch 2 samples (GraphB-1 to GraphB-18), parameters needed for analysis are extracted and recorded in Table 4.15.

Table 4.15: Parameters Obtained from Batch 2 Samples

Sample	Discharge		LSV	
	Plateau Voltage (V)	Discharge Time (s)	Peak Power (W)	Shutdown Current (A)
10	0.6	8308	0.046	0.2101
11	0.3	7566	0.032	0.1795
12	0.1	5900	0.021	0.1097
13	0.9	7565	0.060	0.2425
14	0.6	6994	0.044	0.2050
15	0.3	6930	0.029	0.1617
16	1.1	8549	0.098	0.2673
17	0.6	7772	0.045	0.1668
18	0.4	6072	0.038	0.1726

Then, using formula 4.1, the specific capacity of batch 2 samples is calculated and stated in Table 4.16. The discharge current throughout the discharge test is again 50 mA.

Table 4.16: Specific Capacity of Batch 2 Samples

Samples	Initial Mass (g)	Final Mass (g)	Mass Difference (g)	Specific Capacity (Ah/g)
10	2.7700	2.7200	0.0500	2.308
11	2.7415	2.6994	0.0421	2.496
12	2.8212	2.7904	0.0308	2.661
13	2.8508	2.8079	0.0429	2.449
14	2.7453	2.7062	0.0391	2.484
15	2.6418	2.6027	0.0391	2.462
16	2.7028	2.6553	0.0475	2.500
17	2.6825	2.6426	0.0399	2.705
18	2.7563	2.7243	0.0320	2.635

Gathering the data of plateau voltage, specific capacity, peak power and shutdown current of batch 2 samples, grey relational analysis is then utilized again to rank the batch 2 sample in order to obtain the optimized material compositions of the air cathode.

Similar with batch 1 samples, Table 4.17, Table 4.18, Table 4.19 and Table 4.20 show the GRC values for plateau voltage, specific capacity, peak power and shutdown current of batch 2 samples respectively. Table 4.21 shows the performance ranking of batch 2 samples. From the Grey Relational Analysis results, sample 16 shall be the best sample among batch 2 samples.

Table 4.17: GRC for Plateau Voltage of Batch 2 Samples

Trials, i	Plateau Voltage (V)	$x_i^*(1)$	Deviation Sequence, $\Delta_{0i}(1)$	GRC, $\xi_i(1)$
10	0.6	0.5000	0.5000	0.5000
11	0.3	0.2000	0.8000	0.3846
12	0.1	0.0000	1.0000	0.3333
13	0.9	0.8000	0.2000	0.7143
14	0.6	0.5000	0.5000	0.5000
15	0.3	0.2000	0.8000	0.3846
16	1.1	1.0000	0.0000	1.0000
17	0.6	0.5000	0.5000	0.5000
18	0.4	0.3000	0.7000	0.4167

Table 4.18: GRC for Specific Capacity of Batch 2 Samples

Trials, i	Specific Capacity (Ah/g)	$x_i^*(2)$	Deviation Sequence, $\Delta_{0i}(2)$	GRC, $\xi_i(2)$
10	2.3078	0.0000	1.0000	0.3333
11	2.4960	0.4735	0.5265	0.4871
12	2.6605	0.8872	0.1128	0.8160
13	2.4492	0.3556	0.6444	0.4369
14	2.4844	0.4442	0.5558	0.4736
15	2.4616	0.3870	0.6130	0.4492
16	2.4997	0.4827	0.5173	0.4915
17	2.7054	1.0000	0.0000	1.0000
18	2.6354	0.8240	0.1760	0.7397

Table 4.19: GRC for Peak Power of Batch 2 Samples

Trials, i	Peak Power (W)	$x_i^*(3)$	Deviation Sequence, $\Delta_{0i}(3)$	GRC, $\xi_i(3)$
10	0.0460	0.3247	0.6753	0.4254
11	0.0320	0.1429	0.8571	0.3684
12	0.0210	0.0000	1.0000	0.3333
13	0.0600	0.5065	0.4935	0.5033
14	0.0440	0.2987	0.7013	0.4162
15	0.0290	0.1039	0.8961	0.3581
16	0.0980	1.0000	0.0000	1.0000
17	0.0450	0.3117	0.6883	0.4208
18	0.0380	0.2208	0.7792	0.3909

Table 4.20: GRC for Shutdown Current of Batch 2 Samples

Trials, i	Shutdown Current (A)	$x_i^*(4)$	Deviation Sequence, $\Delta_{0i}(4)$	GRC, $\xi_i(4)$
10	0.2101	0.6371	0.3629	0.5794
11	0.1795	0.4429	0.5571	0.4730
12	0.1097	0.0000	1.0000	0.3333
13	0.2425	0.8426	0.1574	0.7606
14	0.2050	0.6047	0.3953	0.5585
15	0.1617	0.3299	0.6701	0.4273
16	0.2673	1.0000	0.0000	1.0000
17	0.1668	0.3623	0.6377	0.4395
18	0.1726	0.3991	0.6009	0.4542

Table 4.21: Performance Ranking of Batch 2 Samples

Trials, i	GRC, $\xi_i(1)$	GRC, $\xi_i(2)$	GRC, $\xi_i(3)$	GRC, $\xi_i(4)$	GRG, γ_i	Rank
10	0.5000	0.3333	0.4254	0.5794	0.4595	6
11	0.3846	0.4871	0.3684	0.4730	0.4283	8
12	0.3333	0.8160	0.3333	0.3333	0.4540	7
13	0.7143	0.4369	0.5033	0.7606	0.6038	2
14	0.5000	0.4736	0.4162	0.5585	0.4871	5
15	0.3846	0.4492	0.3581	0.4273	0.4048	9
16	1.0000	0.4915	1.0000	1.0000	0.8729	1
17	0.5000	1.0000	0.4208	0.4395	0.5901	3
18	0.4167	0.7397	0.3909	0.4542	0.5004	4

The SNR values regarding all four parameters' performance are calculated as shown in Table 4.22, Table 4.23, Table 4.24 and Table 4.25. From the SNR values, all four parameter outcomes proposed that PTFE is more crucial than propanol in affecting performance by providing a higher SNR difference value. In addition, except for the SNR values for the specific capacity of different levels of PTFE that are relatively closer to each other, the other three outputs all recommended the level 1 PTFE for better performance with the support of higher SNR values. Thus, it can be said that the PTFE mass ratio shall be lower (level 1 mass ratio) in the prototype.

Table 4.22: SNR for Plateau Voltage

Level	Propanol	PTFE
1	-11.632	-1.508
2	-5.27	-6.444
3	-3.856	-12.805
Delta	7.776	11.297
Rank	2	1

Table 4.23: SNR for Specific Capacity

Level	Propanol	PTFE
1	7.904	7.668
2	7.836	8.164
3	8.339	8.247
Delta	0.503	0.58
Rank	2	1

Table 4.24: SNR for Peak Power

Level	Propanol	PTFE
1	-30.07	-23.79
2	-27.44	-27.99
3	-25.17	-30.9
Delta	4.89	7.12
Rank	2	1

Table 4.25: SNR for Shutdown Current

Level	Propanol	PTFE
1	-15.89	-12.44
2	-13.97	-14.75
3	-14.09	-16.76
Delta	1.92	4.32
Rank	2	1

From the results obtained, it can be said that the presence of PTFE will generally inhibit or lower the performance of aluminium-air batteries. This can be supported by looking through Figure 4.3 and Figure 4.4, the values of plateau voltage and peak power follows the trends where when increasing the mass ratio of PTFE, the performance of Plateau Voltage and Peak Power will become poorer. Oppositely, when increasing the mass ratio of propanol, the performance of Plateau Voltage and Peak Power will become better.

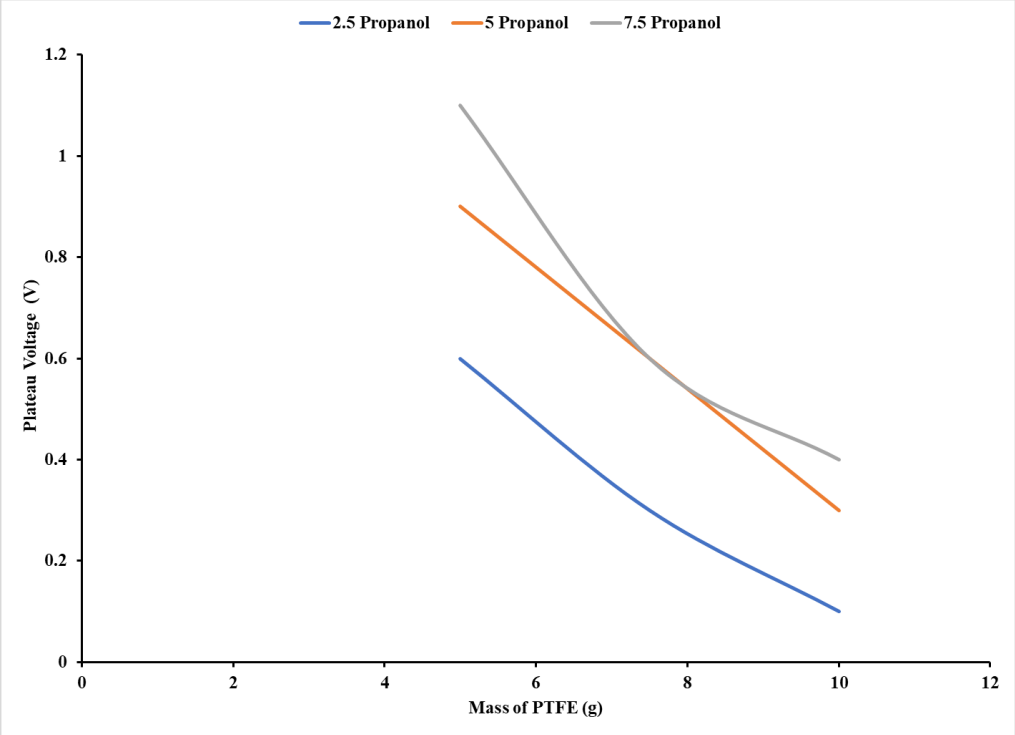

Figure 4.3: Plateau Voltage Value for Various Mass of PTFE and Propanol

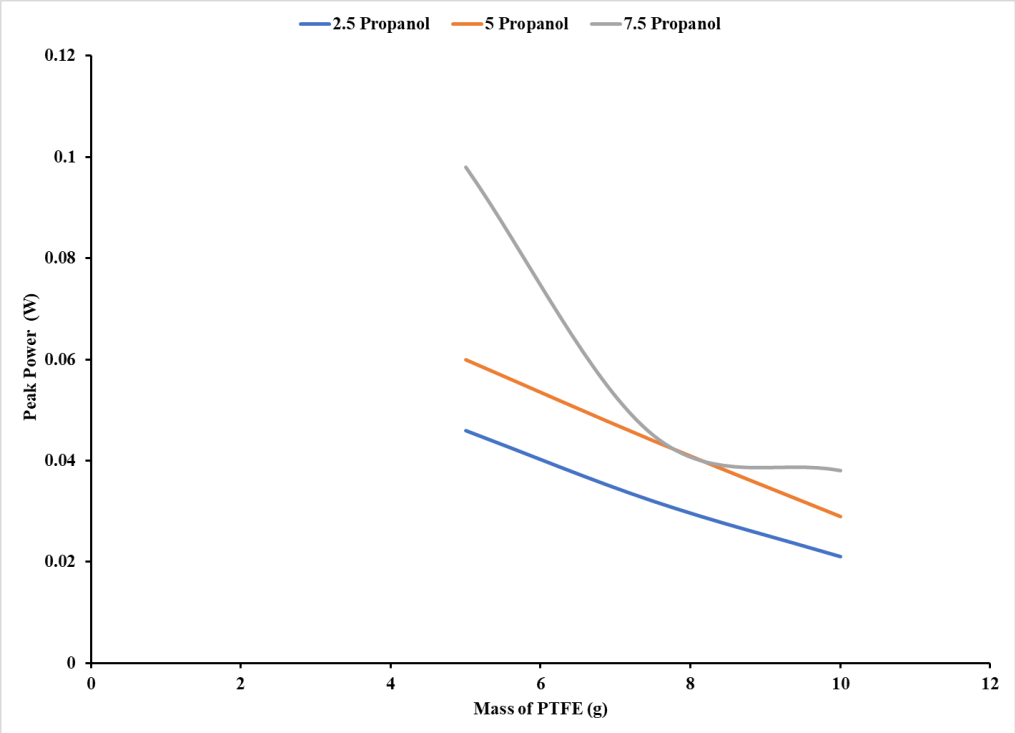

Figure 4.4: Peak Power Value for Various Mass of PTFE and Propanol

Thus, to improve the performance, it can be done in two ways, which is increasing the mass ratio of propanol or reducing the mass ratio of PTFE.

Thus, to further verify the concept, another sample is fabricated. As the mass ratio of Propanol to PTFE of batch 2 samples just varies between the ratio range from 0.25 : 1 to 1.5 : 1, for the modified sample, MS1, the mass ratio of propanol is further increasing to 3 while maintaining the mass ratio of PTFE to prove the concept. Since the main focus in this section is the effect of propanol and PTFE towards the performance, the mass ratio of carbon black, activated carbon and MnO_2 shall be maintained as 9: 1: 2 and this powder mixture shall be in the total mass of 2.5 g. In general, the mass ratio of the powder mixture (carbon black, activated carbon and MnO_2), propanol and PTFE shall be 1: 3: 1.

As sample 16 is the first rank among the batch 2 samples, thus it is pointed up to compare with MS 1. The comparison of the mass ratio of each material for sample 16 and MS1 is stated in Table 4.26. Theoretically, the outputs of MS1 shall be better than all results of batch 2 samples, since the mass ratio of propanol of MS1 is the highest among all samples.

Table 4.26: Mass Ratio of Sample 16 and MS 1

Sample	Carbon Black (g)	Activated Carbon (g)	MnO_2 (g)	Propanol (g)	PTFE (g)	Propanol:PTFE
16	1.88	0.21	0.42	7.5	5	1.5:1
MS 1				7.5	2.5	3:1

Similar way done before, the graphs obtained of MS 1 from the discharge test and LSV test are shown in Figure 4.5 and Figure 4.6 respectively. Then, the comparison of outputs for sample 16 and MS 1 is shown in Table 4.27.

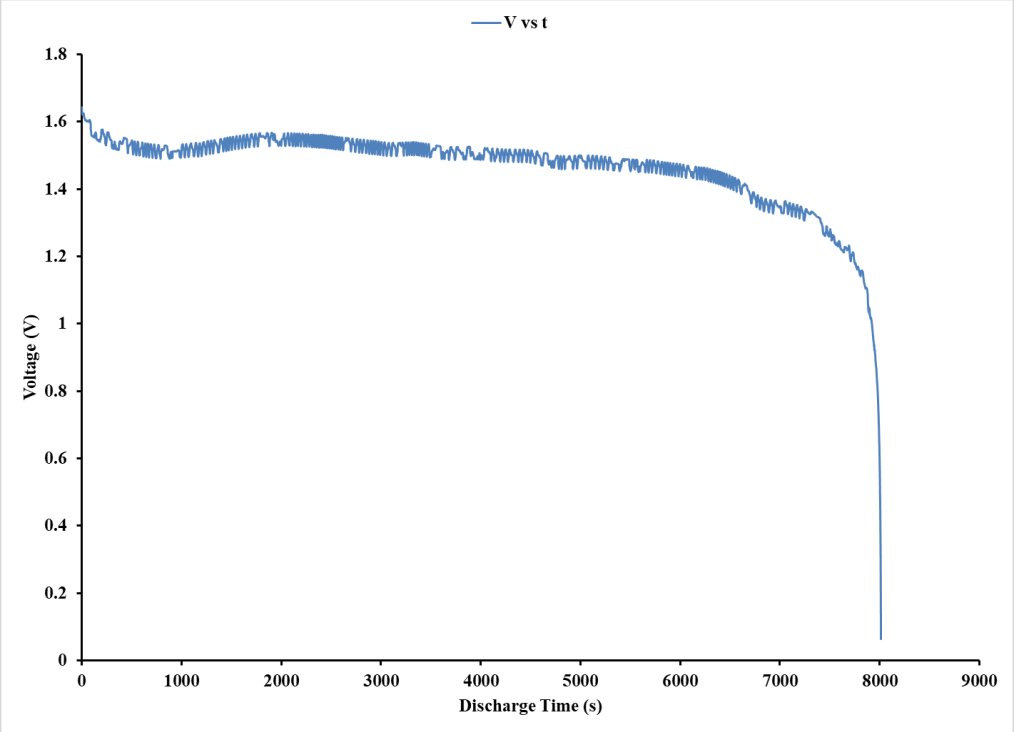

Figure 4.5: Discharge Graph of MS 1

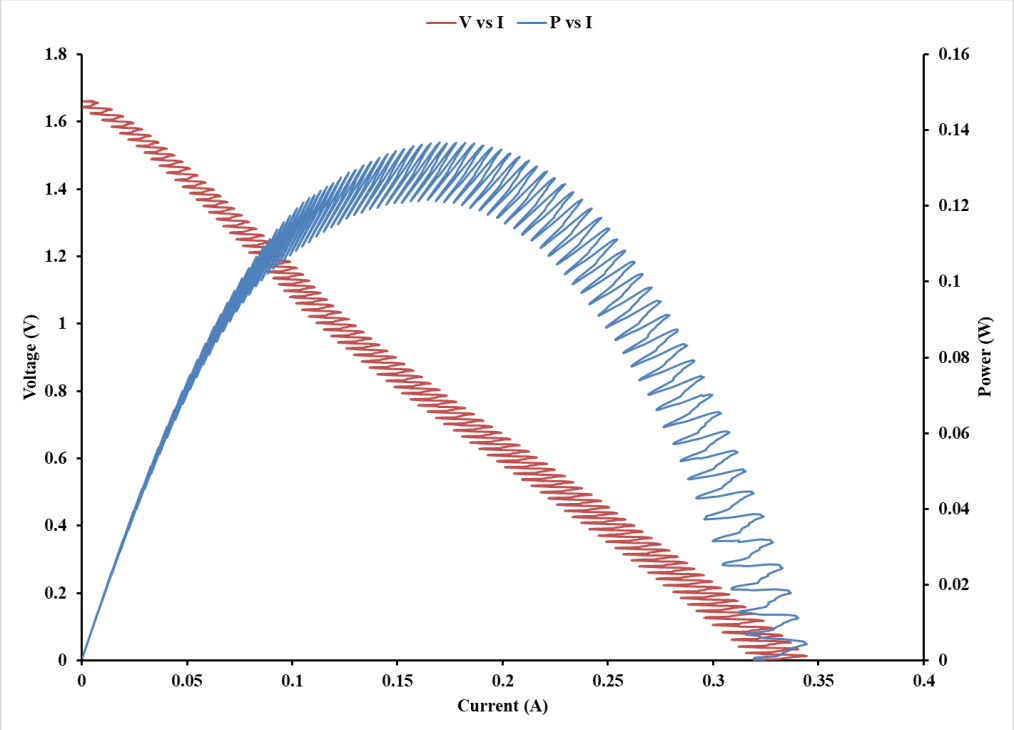

Figure 4.6: LSV Graph of MS 1

Table 4.27: Comparison Table of Sample 16 and MS 1 Outputs

Sample	Discharge		LSV	
	Plateau Voltage (V)	Specific Capacity (Ah/g)	Peak Power (W)	Shutdown current (A)
16	1.1	2.500	0.098	0.2673
MS 1	1.5	2.046	0.137	0.3247

From the results shown, the MS1 has the performance which is much better than all samples of batch 2. This result obtained is lined with the expectation and then verified the assumption. To provide a clearer comparison, Table 4.28 below compares the outputs of MS 1 and sample 15, which is the lowest rank among batch 2 samples, indicating that the poorest performance among the batch 2 samples. As shown in Table 4.28, except for specific capacity, MS 1 performance on the other three parameters is much better than that of sample 15, especially for the plateau voltage, the performance of MS 1 is 5 times better than sample 15. This further indicates the importance of optimization of propanol and PTFE towards the performance of aluminium-air batteries.

The excellent performance obtained from MS 1 can be compared with similar published works. Tan et al. (2024) fabricated an AAB by using 1M KOH electrolyte also and obtained the maximum value of specific capacity of 0.375 Ah/g and 0.3375 Wh/g of specific energy capacity. The specific energy capacity of MS 1 can be calculated by multiplying the plateau voltage and specific capacity, the calculated specific energy capacity shall be 3.069 Wh/g. By comparing both results, MS 1 is capable of providing 5.5 times higher specific capacity and 9 times higher specific energy capacity than the works of Tan et al. This is because the air cathode fabricated by Tan et al. is simply the carbon cloth with a thickness of 0.167 mm while the air cathode of MS 1 is the optimized result throughout this project. This difference in the performance obtained further emphasized the importance of the material composition optimization of air cathode.

Table 4.28: Comparison Table of Sample 15 and MS 1 Outputs

Sample	Discharge		LSV	
	Plateau Voltage (V)	Specific Capacity (Ah/g)	Peak Power (W)	Shutdown current (A)
15	0.3	2.462	0.029	0.1617
MS 1	1.5	2.046	0.137	0.3247

However, based on the result findings, the mass ratio of propanol and PTFE of MS1 can be treated as a limit to further increase the propanol mass ratio. It is because, up to the 3:1 mass ratio of propanol to PTFE, the powder mixture is no longer capable of absorbing all the propanol as shown in Figure 4.7. Thus, it can be said that the 3:1 of propanol to PTFE mass ratio is already the best result for the optimization of PTFE and Propanol. To further improve the performance, perhaps, might back to the optimization of carbon black, activated carbon and manganese (iv) oxide.

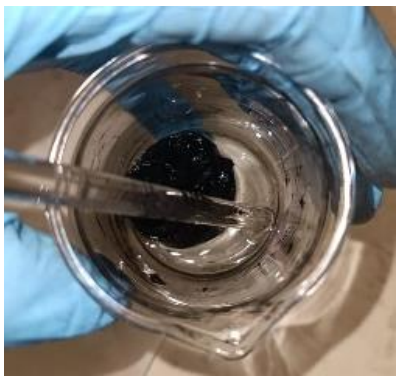

Figure 4.7: Excess Propanol Could Not Absorbed by the Mixture

4.4 Summary

The batch 1 samples are fabricated to optimized the mass ratio of carbon black, activated carbon and manganese (iv) oxide. The results proposed that the mass ratio of carbon black shall be higher and the mass ratio of activated carbon shall be lower to obtain better performance. To verify this finding, another 2 samples (CS 1 and CS 2) were fabricated and the results obtained further supported the finding.

The batch 2 samples are fabricated to optimized the propanol and PTFE. The results showed that the mass ratio of propanol shall be higher and the mass ratio of PTFE shall be lower. In the sense of result verification, the sample MS 1 is fabricated and tested. The testing result of MS 1 shows that the limit mass ratio of Propanol and PTFE shall be 3:1, and the output of MS 1 shall be the best result for the optimization of propanol and PTFE.

There are quite a number of unstable plots obtained during the experiments. This is due to the degree of sensitivity of the potentiostat and can be fixed by simply adjusting the setting. Thus, the accuracy of results is not affected.

CHAPTER 5

CONCLUSIONS AND RECOMMENDATIONS

5.1 Conclusions

From the output of this project, the sample label MS 1 shall be the optimized material compositions result for the air cathode of an aluminium-air battery. The optimized mass ratio of the carbon black, activated carbon and manganese (iv) oxide, which in the total mass of mixture in x, shall be 9:1:2 respectively. The mass ratio of the powder mixture, propanol and PTFE shall be x:3x:x respectively. The expected output of the optimized aluminium-air battery shall be 1.5 V of plateau voltage, 2.046 Ah/g of specific capacity, 0.137 W of peak power and 0.3247 A of shutdown current.

Among the research results, the optimization of the propanol and PTFE shall reach to the limit for further improvement, as the propanol is no longer to be absorbed by the powder mixture if further increase the mass ratio of propanol. For the optimization of the powder mixture, which is carbon black, activated carbon and manganese (iv) oxide, is believed that still having some space for improvement since there are still a number of variables and factors for the compositions.

Lastly, some information extracted from this project's outcomes can be the general recommendation for future works, which are the mass ratio of Activated Carbon and PTFE must be lower and the mass ratio of Carbon Black and Propanol needs to be higher.

5.2 Recommendations for future work

The fabrication method of the aluminium-air batteries casing is recommended to change to 3D printing for more accurate and precise dimension control. This is stated as because the acrylic board will tend to bend after laser cutting and this will lead to the deviation of dimension when sticking them together by chlorofoam. The slight changes in the dimension of the casing will then affect the immerse height of the aluminium anode inside the KOH electrolyte, and thus affect the discharge time. This error can be overcome easily by selecting

the specific capacity as a replacement parameter of discharge time for analysis to take consideration of the mass difference of aluminium anode. However, the 3D printing fabrication method is still recommended for more standardized and professional quality control.

Another improvement for future works may be the hydrophobic characteristic of aluminium-air batteries. This is stated because the water leakage is found on the coated surface of the air cathode after a long period of operation as shown in Figure 5.1.

Figure 5.1: Water Leakage Found after Long Period of Operation

The design of the hydrophobic characteristic of the air cathode may rely on the contents of PTFE. According to Fatemeh Shakerihosseinabad et al. (2023), the presence of PTFE will improve the hydrophobic performance of the prototype. In their research, the air cathode was divided into a few components, which include the active layer that is near the electrolyte, the current collector made from nickel mesh and the backing layer that is exposed to the air. The active layer is made from Pt/C with a lower amount of PTFE ranging between 2 to 25 wt%, while the backing layer is made from carbon and PTFE. The partial adhesion of PTFE will provide the primary hydrophobic characteristic of the air cathode. The works from Liu et al. (2020) also proposed the use of PTFE for hydrophobic air cathode design, where the air

cathode is made by brushing two dispersion solutions onto the nickel foam. Solution A is made from PTFE, acetylene black and isopropanol, while solution B is made from Pt/C, Nafion and isopropanol. However, according to Fatemeh Shakerihosseinabad et al. (2023), the presence of PTFE will result in the reduction of porosity, and similar to the results found in Chapter 4, will lower the AAB performance. Thus, there is a need to conduct additional research regarding this matter to strike a balance between the output performance and robust hydrophobic characteristics of an AAB.

REFERENCES

Aleksandrs Vališevskis, Briedis, U., Žaneta Juchnevičienė, Jucienė, M. and Carvalho, M., 2019. Design improvement of flexible textile aluminium-air battery. *Journal of The Textile Institute*, 111(7), pp.985–990. doi:https://doi.org/10.1080/00405000.2019.1676521.

Buckingham, R., Asset, T. and Atanassov, P., 2021. Aluminum-air batteries: A review of alloys, electrolytes and design. *Journal of Power Sources*, [online] 498, p.229762. doi:https://doi.org/10.1016/j.jpowsour.2021.229762.

Bruce, P.G., Freunberger, S.A., Hardwick, L.J. and Tarascon, J.-M., 2011. Li–O2 and Li–S batteries with high energy storage. *Nature Materials*, [online] 11(1), pp.19–29. doi:https://doi.org/10.1038/nmat3191.

Chen, H., Cong, T.N., Yang, W., Tan, C., Li, Y. and Ding, Y., 2009. Progress in electrical energy storage system: A critical review. *Progress in Natural Science*, 19(3), pp.291–312. doi:https://doi.org/10.1016/j.pnsc.2008.07.014.

Cimbala, J. , 2014. *Taguchi Orthogonal Arrays*. [online] Available at: https://www.me.psu.edu/cimbala/me345/Lectures/Taguchi_orthogonal_arrays.pdf.

Cho, Y.-J., Park, I.-J., Lee, H.-J. and Kim, J.-G., 2015. Aluminum anode for aluminum–air battery – Part I: Influence of aluminum purity. *Journal of Power Sources*, 277, pp.370–378. doi:https://doi.org/10.1016/j.jpowsour.2014.12.026.

Chawla, N., Bharti, N. and Singh, S., 2019. Recent Advances in Non-Flammable Electrolytes for Safer Lithium-Ion Batteries. *Batteries*, 5(1), p.19. doi:https://doi.org/10.3390/batteries5010019.

Egan, D.R., Ponce de León, C., Wood, R.J.K., Jones, R.L., Stokes, K.R. and Walsh, F.C., 2013. Developments in electrode materials and electrolytes for aluminium–air batteries. *Journal of Power Sources*, [online] 236, pp.293–310. doi:https://doi.org/10.1016/j.jpowsour.2013.01.141.

Fatemeh Shakerihosseinabad, Alireza Sadeghi Alavijeh, Mahmood Khalghollah, Shukla, S., Abouali, S., Orfino, F.P., Nader Mahinpey, Kjeang, E., Fan, S. and Edward P.L. Roberts (2023). The role of hydrophobicity and active layer thickness on degradation and durability of the air cathode in alkaline fuel cells. *Journal of power sources*, 578, pp.233209–233209. doi:https://doi.org/10.1016/j.jpowsour.2023.233209.

Felipe, Kumar, A. and Gupta, R.K., 2023. Metal-Air Batteries. pp.1–13. doi:https://doi.org/10.1201/9781003295761-1.

Ganesan, P., Prabu, M., Sanetuntikul, J. and Shanmugam, S., 2015. Cobalt Sulfide Nanoparticles Grown on Nitrogen and Sulfur Codoped Graphene

Oxide: An Efficient Electrocatalyst for Oxygen Reduction and Evolution Reactions. *ACS Catalysis*, 5(6), pp.3625–3637. doi:https://doi.org/10.1021/acscatal.5b00154.

Gao, J., Li, Y., Zhao, Y., Liu, Q., Gao, Y., Chen, C., Ma, B., Song, Y. and Wang, E., 2019. Effects of solid-solute magnesium and stannate ion on the electrochemical characteristics of a high-performance aluminum anode/electrolyte system. 412, pp.63–70. doi:https://doi.org/10.1016/j.jpowsour.2018.11.019.

Goel, P., Dobhal, D. and Sharma, R.C., 2020. Aluminum–air batteries: A viability review. *Journal of Energy Storage*, 28, p.101287. doi:https://doi.org/10.1016/j.est.2020.101287.

Kang, Q., Zhang, T.Y., Wang, X., Wang, Y. and Zhang, X.Y., 2019. Effect of cerium acetate and L-glutamic acid as hybrid electrolyte additives on the performance of Al–air battery. *Journal of Power Sources*, 443, pp.227251–227251. doi:https://doi.org/10.1016/j.jpowsour.2019.227251.

Kotcioglu, I., Cansiz, A. and Nasiri Khalaji, M. (2013). Experimental investigation for optimization of design parameters in a rectangular duct with plate-fins heat exchanger by Taguchi method. *Applied Thermal Engineering*, 50(1), pp.604–613. doi:https://doi.org/10.1016/j.applthermaleng.2012.05.036.

Ibrahim, H., Ilinca, A. and Perron, J., 2008. Energy storage systems—Characteristics and comparisons. *Renewable and Sustainable Energy Reviews*, 12(5), pp.1221–1250. doi:https://doi.org/10.1016/j.rser.2007.01.023.

Li, Y. and Lu, J., 2017. Metal–Air Batteries: Will They Be the Future Electrochemical Energy Storage Device of Choice? *ACS Energy Letters*, 2(6), pp.1370–1377. doi:https://doi.org/10.1021/acsenergylett.7b00119.

Liu, B., Dai, Y.-K., Li, L., Zhang, H.-D., Zhao, L., Kong, F.-R., Sui, X.-L. and Wang, Z.-B. (2020). Effect of polytetrafluoroethylene (PTFE) in current collecting layer on the performance of zinc-air battery. *Progress in Natural Science/Progress in natural science*, 30(6), pp.861–867. doi:https://doi.org/10.1016/j.pnsc.2020.09.012.

Liu, Q., Pan, Z., Wang, E., An, L. and Sun, G., 2020. Aqueous metal-air batteries: Fundamentals and applications. *Energy Storage Materials*, [online] 27, pp.478–505. doi:https://doi.org/10.1016/j.ensm.2019.12.011.

Liu, X., Zhang, P., Xue, J., Zhu, C., Li, X. and Wang, Z., 2021. High energy efficiency of Al-based anodes for Al-air battery by simultaneous addition of Mn and Sb. *Chemical Engineering Journal*, 417, pp.128006–128006. doi:https://doi.org/10.1016/j.cej.2020.128006.

Li, Z. and Zhang, G., 2023. Carbon-Based Electrocatalysts for Metal-Air Batteries. *CRC Press eBooks*, pp.195–207. doi:https://doi.org/10.1201/9781003295761-14.

Li, S., Li, E., An, X. and Guan, G., 2023. Electrochemical Fundamentals and Issues of Metal-Air Batteries. pp.29–43. doi:https://doi.org/10.1201/9781003295761-3.

Ma, J., Wen, J., Gao, J. and Li, Q., 2014. Performance of Al−1Mg−1Zn−0.1Ga−0.1Sn as anode for Al-air battery. *Electrochimica Acta*, 129, pp.69–75. doi:https://doi.org/10.1016/j.electacta.2014.02.080.

Manthiram, A., 2017. An Outlook on Lithium Ion Battery Technology. *ACS Central Science*, [online] 3(10), pp.1063–1069. doi:https://doi.org/10.1021/acscentsci.7b00288.

M.A. Deyab, 2019. Effect of nonionic surfactant as an electrolyte additive on the performance of aluminum-air battery. 412, pp.520–526. doi:https://doi.org/10.1016/j.jpowsour.2018.11.086.

Mori, R., 2020. Recent Developments for Aluminum–Air Batteries. *Electrochemical Energy Reviews*. doi:https://doi.org/10.1007/s41918-020-00065-4.

Naqiuddin, NH, Saw, LH, Yew, MC, Yusof, F, Poon, HM, Cai, Z & Thiam, HS, 2018. Numerical investigation for optimizing segmented micro-channel heat sink by Taguchi-Grey method. *Applied Energy*, 222437–450. doi:https://doi.org/10.1016/j.apenergy.2018.03.186.

Nit Namwong and Chaiyaput Kruehong, 2022. Chain-like carbon nano-onions from candle flame combustion as a high-performance cathode for aluminum-air batteries. *Diamond and Related Materials*, 129, pp.109396–109396. doi:https://doi.org/10.1016/j.diamond.2022.109396.

Olabi, A.G., Sayed, E.T., Wilberforce, T., Jamal, A., Alami, A.H., Elsaid, K., Rahman, S.M.A., Shah, S.K. and Abdelkareem, M.A., 2021. Metal-Air Batteries—A Review. *Energies*, 14(21), p.7373. doi:https://doi.org/10.3390/en14217373.

Qazi, M.I., Abas, M., Khan, R., Saleem, W., Pruncu, C.I. and Omair, M. (2021). Experimental Investigation and Multi-Response Optimization of Machinability of AA5005H34 Using Composite Desirability Coupled with PCA. *Metals*, 11(2), p.235. doi:https://doi.org/10.3390/met11020235.

Rahman, Md.A., Wang, X. and Wen, C., 2013. High Energy Density Metal-Air Batteries: A Review. *Journal of The Electrochemical Society*, 160(10), pp.A1759–A1771. doi:https://doi.org/10.1149/2.062310jes.

Tressler, R., 2022. *Battery capacity testing: what it is, how it works, and why you should be doing it*. [online] Available at: https://www.bestmag.co.uk/battery-capacity-testing-what-it-is-how-it-works-and-why-you-should-be-doing-it/.

Tran, M.-K., Mevawalla, A., Aziz, A., Panchal, S., Xie, Y. and Fowler, M., 2022. A Review of Lithium-Ion Battery Thermal Runaway Modeling and Diagnosis Approaches. *Processes*, 10(6), p.1192. doi:https://doi.org/10.3390/pr10061192.

Tan, WC, Saw, LH, Yew, MC & Yew, MK, 2023. Materials and technologies of Al-Air batteries. *CRC Press eBooks*, pp. 77–88. doi:https://doi.org/10.1201/9781003295761-6.

Tan, WC, Saw, LH, Yew, MC, Thiam, HS & Kuo, PY, (2024). Characterization of the aluminium-air battery utilizing a polypropylene separator with corrosion inhibition ability. *Chemical engineering journal*, pp.151106–151106. doi:https://doi.org/10.1016/j.cej.2024.151106.

Tomar, A., Sakshee Chandel and Alok Kumar Rai, 2023. Materials and Electrochemistry of Metal-Air Battery. pp.15–28. doi:https://doi.org/10.1201/9781003295761-2.

University of Cambridge, 2013. *Linear Sweep and Cyclic Voltametry: The Principles | Department of Chemical Engineering and Biotechnology*. [online] Cam.ac.uk. Available at: https://www.ceb.cam.ac.uk/research/groups/rg-eme/Edu/linear-sweep-and-cyclic-voltametry-the-principles.

Wang, X.F., Wang, J., Wang, Q., Shao, H.M. and Zhang, J., 2010. The effects of polyethylene glycol (PEG) as an electrolyte additive on the corrosion behavior and electrochemical performances of pure aluminum in an alkaline zincate solution. 62(12), pp.1149–1152. doi:https://doi.org/10.1002/maco.201005646.

Wang, D., Li, H., Liu, J., Zhang, D., Gao, L. and Tong, L., 2015. Evaluation of AA5052 alloy anode in alkaline electrolyte with organic rare-earth complex additives for aluminium-air batteries. *Journal of Power Sources*, 293, pp.484–491. doi:https://doi.org/10.1016/j.jpowsour.2015.05.104.

Wang, C., Yu, Y., Niu, J., Liu, Y., Bridges, D., Liu, X., Pooran, J., Zhang, Y. and Hu, A., 2019. Recent Progress of Metal–Air Batteries—A Mini Review. *Applied Sciences*, 9(14), p.2787. doi:https://doi.org/10.3390/app9142787.

www.metals4u.co.uk. (n.d.). *A guide to aluminium grades and their uses.* [online] Available at: https://www.metals4u.co.uk/blog/a-guide-to-aluminium-grades-and-their-uses.

Zhang, L., Huang, Q., Yan, W., Shao, Q. and Zhang, J., 2019. Design and fabrication of non-noble metal catalyst-based air-cathodes for metal-air battery. *The Canadian Journal of Chemical Engineering*, 97(12), pp.2984–2993. doi:https://doi.org/10.1002/cjce.23616.

Zhou, S., Tian, C., Sultan Alzoabi, Xu, Y., Jiao, Z., Luo, K., Peng, B., Zhang, C., Santos, N. and Cao, Y., 2020. Performance of an Al–0.08Sn–0.08Ga–xMg

alloy as an anode for Al–air batteries in alkaline electrolytes. *Journal of Materials Science*, 55(25), pp.11477–11488. doi:https://doi.org/10.1007/s10853-020-04711-6.

Zhang, S., Wang, Y., Li, Y., Wei, M. and Wang, K., 2022. Sodium lignosulphonate decomposing accumulated byproducts of quasi-solid aluminum-air batteries. *Journal of Power Sources*, 549, pp.232088–232088. doi:https://doi.org/10.1016/j.jpowsour.2022.232088.

APPENDICES

Appendix A: Graphs Obtained For Batch 1 Samples

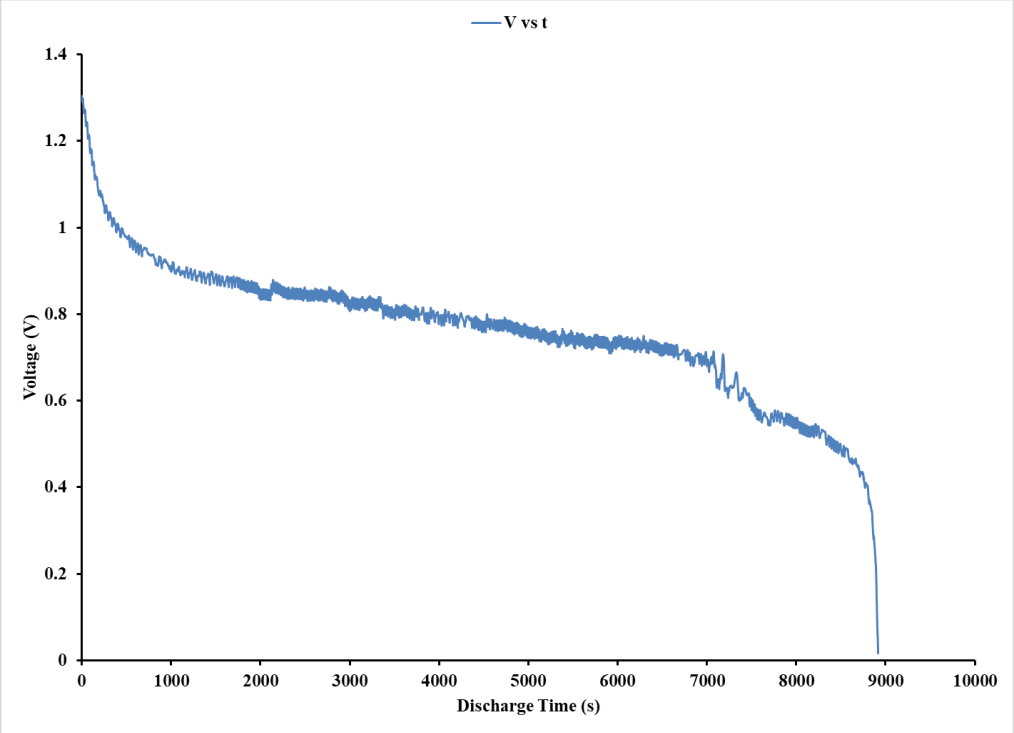

GraphA-1: Discharge Graph of Sample 1

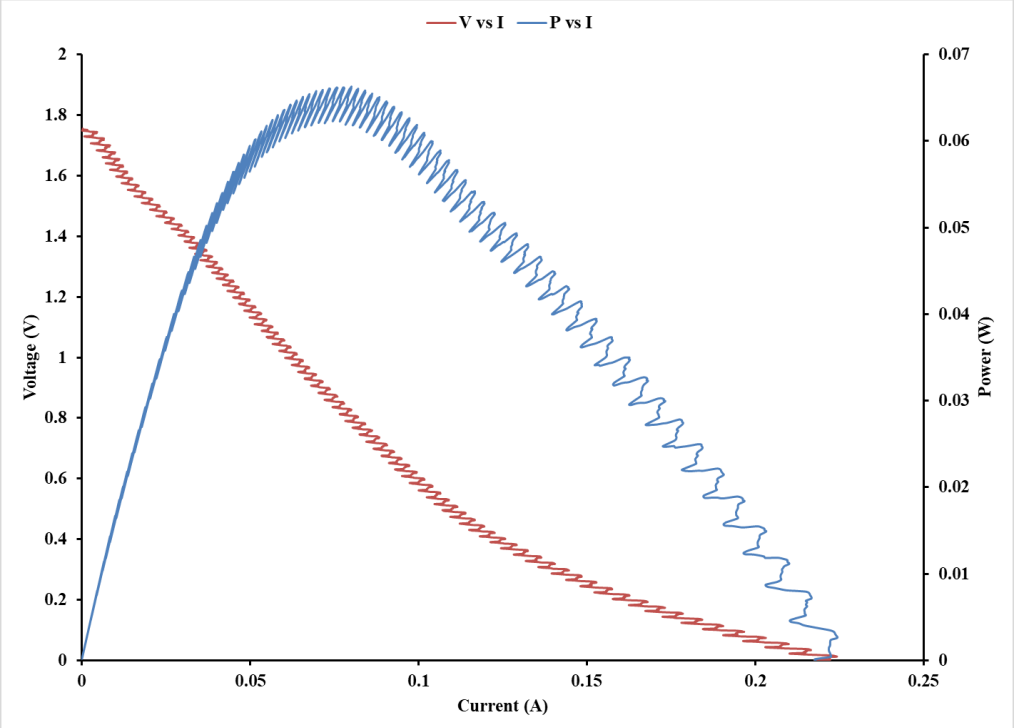

GraphA-2: LSV Graph of Sample 1

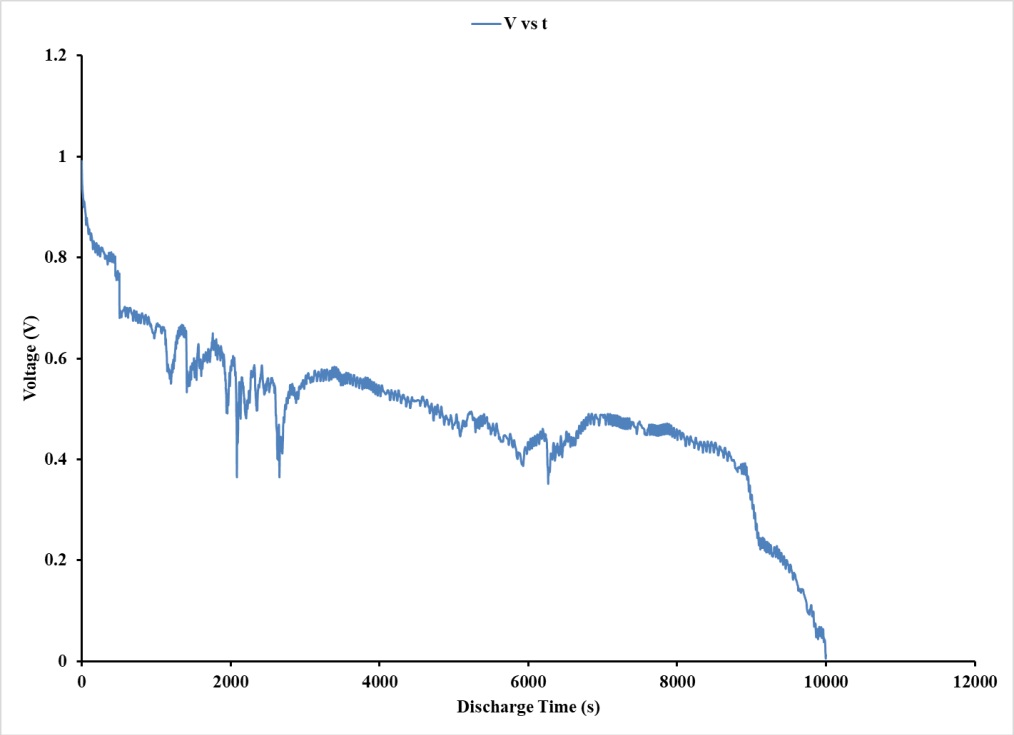

GraphA-3: Discharge Graph of Sample 2

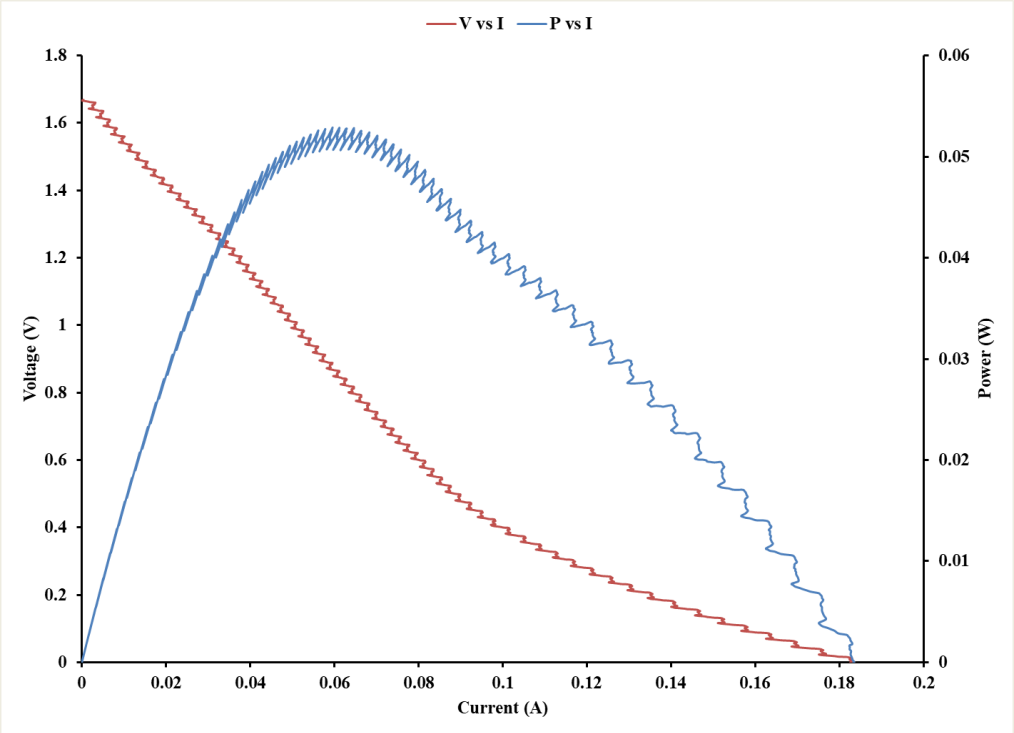

GraphA-4: LSV Graph of Sample 2

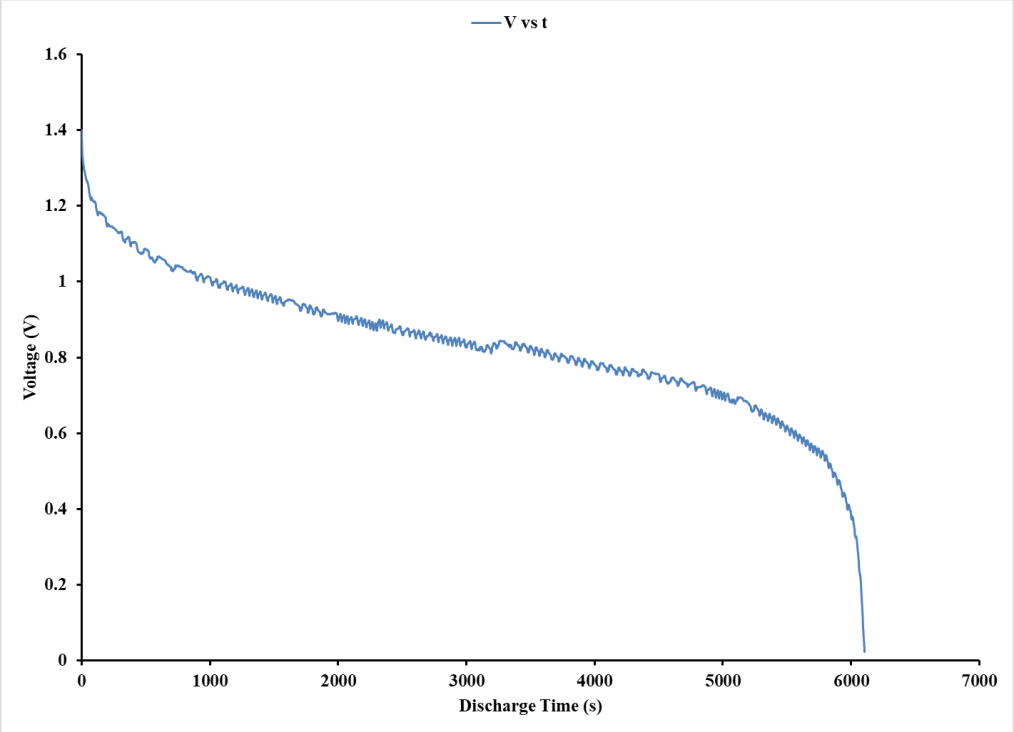

GraphA-5: Discharge Graph of Sample 3

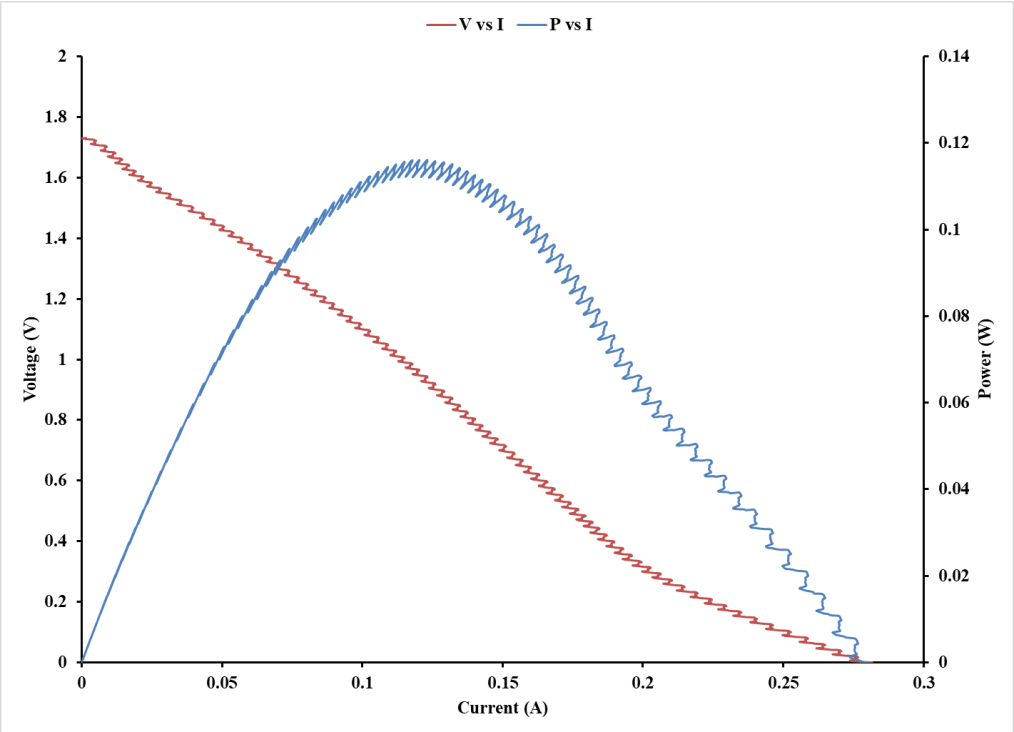

GraphA-6: LSV Graph of Sample 3

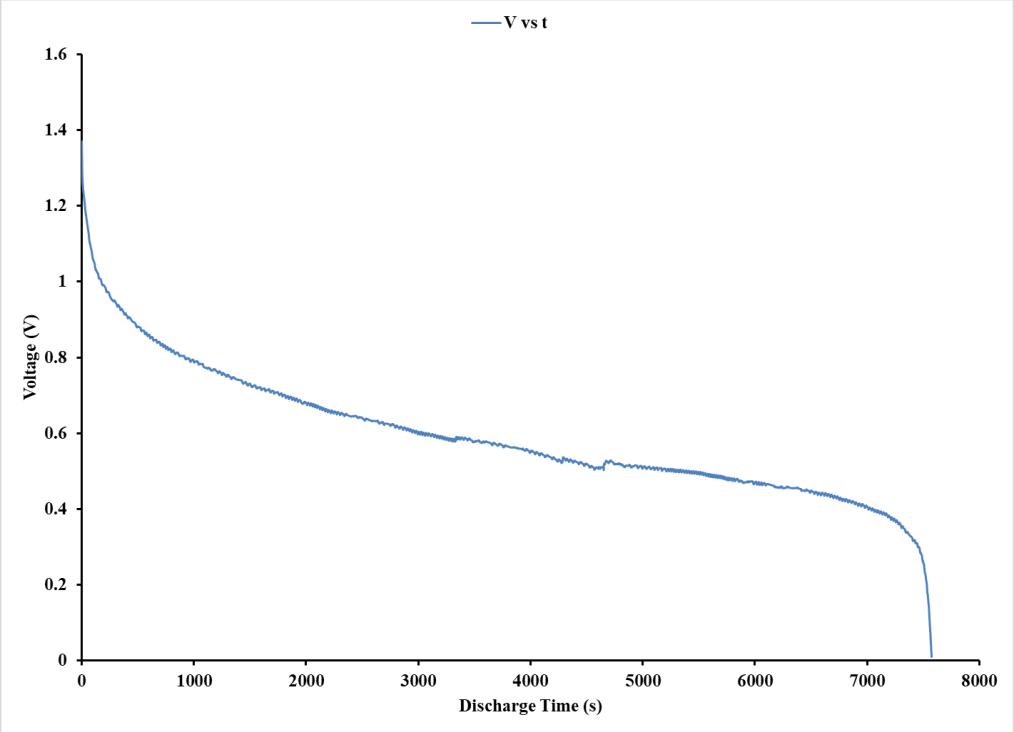

GraphA-7: Discharge Graph of Sample 5

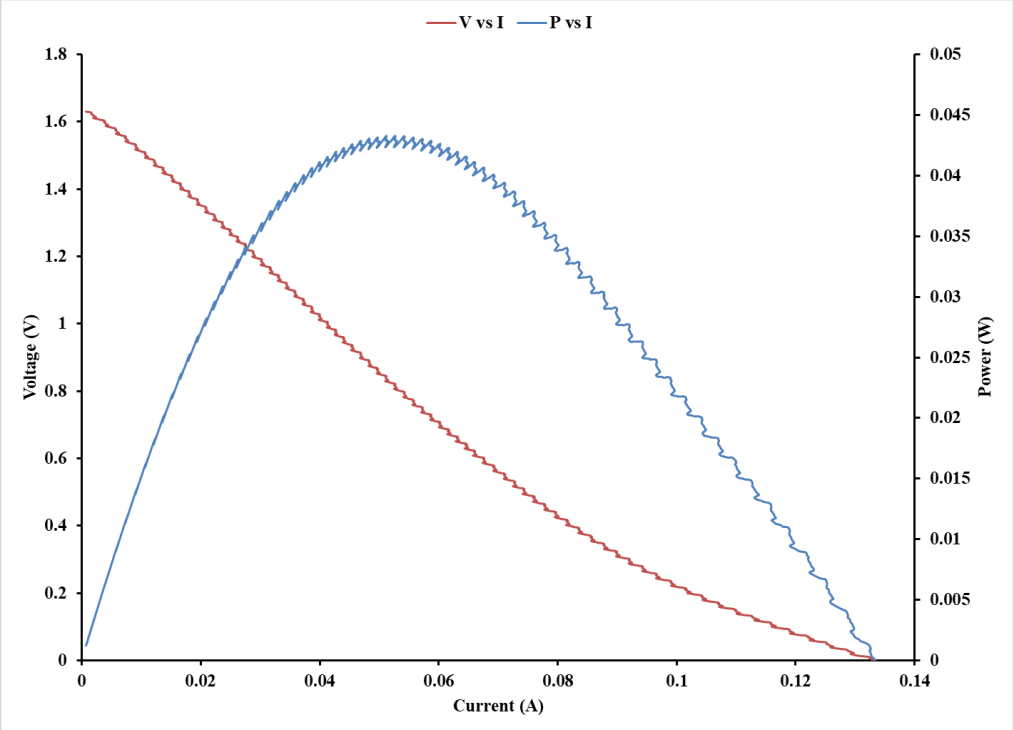

GraphA-8: LSV Graph of Sample 5

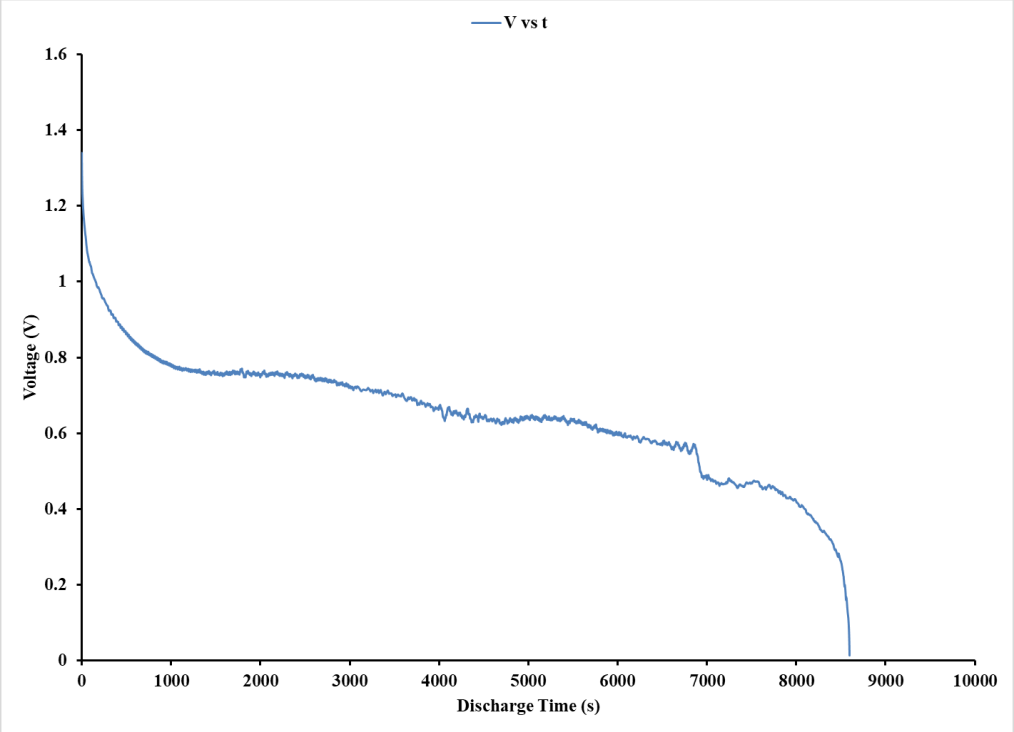

GraphA-9: Discharge Graph of Sample 6

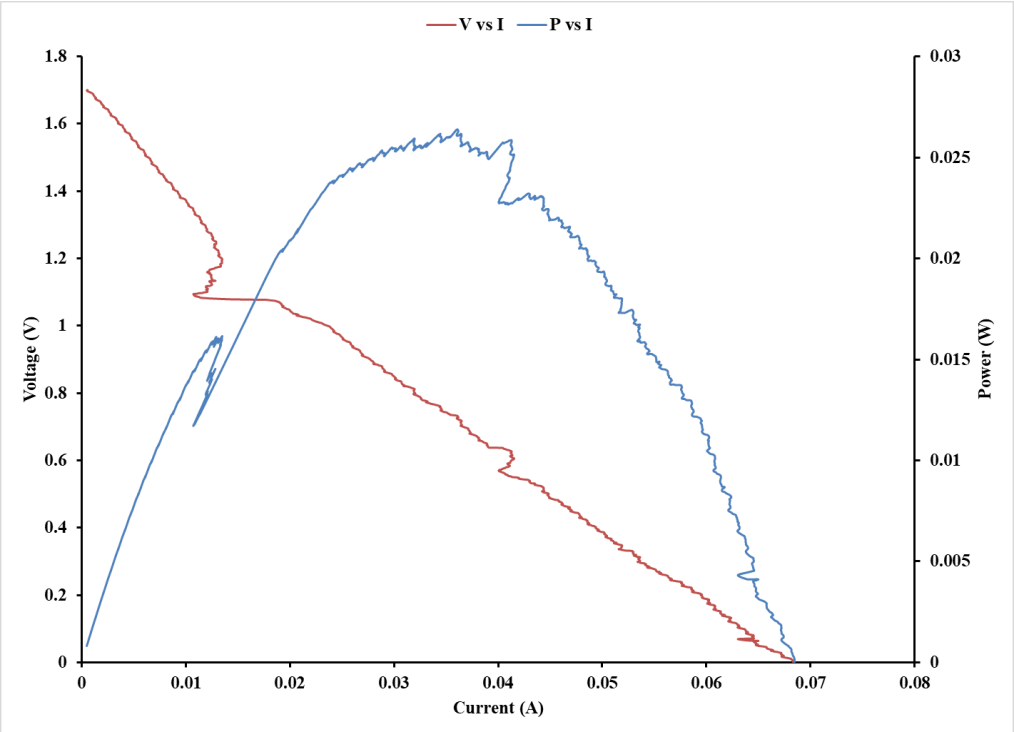

GraphA-10: LSV Graph of Sample 6

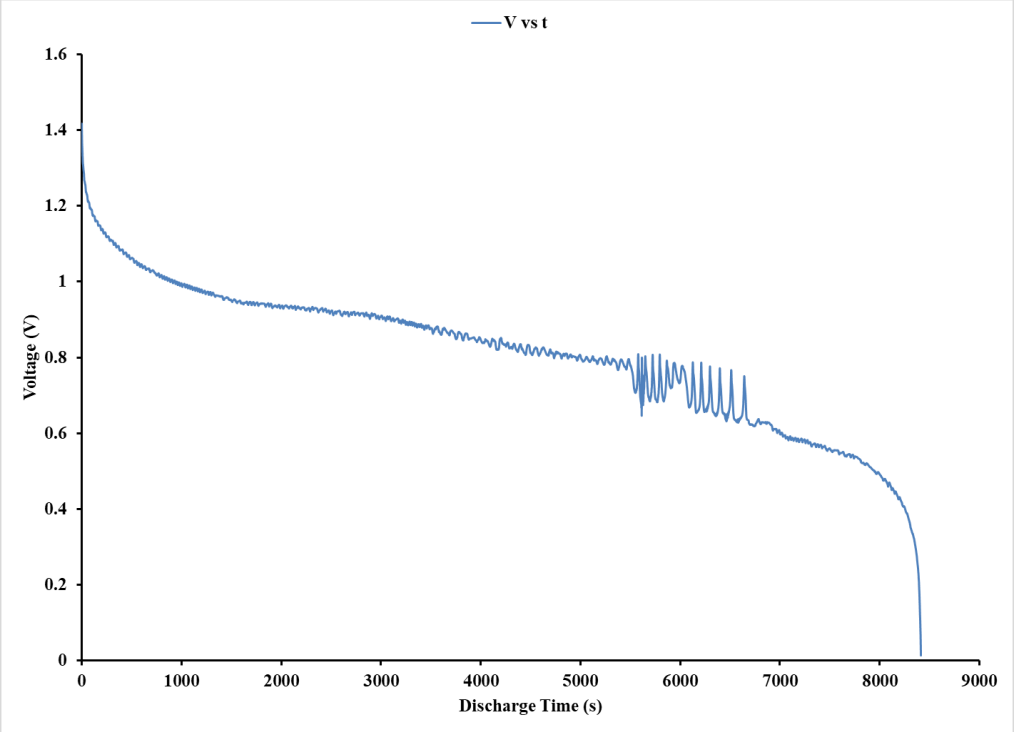

GraphA-11: Discharge Graph of Sample 7

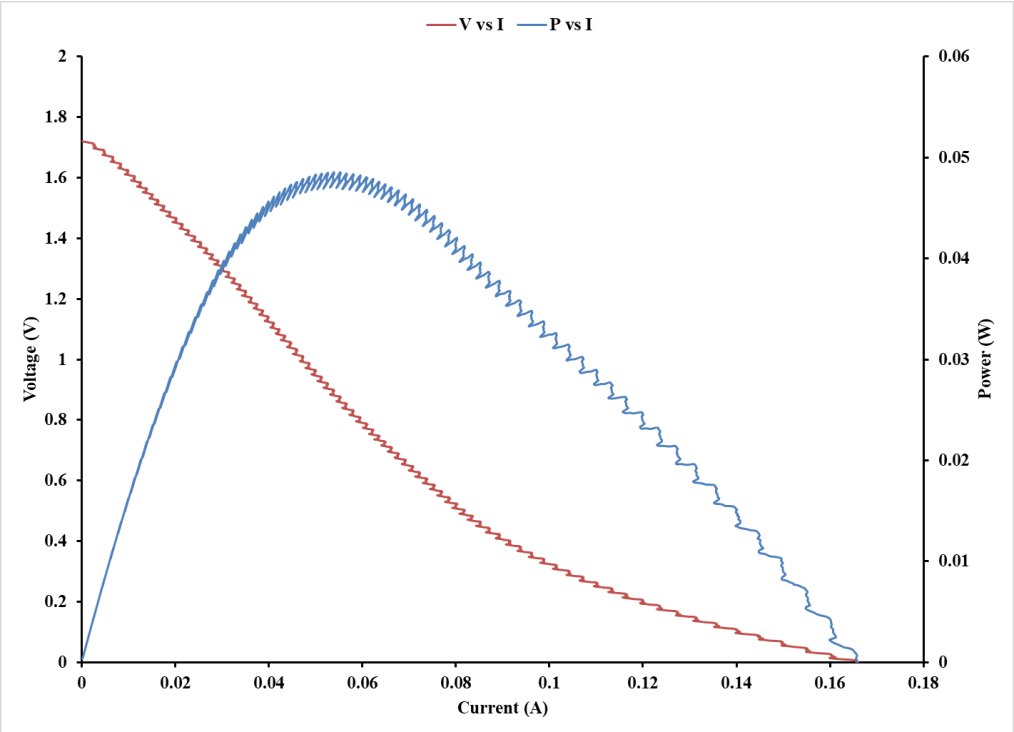

GraphA-12: LSV Graph of Sample 7

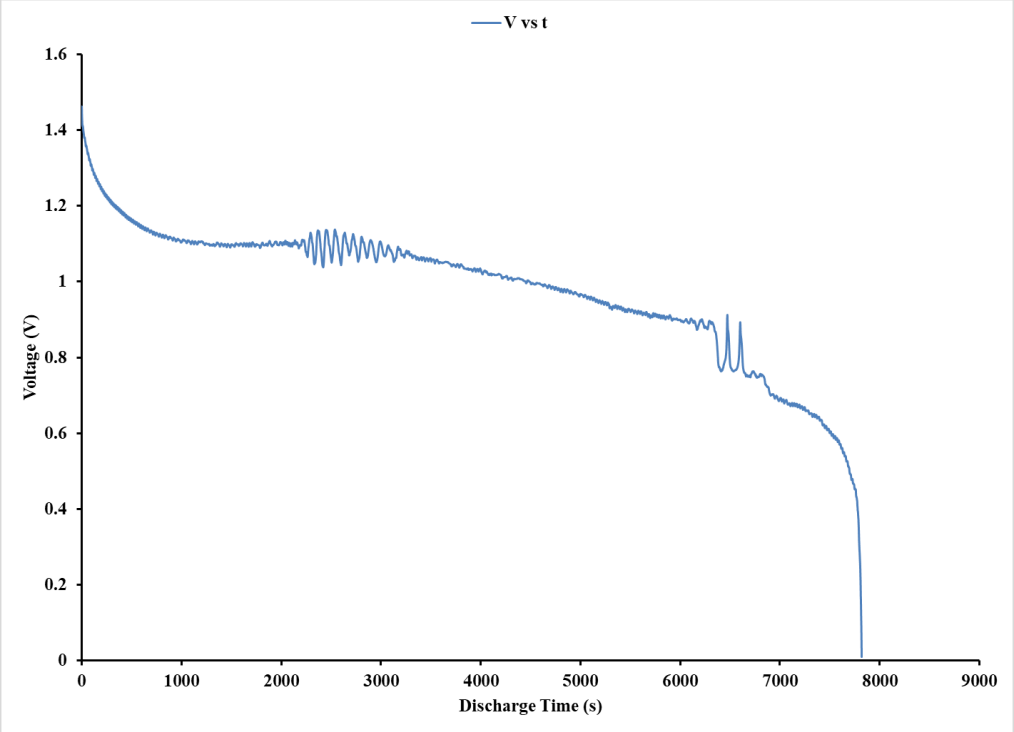

GraphA-13: Discharge Graph of Sample 8

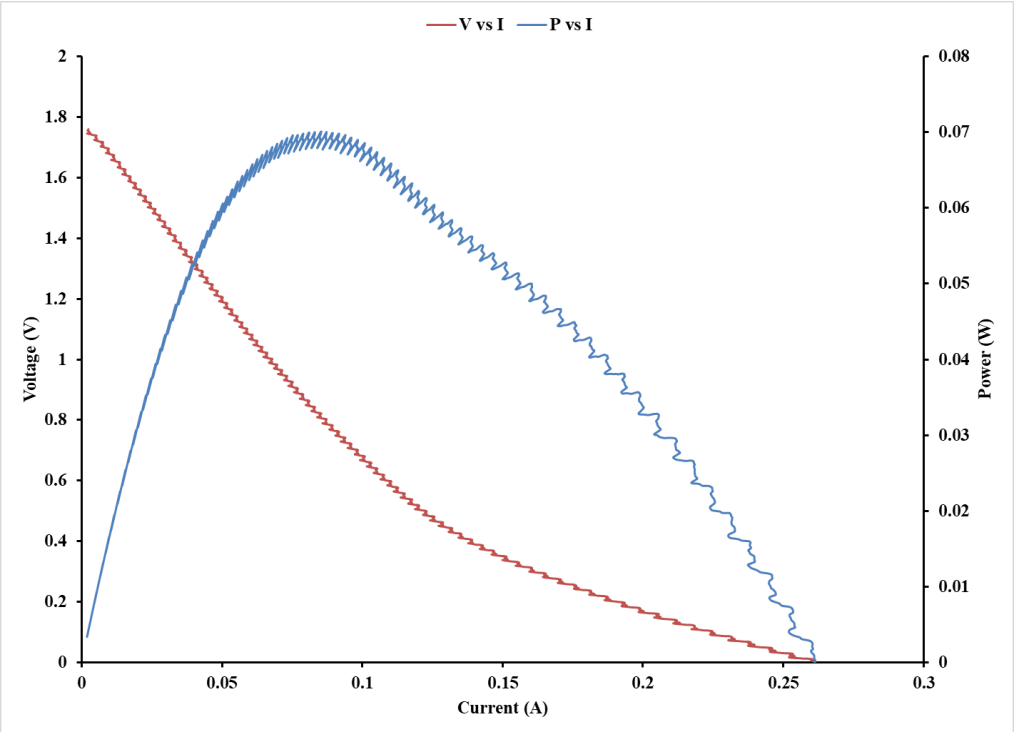

GraphA-14: LSV Graph of Sample 8

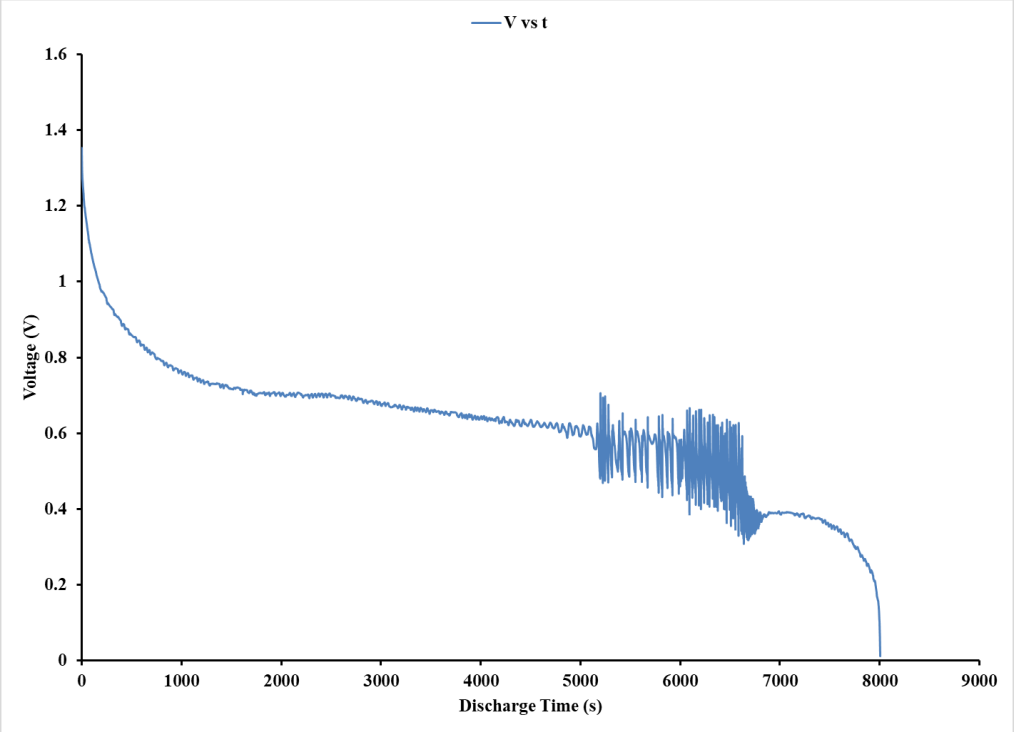

GraphA-15: Discharge Graph of Sample 9

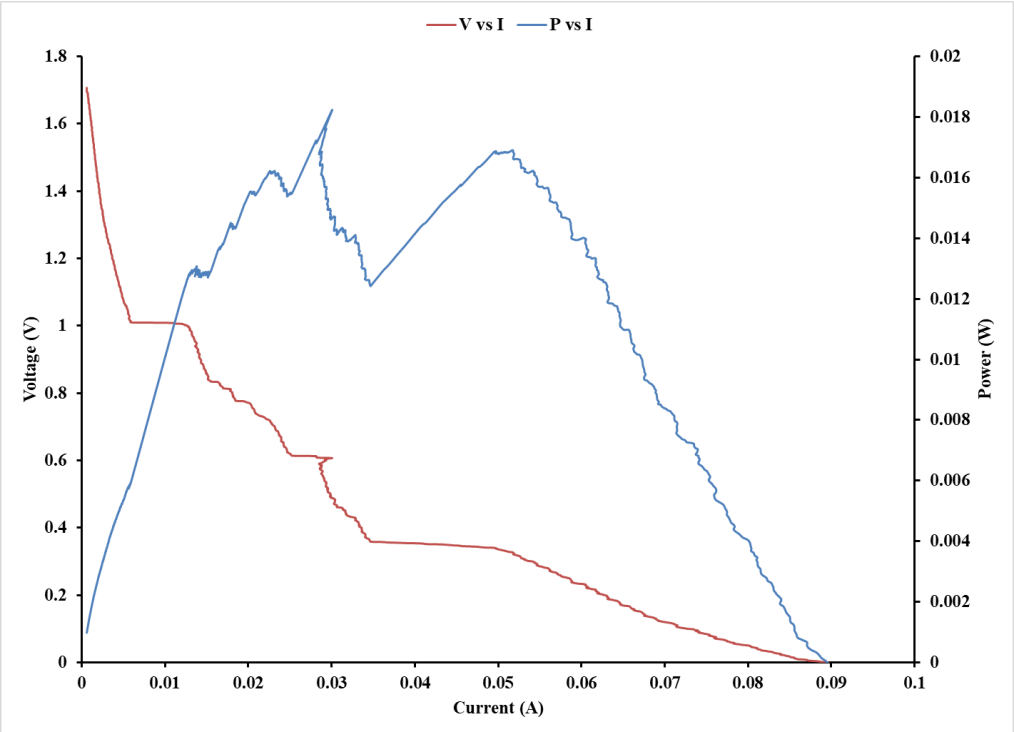

GraphA-16: LSV Graph of Sample 9

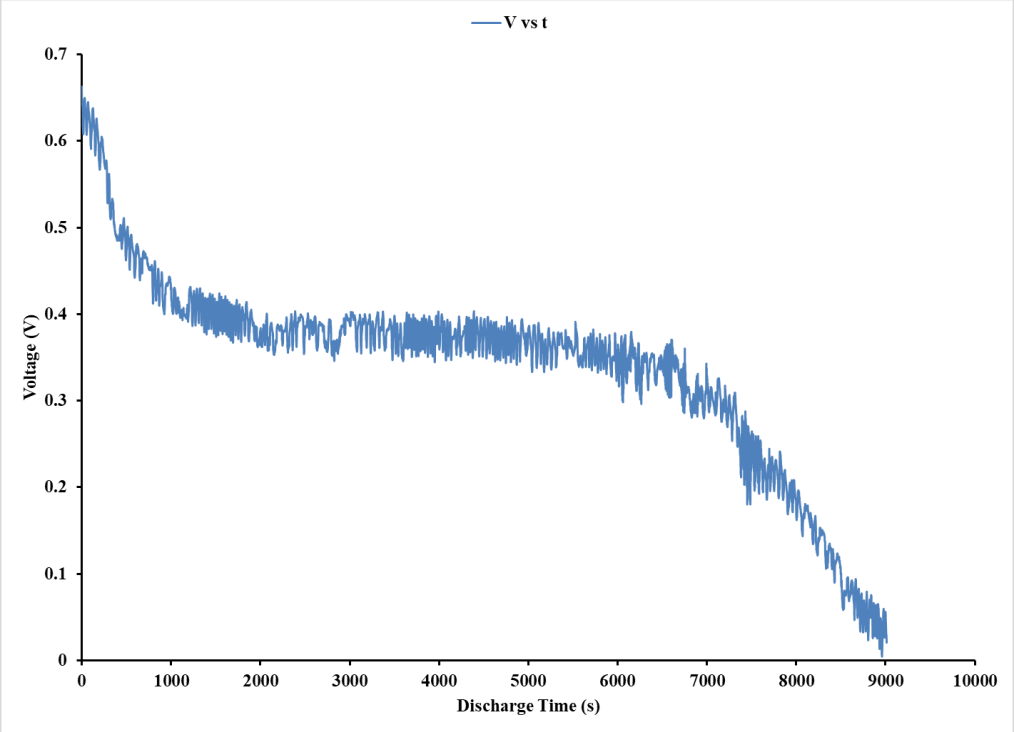

GraphA-17: Discharge Graph of CS 1

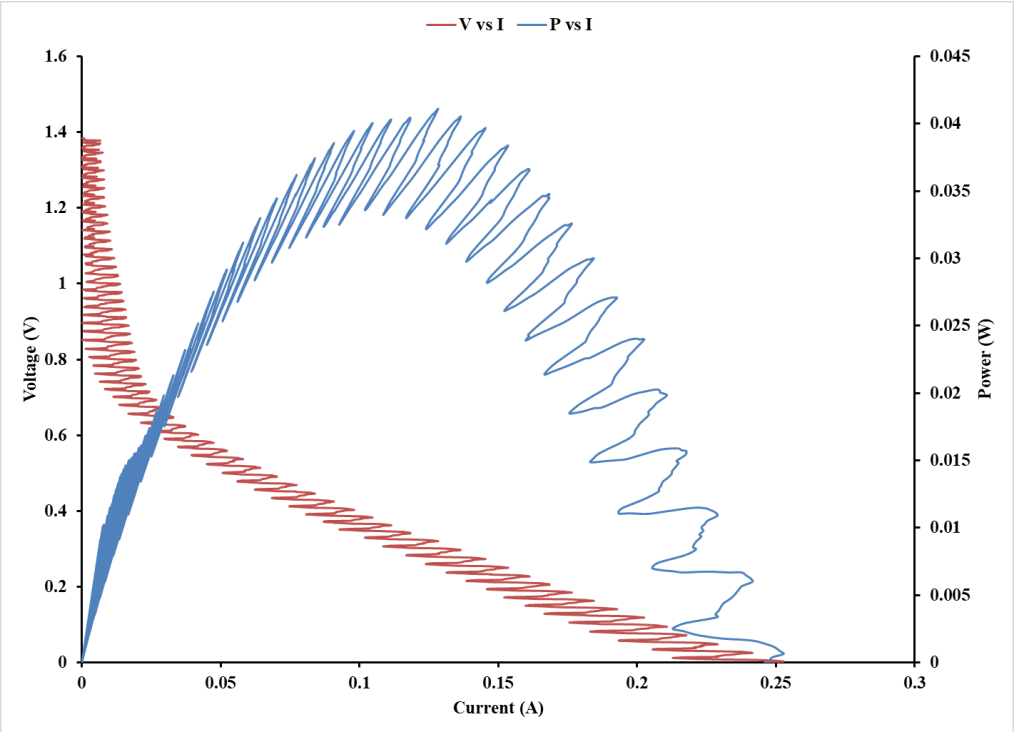

GraphA-18: LSV Graph of CS 1

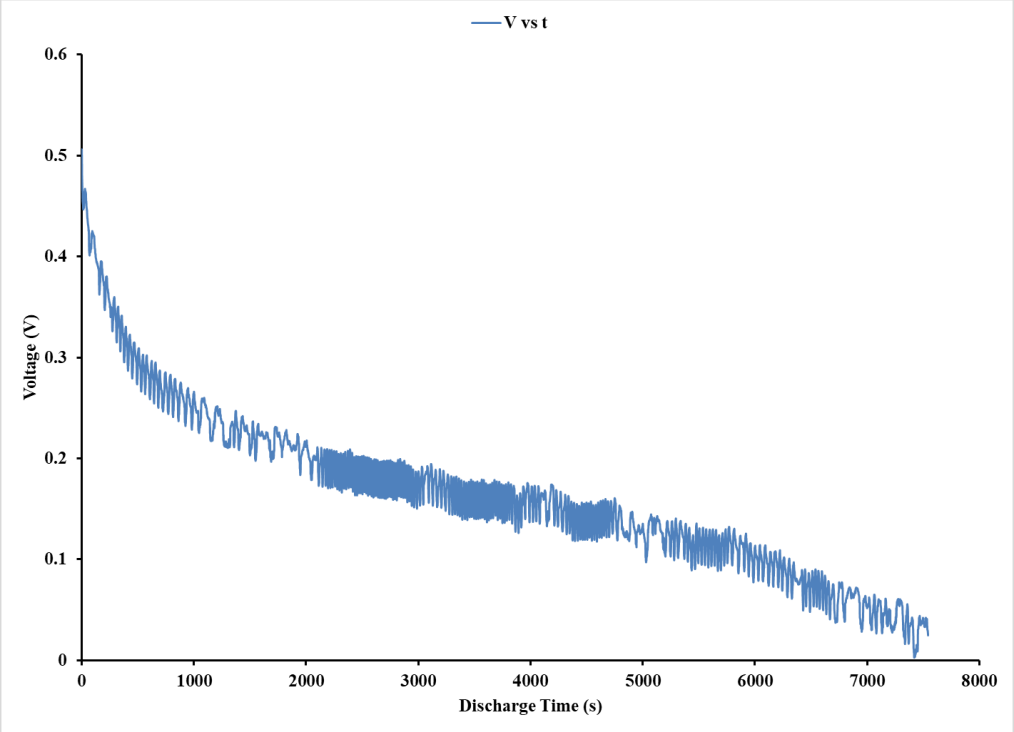

GraphA-19: Discharge Graph of CS 2

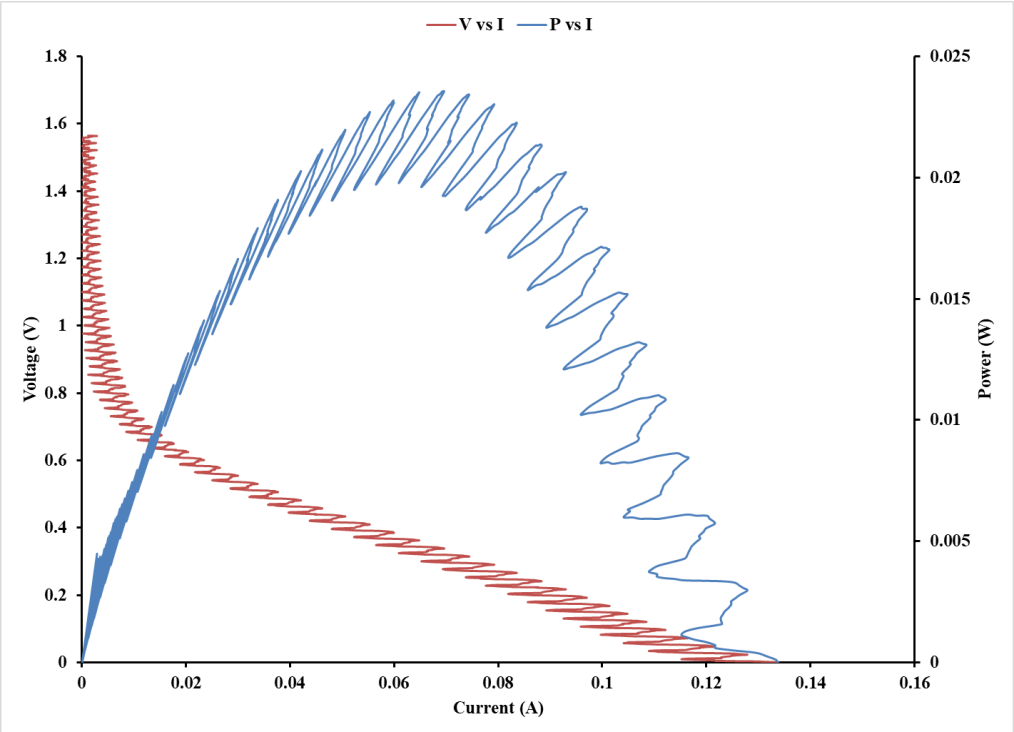

GraphA-20: LSV Graph of CS 2

Appendix B: Graphs Obtained For Batch 2 Samples

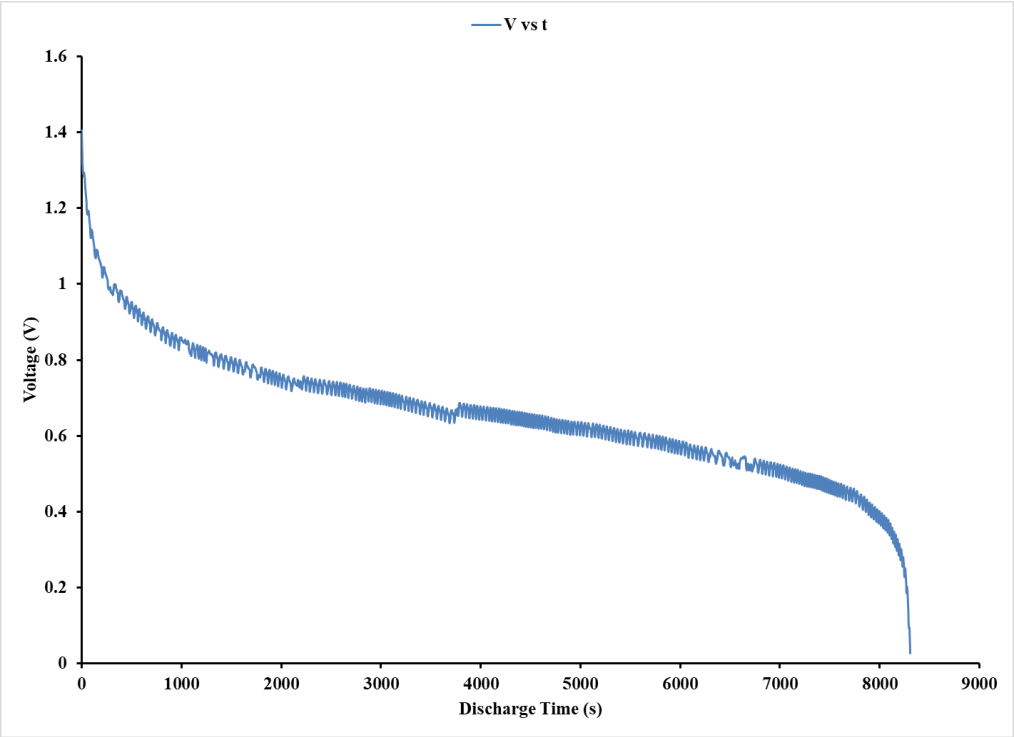

GraphB-1: Discharge Graph of Sample 10

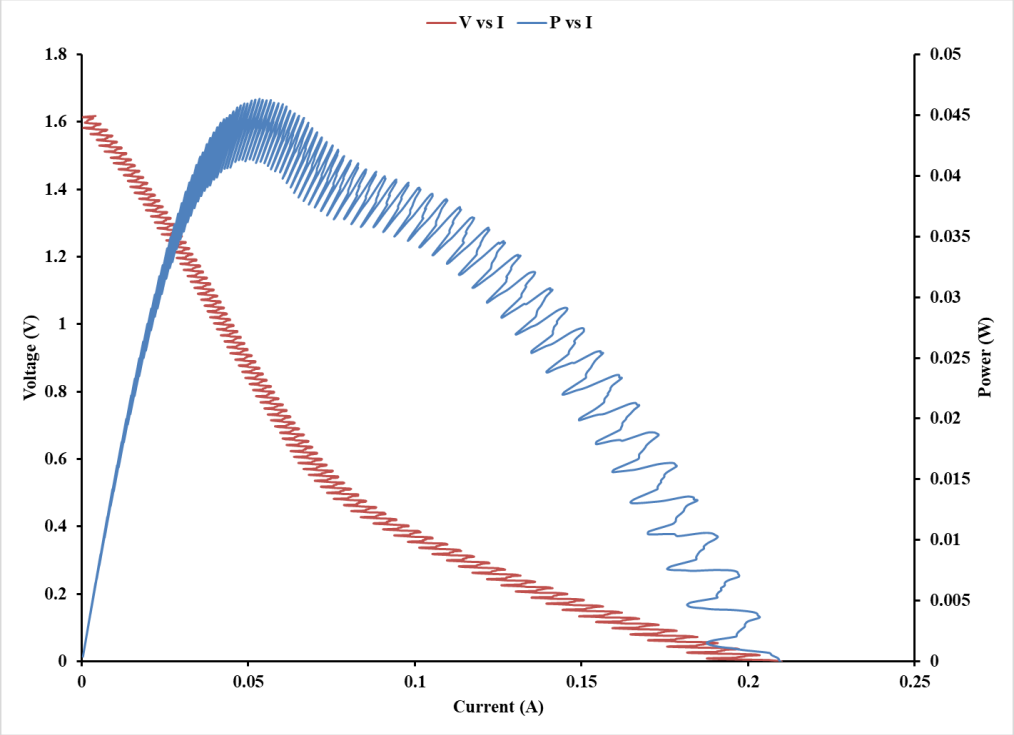

GraphB-2: LSV of Sample 10

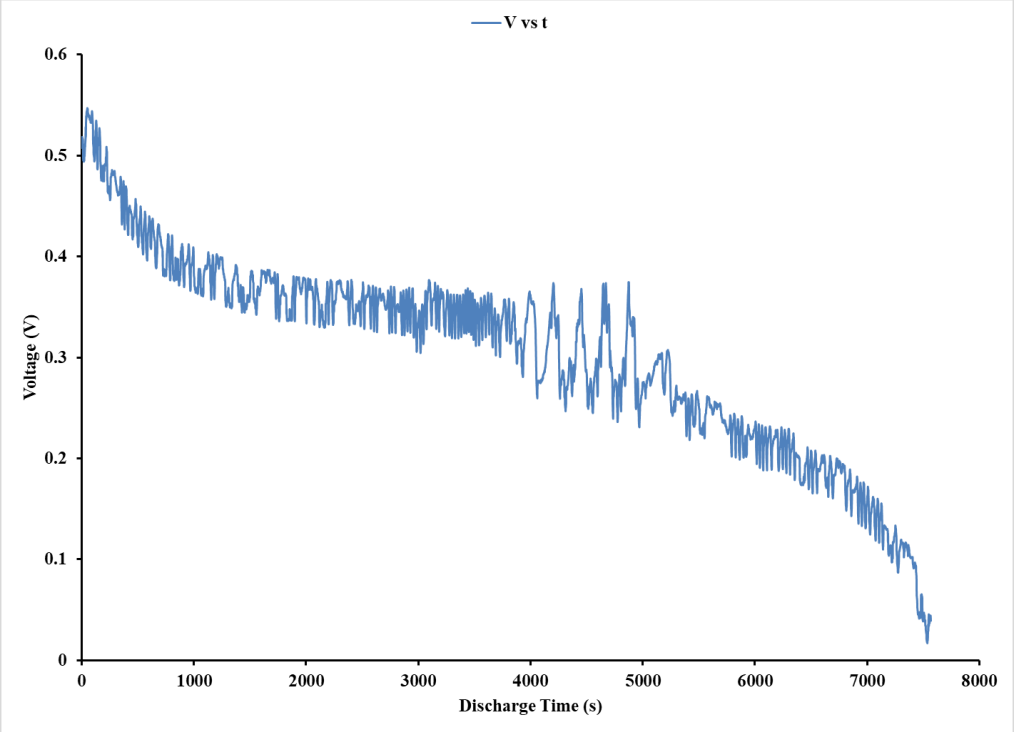

GraphB-3: Discharge Graph of Sample 11

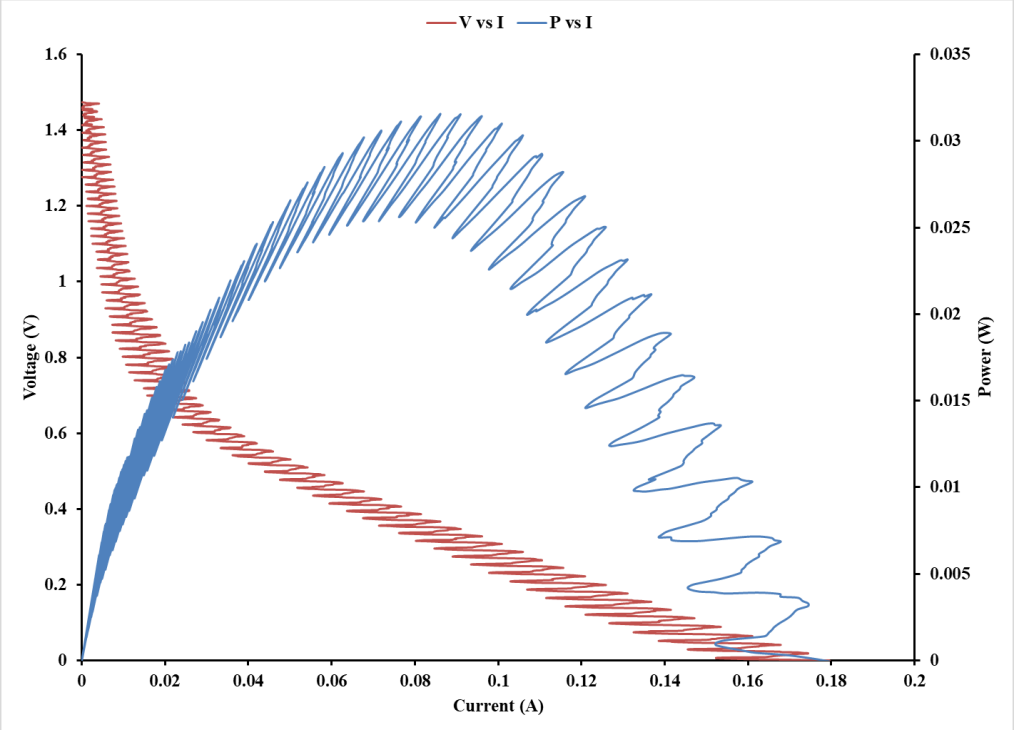

GraphB-4: LSV Graph of Sample 11

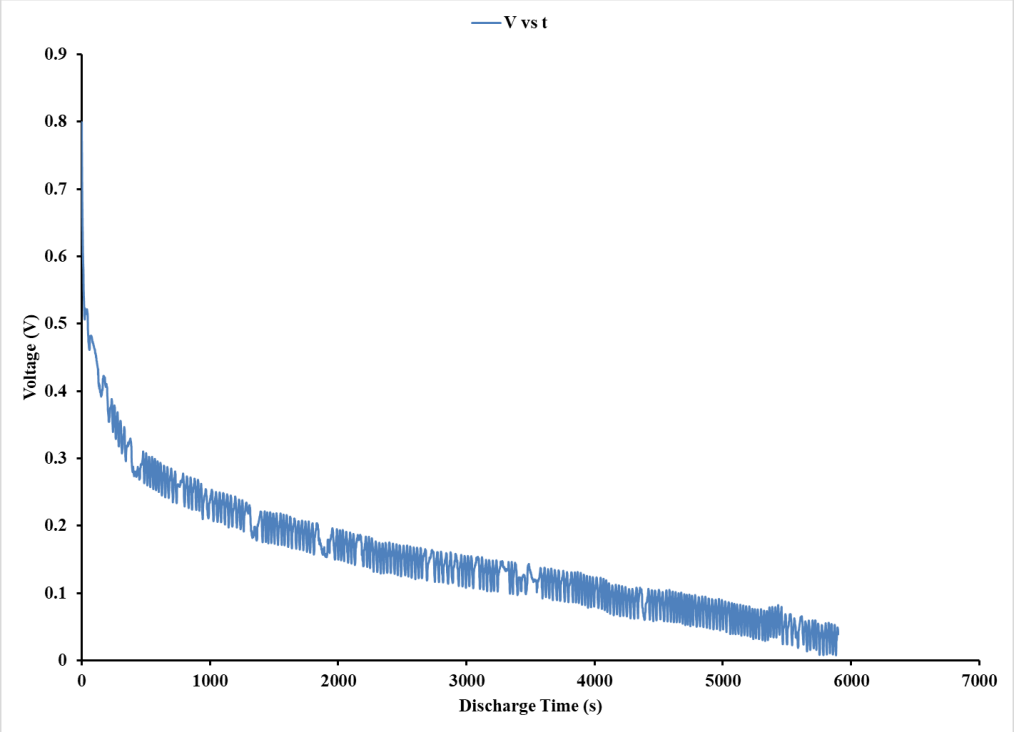

GraphB-5: Discharge Graph of Sample 12

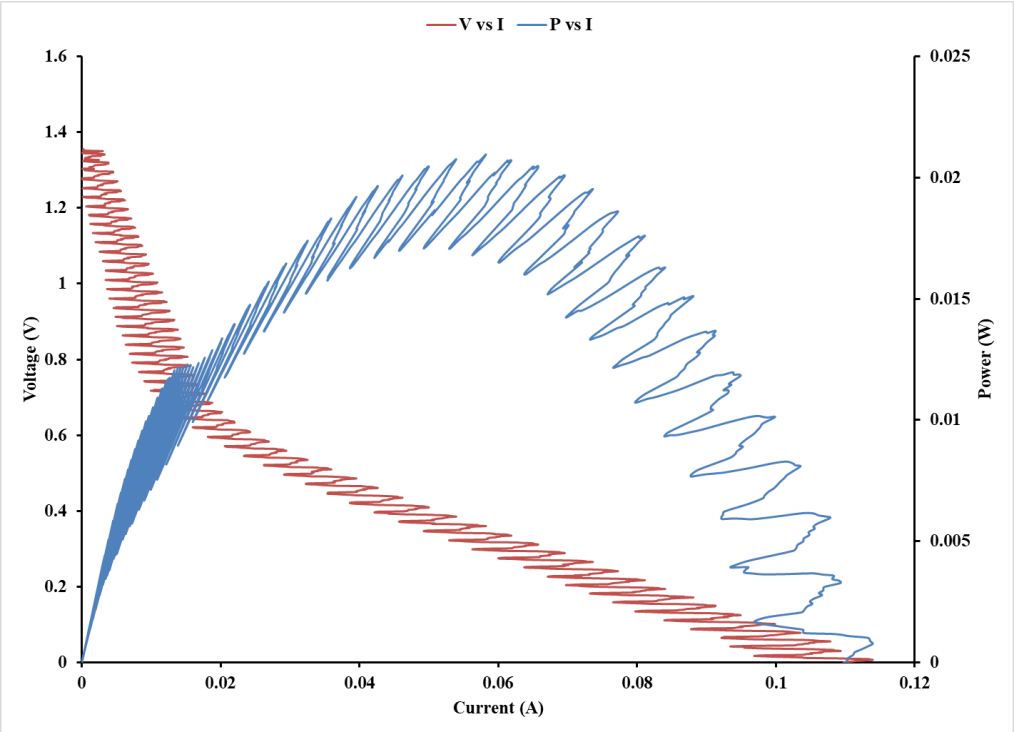

GraphB-6: LSV Graph of Sample 12

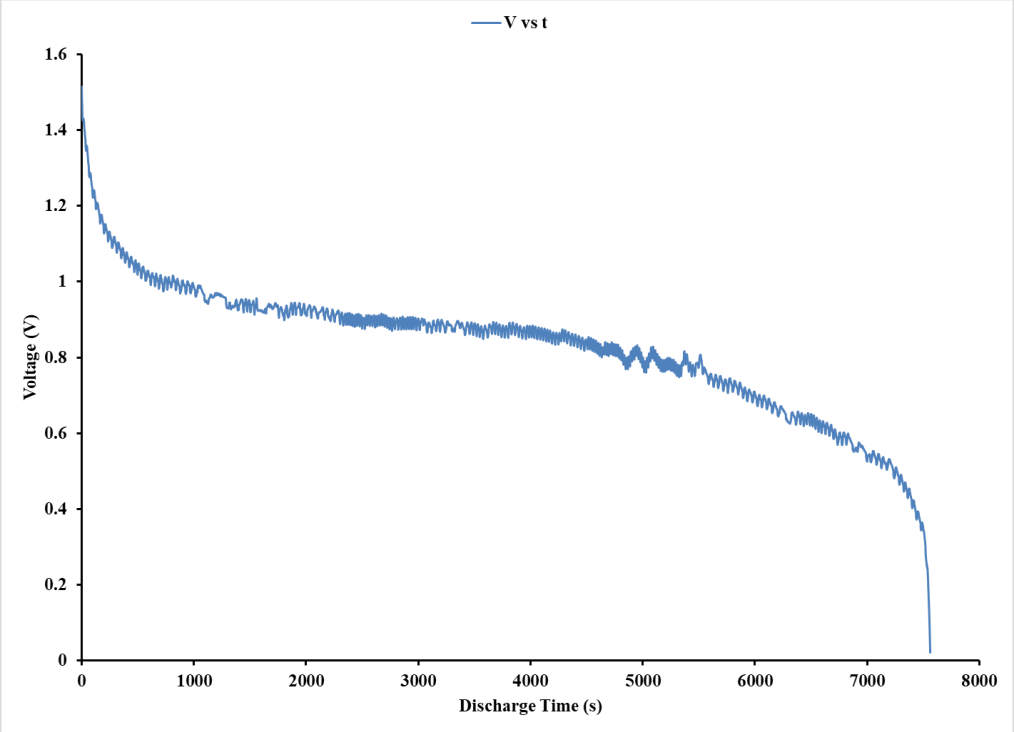

GraphB-7: Discharge Graph of Sample 13

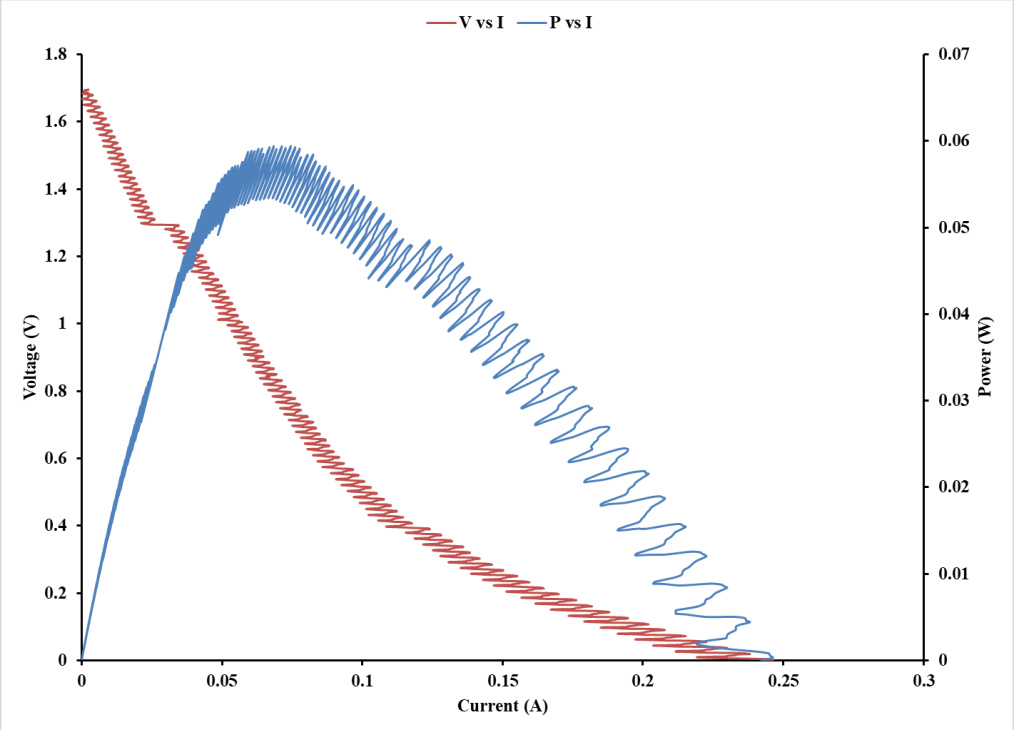

GraphB-8: LSV Graph of Sample 13

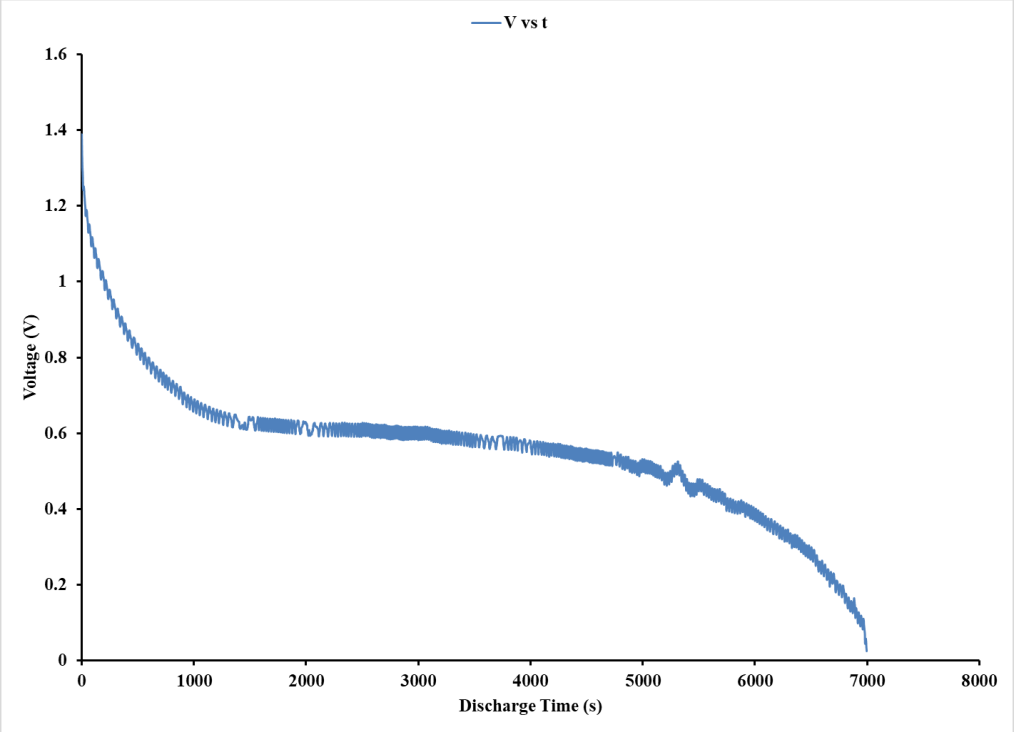

GraphB-9: Discharge Graph of Sample 14

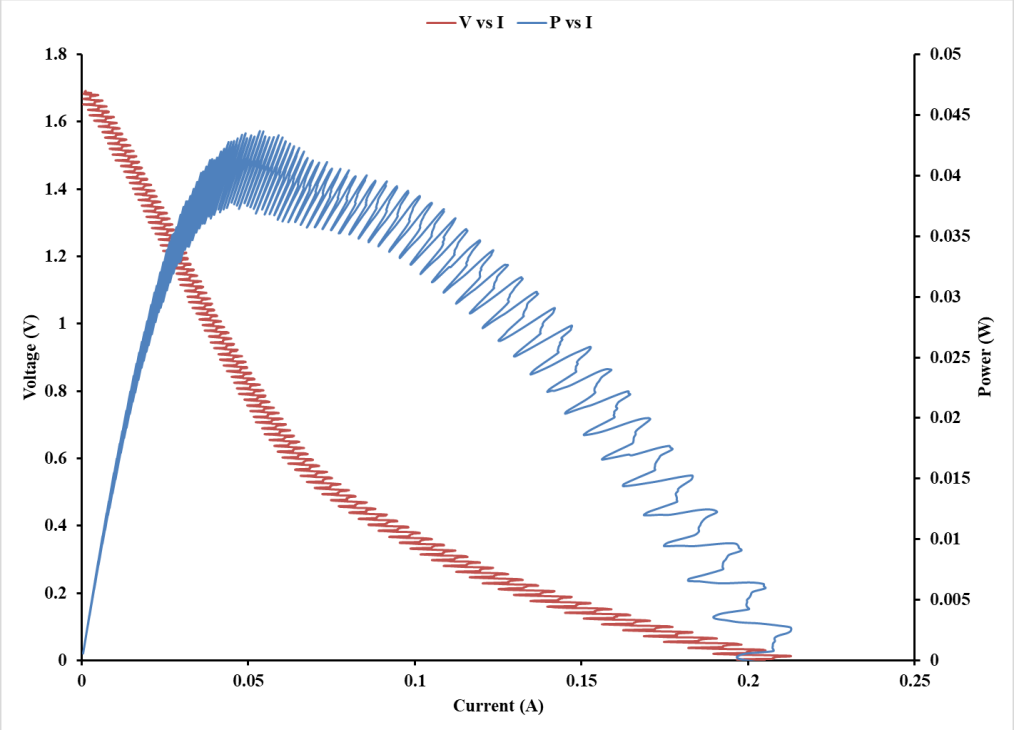

GraphB-10: LSV Graph of Sample 14

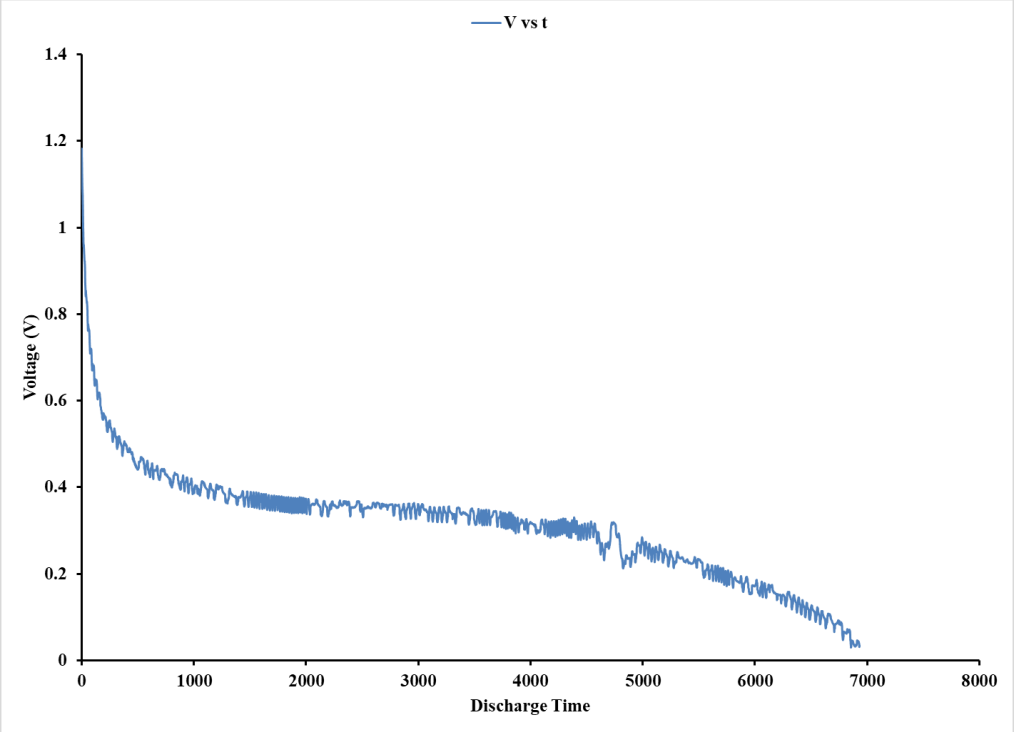

GraphB-11: Discharge Graph of Sample 15

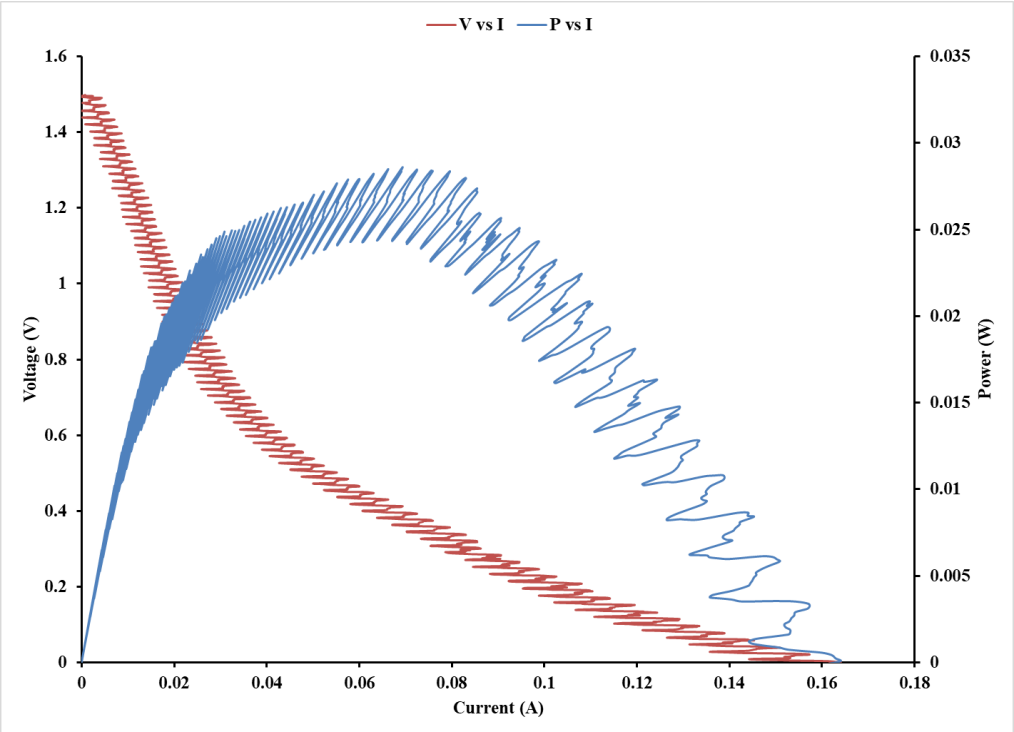

GraphB-12: LSV Graph of Sample 15

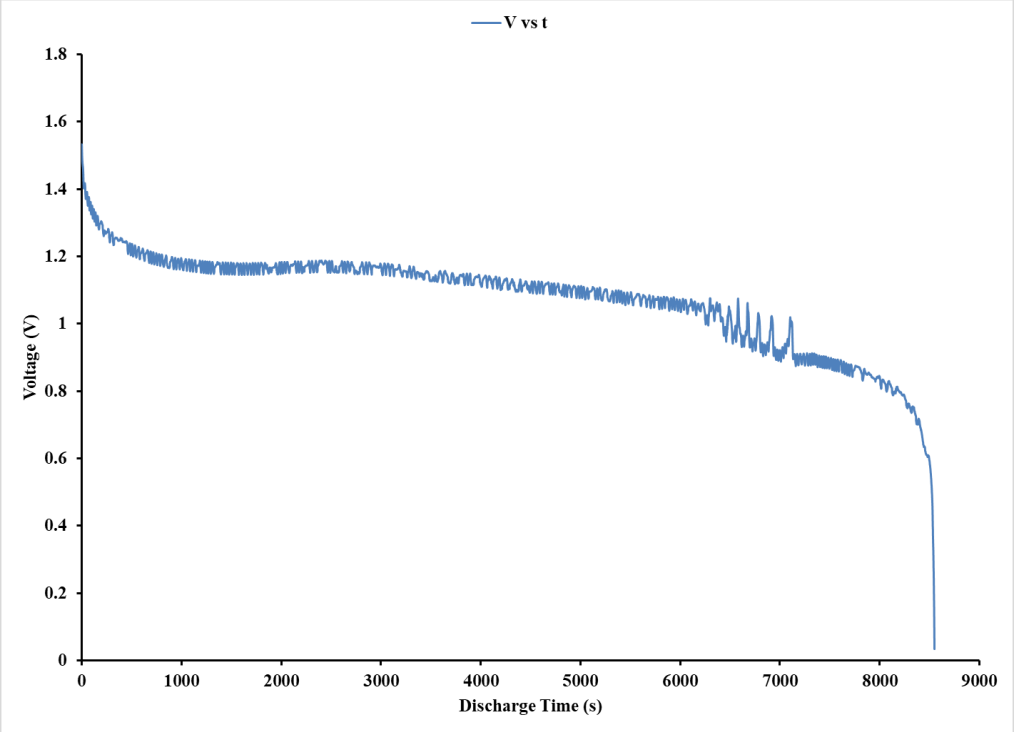

GraphB-13: Discharge Graph of Sample 16

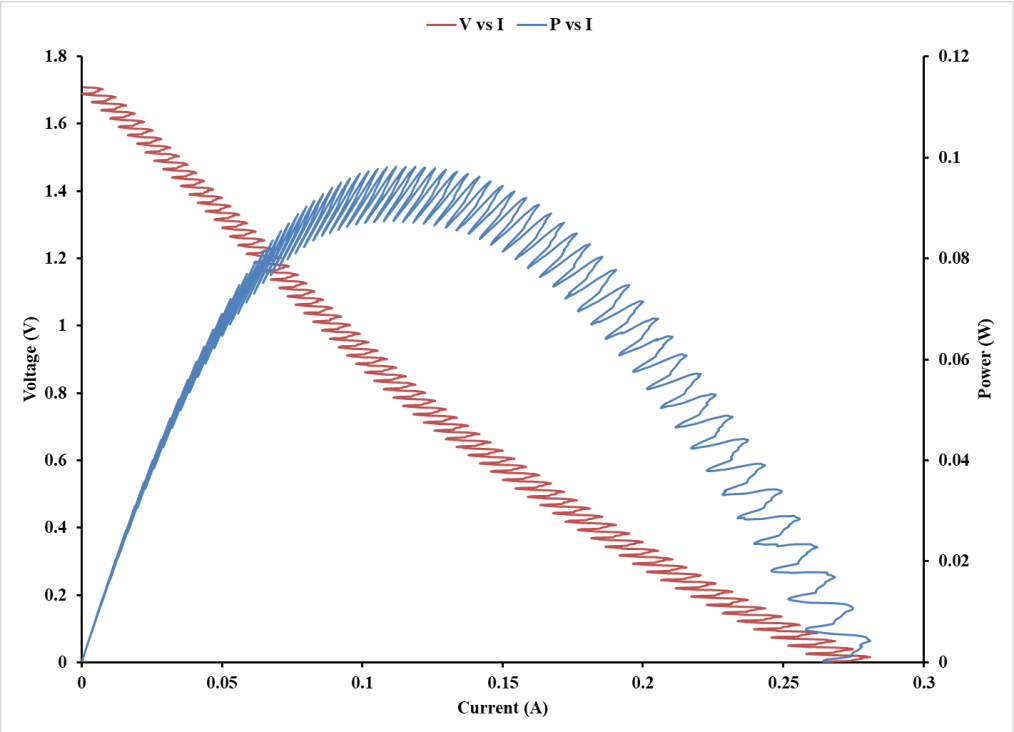

GraphB-14: LSV Graph of Sample 16

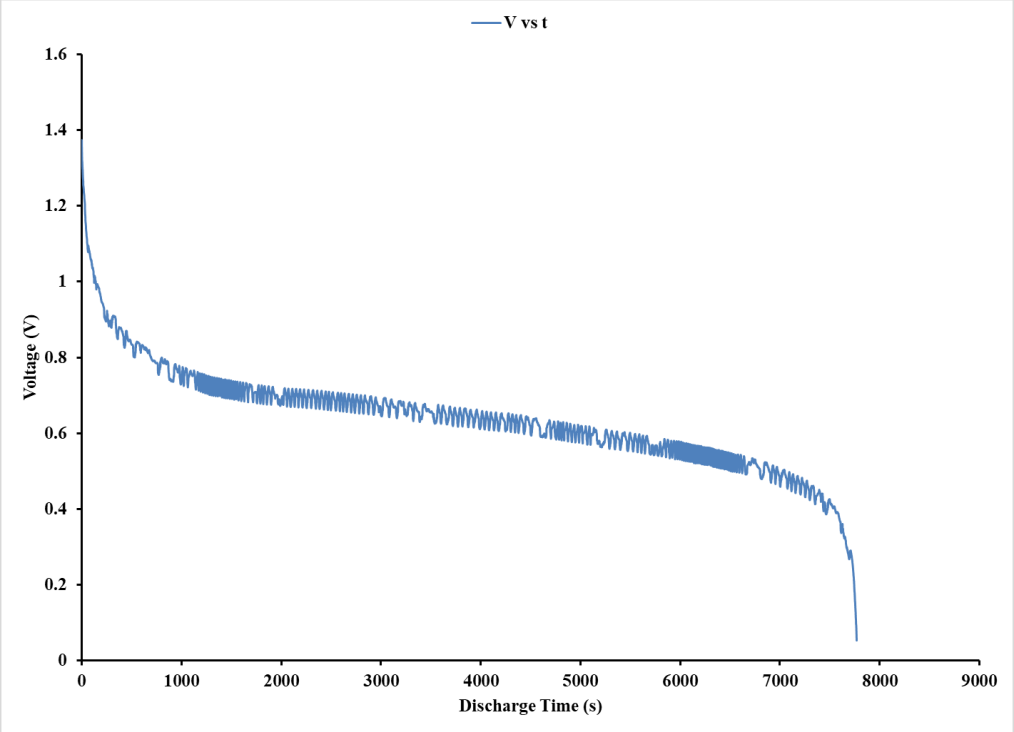

GraphB-15: Discharge Graph of Sample 17

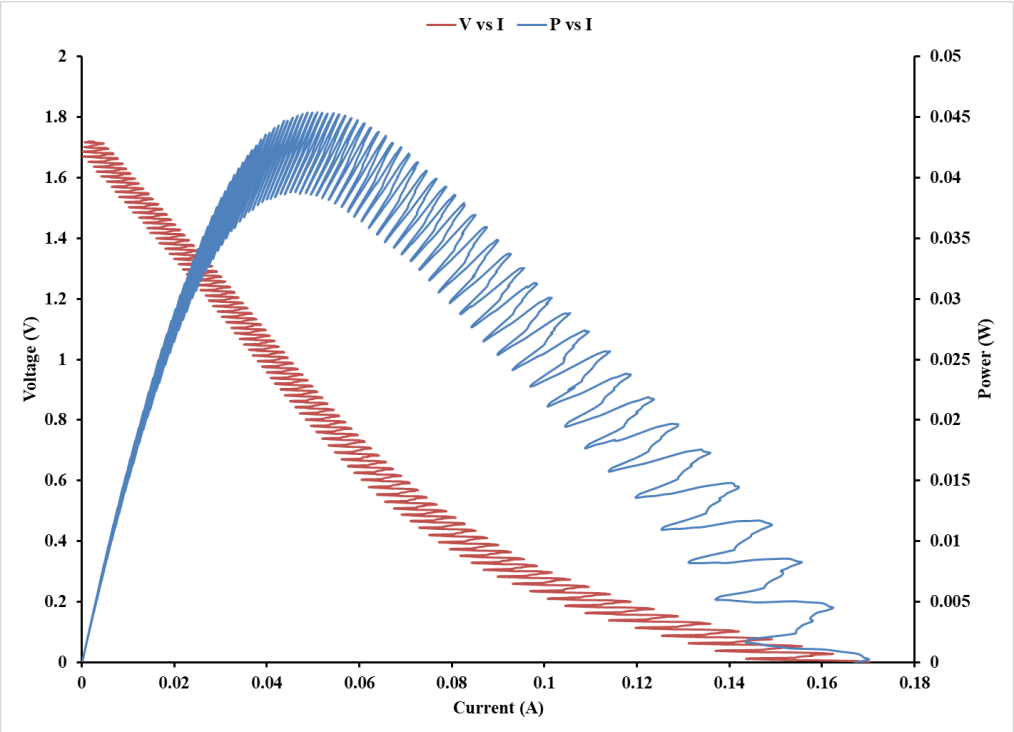

GraphB-16: LSV Graph of Sample 17

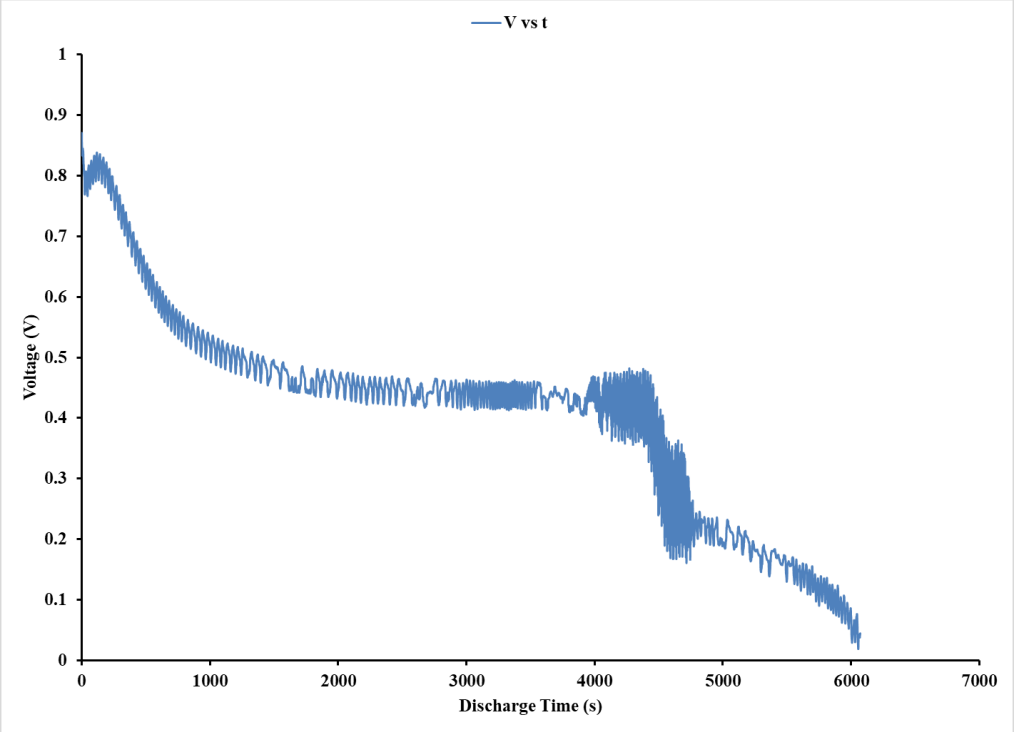

GraphB-17: Discharge Graph of Sample 18

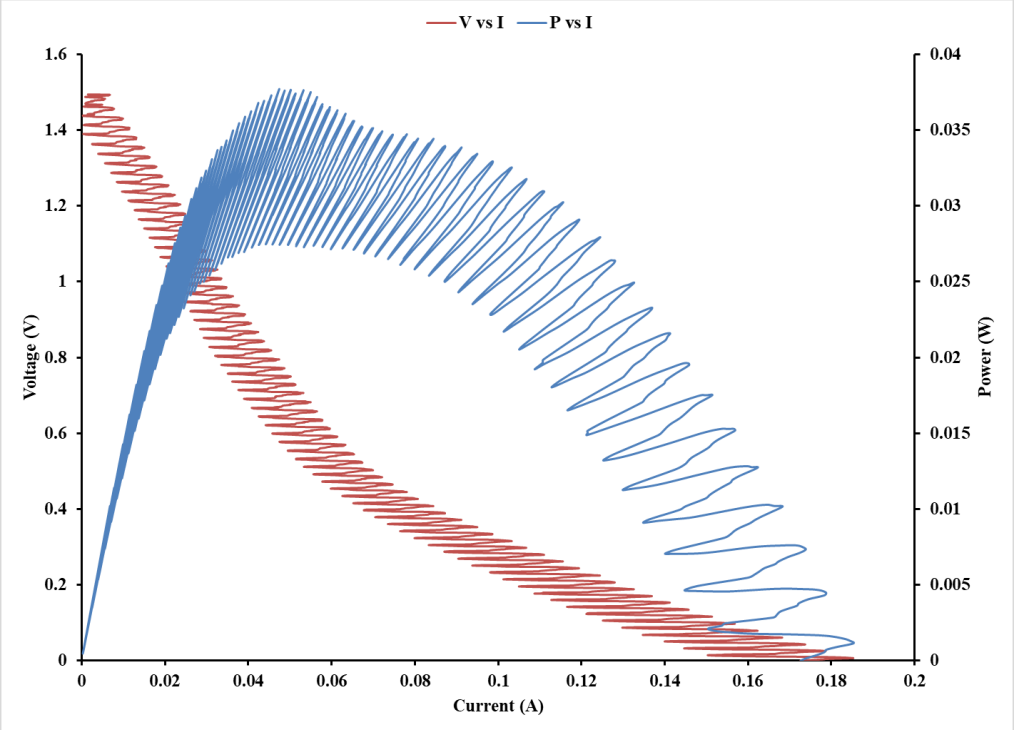

GraphB-18: LSV Graph of Sample 18